MULTIPLE MOVING TARGET DETECTION WITH ULTRA WIDEBAND RADAR USING SUPER-RESOLUTION ALGORITHMS

by
ERMAN ENGİN

Submitted to the Graduate School of Engineering and Natural Sciences
in partial fulfillment of
the requirements for the degree of
Master of Science in Electronics Engineering

Sabanci University
August 2007

MULTIPLE MOVING TARGET DETECTION WITH ULTRA WIDEBAND RADAR USING SUPER-RESOLUTION ALGORITHMS

APPROVED BY:

Associate Professor Meriç ÖZCAN (Thesis Supervisor)	_____
Associate Professor İbrahim TEKİN	_____
Assistant Professor Ayhan BOZKURT	_____
Assistant Professor Mehmet KESKİNÖZ	_____
Assistant Professor Serhat YEŞİLYURT	_____

DATE OF APPROVAL _____

MULTIPLE MOVING TARGET DETECTION WITH ULTRA WIDEBAND RADAR USING SUPER-RESOLUTION ALGORITHMS

Erman Engin

EECS, MSc Thesis, 2007

Thesis Supervisor: Assoc. Prof. Meriç Özcan

Keywords: Ultra Wideband Radar, Moving Target Detection, Super-Resolution, Multiple Signal Classification (MUSIC)

ABSTACT

The improvements in microwave electronics opened the way to build microwave components such as low noise amplifiers, samplers and pulse generators that are broadband. As these building blocks are being developed, new applications become subject of research. Ultra wideband radar is one of these subjects. Major applications of ultra wideband radars are behind the wall imaging, biomedical imaging and buried land mine detection.

In this study we aimed to locate multiple scatterers that are moving. Even though there are many scatterers in an environment, detection of moving targets is possible using differences of successive radar snapshots. This is generally the case when behind the wall human targets are to be detected. We investigated the effectiveness of various types Multiple Signal Classification (MUSIC) algorithms on the data acquired by our ultra wideband radar prototype.

In ideal computer simulations, Time Reversal MUSIC (TRM) algorithm provides successful estimations of both directions and distances of multiple targets. However in practice where non-ideal effects are existent, the performance of TRM algorithm is estimating the target distances degrades. On the other hand, Delay Estimation MUSIC algorithm provides better estimates for the distances of the targets since it is less sensitive to phase noise. Combining the output of TRM algorithm for target directions and the output of Delay Estimation MUSIC method for target distances resulted in successful localization of targets. Experiments are performed using two moving targets in order to test the effectiveness the proposed processing scheme. The problem of detection ambiguities is also considered and several methods to resolve actual targets are presented.

ULTRA GENİŞ BANTLI RADAR İLE ÜSTÜN ÇÖZÜNÜRLÜK ALGORİTMALARI KULLANARAK ÇOKLU HAREKETLİ HEDEFLERİN SEZİMİ

Erman Engin

EECS, MSc Tez, 2007

Tez Danışmanı: Doç. Dr. Meriç Özcan

Anahtar Kelimeler: Ultra Genişbantlı Radar, Hareketli Hedef Sezimi, Üstün Çözünürlük, Çoklu Sinyal Sınıflandırması

ÖZET

Mikrodalga elekroniği alanındaki gelişmeler, genişbantta çalışabilen düşük gürültülü yükselteç, örnekleyici, darbe üreteci gibi mikrodalga elemanlarının yapılabilmesinin yolunu açtı. Bir yandan bu temel yapıtaşları geliştirilirken diğer yandan yeni uygulama alanları araştırma konusu haline geldi. Ultra Genişbantlı Radar bu konulardan bir tanesidir. Duvar arkası görüntüleme, medikal görüntüleme ve gömülü yeraltı mayınlarının tespiti, Ultra Genişbantlı Radarların temel uygulama alanları arasındadır.

Bu çalışmada hareket halinde olan çoklu hedeflerin yerini saptamayı hedefledik. Bir ortamda bir çok saçıcı olsa da, hareketli olan hedeflerin tespiti, ard arda gelen radar enstantenelerinin farkını kullanarak mümkün hale geliyor. Genel olarak duvar arkasındaki insan hedeflerinin tespitindeki durum da budur. Çeşitli Çoklu Sinyal Sınıflandırması (Multiple Signal Classification - MUSIC) algoritmalarının verimliliğini, kendi Ultra Genişbantlı Radar ilkörneğimizle elde ettiğimiz veriler üzerinde tetkik ettik.

Ideal, gürlütüsüz ortamlar için gerçekleştirilen bilgisayar simulasyonlarında, Zaman Tersinimli MUSIC (Time Reversal MUSIC - TRM) algoritması, hedeflerin hem doğrultuları hem de mesafeleri konusunda başarılı sonuçlar sağlıyor. Ancak, ideal olmayan etkilerin de mevcut olduğu gerçek uygulamalarda, TRM algoritmasının hedeflerin mesafelerini bulmadaki verimliliği düşüyor. Öte yandan evre gürültüsüne daha az duyarlı olan MUSIC ile Gecikme Kestirimi (Delay Estimation MUSIC - DEM) algoritması hedeflerin mesafeleri konusunda daha iyi tahminler veriyor. TRM algoritmasının hedeflerin yönü için çıkışıyla DEM algoritmasının hedeflerin mesafeleri için çıkışını birleştirmek, hedeflerin yerinin başarılı bir şekilde bulunmasına olanak verdi. Öne sürülen sinyal işleme tertibinin tesirini sınamak için iki hareketli hedef kullanılarak deneneyler yapıldı. Sahte hedeflerin ortaya çıkması sorunu da ele alındı ve gerçek hedefleri çözümlemek için birkaç yöntem ileri sürüldü.

TÜM İNSANLIĞA…

To All Humanity

ACKNOWLEDGEMENTS

I would like to thank my father, my mother and my brother for their efforts since my childhood. Also to all of my aunts like angels especially S. Aksoy who influenced me throughout my life, to my uncles who always encouraged me and to all of my relatives.

Special thanks to Meriç Özcan, İbrahim Tekin and Mehmet Keskinöz for guiding me in my academic life, my roommate Mustafa Parlak who is one of the rare ones with his kindness and tolerance, Bülent Köroğlu for his helps and motivating talks and all others who took role in my well being.

TABLE OF CONTENTS

LIST OF FIGURES

LIST OF TABLES

CHAPTER 1

INTRODUCTION

1.1 Motivation

One can write a thousand-page book to express the importance of the imaging. However, since I do not have such a large space here, I will only try to make a summary. Knowing the reasons, causes and outcomes of events and analyzing the mysteries of structures that surround us gives humans confidence and control over that events. In a manner, imaging provides us this knowledge. In many cases observing an event with our eyes is the first step of analyzing it and tells us what to do as the next step. Imaging can be divided into a

Consider your eye as an imaging device. The light waves reflected or emitted from objects are focused onto the retina and at a moment we get the information of colors and shapes of the objects. Furthermore we can obtain other information using our pre-knowledge. By seeing a bottle that has condensed vapor on its surface we can guess that the water inside the bottle is cold. So by looking at an object we get a lot of information about our surroundings. It would be very hard to live without our eyes.

When what we want to observe is beyond the capability of our eyes we develop devices to observe events such as microscopes, x-ray devices, ultrasonic probes or radars. There are various areas of imaging such as optical imaging, acoustical imaging, radar imaging and magnetic resonance imaging which are named according to the source of information used in obtaining the image. In medicine, imaging is used in order to observe microorganisms, tissues and organs, detection of structural disorders, diagnosis of diseases and defects such as tumors. Typical military applications of imaging are observation of aerial targets, battlefield surveillance, navigation of missiles and landmine detection. In geophysics analyzing the structure of Earth's crust, schists

or detection of mines; in air or sea transportation, traffic control, collision avoidance, are the issues that imaging addresses. In this study we focus on imaging of moving targets behind obstacles using an Ultra Wideband (UWB) Radar.

Advances in technology trigger the development of new applications and also providing alternative solutions to existing problems. Ultra Wideband (UWB) Radar became an important research field as a consequence of the progress in microwave electronics that enabled the development of broadband electronic components such as pulse generators, samplers, amplifiers. We will discuss the advantages and applications of UWB radars in more detail in the proceeding sections. Briefly speaking, increased resolution, immunity to interference and low power operation are the major benefits of UWB radars. They can be used in various fields such as biomedical imaging, through-wall imaging, landmine detection, automotive sensors. There is a valuable research on UWB communications and relatively less on UWB radars however UWB technology is not yet mature in both areas.

Besides the importance of the concept, what motivates me is the research itself. Developing a system level device, making experiments that no one has done before gives the feeling that you are a member of the developers of technology.

1.2 Organization of the Thesis

In this chapter, I tried to explain the significance of this research. Chapter 2 will cover the concept of radars presenting the basic working principle, the classification of radar systems, the evolution of radars throughout the history and mathematical formulations about radar signal transmission, scattering and reception. Then we will focus on Ultra Wideband Radars, giving a brief history and advantages when compared to conventional radar systems. At the end of Chapter 2, I will try to present the current position of research about UWB radars.

In Chapter 3 the numerical computation technique, Finite Difference Time Domain (FDTD) algorithm will be presented in detail including Berenger's Perfectly Matched Layer implementation. Later in Chapter 4 signal processing algorithms will be presented. These algorithms include the classical MUSIC, Time Reversal MUSIC and Delay Estimation MUSIC. With the background provided in Chapter 4, in Chapter 5, I will present the experiments performed, how the processing algorithms are applied to

the experimental data, the problems encountered such as detection ambiguities and the methods to solve these. Finally in Chapter 6 there is the conclusion and the future improvements of our system will be discussed.

I aimed the completeness of the thesis and I tried to express the key points that should be clear in order to understand the subject, especially while presenting the signal processing algorithms. Readers are expected to have a familiarity with linear algebra since the proofs of linear algebraic theorems are not given. One should refer to books on linear algebra for the proofs of these theorems.

CHAPTER 2

RADARS

2.1 Radars in General

The word **RADAR** is an acronym for **Radio Detection and Ranging**. Radar can be defined as a device used for gathering information on remote objects utilizing the electromagnetic waves reflected from or emitted by the objects. The type of information can be range, direction, speed, shape, altitude, etc. The targets may be illuminated either by the radar device itself or by third-party transmitters in the environment.

The first radar is considered as the "Telemobiloscope" invented by Christian Hülsmeyer in 1904, which is used to detect the presence of ships in 3 km range using a spark gap transmitter. It was Nikola Tesla who proposed the basic principles of Radars. In 1920's there was a research going on in U.S Naval research laboratories where the first continuous wave radar is invented. Robert Watson-Watt is also one of the great contributors to the development of radars by being able to detect aircrafts using radio waves. During World War II as in many areas of science there has been a great effort in developing radars. Radars played a crucial role in the defeat of Germans in the "Battle of Britain". Developments in radar increased significantly by the invention of klystron, a device that generates microwaves. Other improvements in electronics, electromagnetics, signal processing methods further triggered the developments.

Most known application of radars is the detection of approaching aircrafts or ships which it was originally developed for. Throughout the evolution of radars not only the detection of existence of a target but detecting the range, speed, type or shape also became possible. Some military applications of radars include Early Warning (EW) radars [1], [2] for detecting approaching targets that are terrestrial, airborne or

seaborne, navigation of missiles, tracking of targets and battlefield surveillance. In air transportation Air Traffic Control (ATC) systems involve radars used to monitor airplanes [3], [4] and prevent collisions [5] or to assist airplanes while landing. Similarly, in sea transportation avoidance of ship collisions [6], navigation of ships is maintained by radars. Weather radars are used in weather forecasting, tracking of atmospheric events such as motions of clouds, precipitation, hurricanes, directions and speeds of winds [7], [8]. In geophysics, Ground Penetrating Radars (GPR) are used to obtain subsurface profiling such as locating mines, ground water, bedrock, voids or infrastructure [9]-[11]. Radars are also used for planetary observations [12].

It is possible to classify radars according to frequency range of operation, purpose of usage, type of the transmitted wave and so on. Here we will classify radar systems according to their receiver and transmitter structure. In this approach radars can be classified as monostatic, bistatic or multistatic. In monostatic radars same antenna is used for both illuminating the targets and receiving the back scattered echoes. A special case of monostatic radars called pseudo-monostatic radars are where the transmitter and receiver antennas are not collocated; however they are separated by a distance much smaller than the range of the targets to be detected. Therefore the angle between the transmitter, target and receiver is close to zero. Bistatic radars have a transmitter and a receiver separated with a comparable distance to the range of the targets to be detected. Passive radars are a specific case of bistatic radars which have no transmitter but utilize the available electromagnetic signals in the environment such as radio or television broadcast as illuminators. They work by comparing the signal coming directly from the illuminator and the one reflected from the target. Finally multistatic radars have more than three elements comprising both transmitters and receivers. Our experimental radar prototype which will be explained in detail in Chapter 5 can be considered as a multistatic radar.

At this point it would be helpful to present basic radar equations formulating the received power level and radar cross-section of targets. Readers willing to have a more detailed analysis of radars can consult [13].

2.1.1 The Bistatic Radar Equation

An omni directional antenna has a spherical radiation pattern, which means it radiates equal amount of power to every direction in three dimensional space. So the power per unit area on a spherical enclosure having radius R with the antenna being at the center is given by:

$$P_D = \frac{P_t}{4\pi R^2}, \tag{2.1}$$

where P_t is the total transmitted power.

If directional antennas are used instead of omni directional ones the radiated power concentrates in a region defined as the "beam angle". The gain of the antenna G is defined as the ratio of the antenna's radiation intensity at the direction that it is maximum, to the intensity of a reference antenna. If the reference antenna is an isotropic antenna the gain can be expressed in *dBi* units. Antenna effective aperture is related with gain by the formula:

$$A_e = \frac{G\lambda^2}{4\pi} \tag{2.2}$$

Equation (2.1) can be rewritten incorporating the gain of the antenna as:

$$P_D = \frac{P_t G}{4\pi R^2} \tag{2.3}$$

The ratio of the back scattered power to the density of incident power on the target is defined as Radar Cross Section (RCS) given by:

$$\sigma = \frac{P_b}{P_D}, \tag{2.4}$$

where P_b represents the total back scattered power and P_D is the incident power density on the target. RCS can also be considered as the effective surface of the target that radiates the incident power isotropically. Therefore the unit of RCS is meters^2. In the bistatic case where the transmitter and the receiver antennas are separated, the RCS of the target is dependent on both the direction of incidence of the radiated power (or direction of transmitter) and the direction of the receiver. Then the total received power is formulated by:

$$P_r = \underbrace{(P_t G_t)}_{1}.\underbrace{\left(\frac{1}{4\pi R_T^2}\right)}_{2}.\underbrace{(\sigma(\theta_t,\theta_r))}_{3}.\underbrace{\left(\frac{1}{4\pi R_R^2}\right)}_{4}.\underbrace{A_R}_{5}. \quad (2.5)$$

where θ_t and θ_r are the angular position of the transmitter and the receiver antennas with respect to the target. Here the first multiplicand is the total radiated power and the second one is for obtaining the density of the power incident on the target which has a distance of R_T from the transmitter. Multiplication of the first three terms gives the total backscattered power (considered isotropically radiated by the target) from the target. The fourth term is the coefficient to calculate the power density of the spherical wave at the receiver antenna. And lastly A_R is the effective aperture of the receiver antenna.

Equation (2.5) is referred to as bistatic radar equation. In UWB radar systems the dependence of the gain of the antennas, the RCS of the target on frequency should also be taken into account. Also antenna losses, path losses, UWB pulse distortion are things to consider. Detailed analysis of UWB transmission, scattering and reception can be found in [14].

2.1.2 The Unambiguous Range

Practically in pulsed radar systems the radar snapshot of the environment can not be gathered using a single pulse. The pulses are sent periodically therefore the echoes coming from the targets are also periodic and this enables Equivalent Time Sampling (ETS) or elimination of noise. The periodicity of the pulses has implications on the maximum distance of the targets to prevent ambiguity. The echoes coming from the targets should reach to the receiver before the end of the period. Otherwise the echoes will be received in the next period and will be treated as if they are coming from a closer target. The maximum distance a target can be at in order that the backscattered pulse reaches to the receiver before another pulse is emitted from the transmitter is called “the unambiguous range”. In monostatic radars where the transmitter and the receiver are collocated the unambiguous range is an area limited by a circle with center being the transceiver. In case of a bistatic radar the region is limited by an ellipse with foci being the transmitter and the receiver antenna.

2.2 Ultra Wideband Radars

Ultra wideband (UWB) radar is often referred to as impulse radar, transmits UWB pulses to illuminate targets. According to Federal Communications Commission (FCC) the term ultra wideband refers to radio technologies having a minimum bandwidth of 500 MHz or a fractional bandwidth of at least %25 [15].

$$\frac{2(f_H - f_L)}{(f_H + f_L)} > 0.25 \tag{2.6}$$

Where f_H and f_L are higher and lower limits of the frequency band. The term "Ultra Wideband" was first used by Defense Advanced Research Projects Agency (DARPA) in 1990 for a radar system. Before then UWB was referred by terms such as base-band pulse, non-sinusoidal, time domain or carrierless [14].

It is said that the origin of UWB radio lies back to late 1800s to the spark-gap transmitters studied by Hertz, Tesla and Marconi. UWB radio was regulated by FCC part 15 rules which authorize the unlicensed use of UWB in 3.1 GHz to 10.6 GHz and under certain power levels to prevent severe interference to radio systems sharing the same band.

Ultra wideband radars are discriminated by conventional narrowband radars by their unique advantages. Several most significant advantages of UWB radars are listed in [16]:

1) Increased range resolution: As a result of pulses being short in time, echoes coming from targets having small differences in their distance to the radar, do not overlap. Besides, since errors in detecting the delay of an echo are related with the width of the pulse, as pulses become shorter in time their delay can be measured with a smaller error.
2) Ability of detecting slow moving targets: Higher range resolution means that slow variations in targets' positions can be monitored.
3) Ability to discriminate echoes coming from different elements of the target: As an implication of the first point, the reflections from different parts of the target can also be resolved. This provides information about the shape of the target. An application related to this can be determining the type of a buried landmine by constructing its geometric profile.

4) Increased probability of detection: Because the reflections coming from different parts of a target are less likely to interfere since the pulses are narrow, the probability of detecting the target correctly is increased.
5) Immunity to passive interference: By subtracting the successive snapshots the passive interference or equivalently stationary targets can be cancelled while moving targets will become apparent.
6) Ability to classify target material: Deriving the impulse response of the targets using the sent impulse like signals is possible. Responses from different targets may differ significantly so that they can be identified.
7) Noise-like behavior to collocated narrowband systems: Since the power is spread in spectrum, the power level at each frequency component is low. Therefore interference with narrowband systems becomes negligible.
8) Immunity to other radar systems working in the same band: The probability of UWB pulses emitted from different transmitters to overlap is small. Therefore by time hopping procedure interference of other UWB systems can be canceled.
9) Increased operational security: Since the power is spread to a wide range of frequencies, the power level at each frequency level is low. Therefore detection of UWB pulses by other systems is harder.

While UWB radar systems have the listed advantages, one encounters many difficulties in developing such a system, just like any other new technology. Design and manufacturing of system components such as pulse generators, low-noise or power amplifiers, antennas, matched filters, etc is challenging when ultra wide bandwidth is required. Another disadvantage is that the UWB signals are subject to noise in the whole band.

A different approach is synthetically forming the ultra wide frequency band by combining the responses of the targets in relatively narrow bands. With this approach the wide bandwidth requirement of the UWB radar can be solved by several narrowband transmitter and receiver systems. The cost is increased hardware and advantages such as noise-like behavior, reduced immunity to other radio waves and security discussed in items 7-9 are sacrificed. Also synthesizing the responses may take more computation time. However this type of radar still covers many applications as we will see examples in the following section.

2.3 Current Progress

UWB radar is not yet a mature technology. There is a significant amount of research carried on in UWB radar and especially in communications. There exists some commercially available UWB radar devices such as wall penetrating radar, RadarVision of Time-Domain Corporation and Prism200 of Cambridge Consultants. However, to our knowledge they do not operate well in cluttered environment such as imaging through the walls of an ordinary office where there is office furniture such as seats, cardboards besides human targets. There are also commercially available patient monitoring devices for detecting the heart rate, breath rate of the patient remotely of the company Wireless 2000.

I will try to summarize some recent studies on UWB radar systems. Of course, while these studies may lay on the valuable work done previously, I do not mention them here. I tried to select outstanding works in different types of applications of UWB radar.

Micropower Impulse Radar (MIR) is invented by McEwan [17] comes as the first important development to mention about. It was developed in 1993 as an outcome of the research for transient digitizer which was part of another project. McEwan was the one to apply this to radar receivers. In one transmission of a pulse only a small duration, window of the return signal called the range gate is sampled. Since the time of arrival of a reflected pulse corresponds to range in space, each range gate corresponds to different ranges. The whole range is covered in multiple periods. The radar operates with very low amount of power and is orders of magnitude less expensive than conventional systems and very compact. The pulse repetition frequency is random around a certain value, so that interference to other systems and detectability is reduced. Proposed applications are landmine detection, border surveillance, imaging of iron bars inside concrete, patient monitoring, automotive sensors etc. Some of the patents issued to T. McEwan are Phase coded, micro-power impulse radar motion sensor [18], Ultra-wideband receiver [19] and Ultra-wideband radar motion sensor [20], Body monitoring and imaging apparatus and method [21].

Another application of UWB radars is determining the thickness of snow above the surface of the sea ice. The snow thickness in Polar Regions effects the heat exchange between the oceans and the atmosphere which in turn affects the heat budget at the poles and the overall climate. Gogineni and others from the Kansas University

built radar prototype operating between 2GHz to 8GHz [22]. The radar does not operate by sending pulses but sweeping the frequency band by sending continuous wave signals. Therefore the system it self can not be considered as UWB, however is emulates UWB by synthesizing individual frequency components. This approach has advantages such as improving signal to noise ratio and has a relatively simpler hardware compared to typical UWB systems. In addition to the publication in 2003, the group published another article recently in September 2007, where a more sophisticated experiment performed in Antarctic Sea is presented [23]. The thickness of snow layer is measured with an accuracy of 3cm-6cm. The aim is to place the radar on a hedgehop helicopter or airplane so that measurements can be made more practically.

A biomedical study on UWB radars is the detection of malignant tumors in the breast. Researchers from University of Wisconsin, Madison presented their work in [24]. Both Finite Difference Time Domain computer simulations and the data obtained by experiments performed on breast phantoms have been done to locate tumors. Generalized Likelihood Ratio Test (GLRT) is applied to find the likelihood of presence of a tumor in a given location. The experiments are performed using arrays of antennas placed around the phantom. A performance network analyzer is used to synthetically generate microwave pulses in 1GHz to 11 GHz band. A tumor having dielectric contrast ratio of 1.43:1 is proven to be detectable using numerical simulations. Also using experimental data, low dielectric contrast tumors such as 1.5:1 can be localized within a few millimeters of the actual location of the tumor.

Signal processing is as important as the hardware design in radar applications. Especially in a UWB system the difficulties in hardware make the signal processing side even more important. Ultrasound imaging and microwave radar topics are very close by means of theory and signal processing. An example of an implementation of an algorithm developed for acoustical imaging to electromagnetics can be found in [25]. In this article, DORT, French acronym for Decomposition of the Time Reversal Operator, is applied to electromagnetics additionally by using UWB pulses. DORT method [26] can be considered as an extension to the Multiple Signal Classification (MUSIC) algorithm and it enables locating targets or focusing the transmitted acoustical signals on the individual scatterers in the environment. A potential application is focusing the pressure wave on the kidney stone to break it apart. This method addresses the difficulties encountered in cluttered environment therefore; it is suitable to be used in subsurface imaging of soil. Using UWB pulses provide information about a wide

range of frequencies which is used to extract the resonant frequencies of the scatterers and to determine the number of scatterers. In the time domain data, it is also straightforward to eliminate the reflections coming from unwanted boundaries such as the air-soil boundary in subsurface imaging. Numerical simulation results are also presented where the locations of two metallic pipes are found. Experimental studies about DORT method in the field of acoustics can be found in [27], [28].

The studies discussed above are few examples chosen from recent studies on Ultra Wideband radars. The algorithm that we used in this study has resemblance to the last one.

CHAPTER 3

FINITE DIFFERENCE TIME DOMAIN METHOD

3.1 Introduction

There is no doubt that the greatest improvement in electromagnetics has been done by Maxwell who mathematically formulated the electromagnetic waves incorporating the results of earlier studies. The importance of electromagnetics became significant during the World War II in which radars took an important role in determining the course of the war. From those days we reached today's world where electromagnetics penetrated so deeply in our daily lives.

Predicting the responses of objects to electric and magnetic disturbances is the key to model, design and implement devices based on electromagnetics. Finite Difference Time Domain (FDTD) is one of the many numerical methods for solving Maxwell's equations. Using numerical methods we can analyze the scattering of electromagnetic waves from complex objects or the interaction of electromagnetic waves with materials, which we can not find a solution analytically. Therefore numerical methods significantly simplify the design of complex electromagnetic devices such as waveguides, couplers or antennas besides it provides solutions for the response of objects to electromagnetic waves. An example of FDTD in radar applications is finding and/or predicting the response of targets to transmitted waves.

Before the invention of computers, people used to solve Maxwell's equations analytically. By the availability of programmable computers researchers started using numerical solving methods such as high-frequency asymptotic methods and integral equations. The drawbacks of these methods led the researchers to discover time-domain solutions for Maxwell's equations. In 1966 Yee introduced the first time-domain approach [29] later named as Finite Difference Time Domain technique. FDTD's

ability of handling impulse like signals and simulating the nonlinear behavior naturally are the major advantages [30]. Since it works in the time domain it can provide information about a wide range of frequencies in a single run. Instead of complex reformulation of integral equations, FDTD method only requires the generation of meshes. FDTD is also used in simulations of acoustic waves [31], [32].

FDTD method can be used in solving one, two or three dimensional problems. Throughout this thesis we will focus on two dimensional FDTD solutions. [30] is a comprehensive source about FDTD method.

3.2 Overview

In FDTD method Maxwell's differential equations are discretized into so called difference equations. This discretization occurs both in time and in space. The discretization in space means meshing the computational medium e.g. the waveguide or the antenna in which the electric and magnetic fields radiated from sources are to be solved with respect to time. The meshes do not have to be uniform however in this thesis we will only consider uniform Cartesian mesh which is the simplest one. As an example, Fig. 3.1 shows a ridge waveguide meshed into cubic cells.

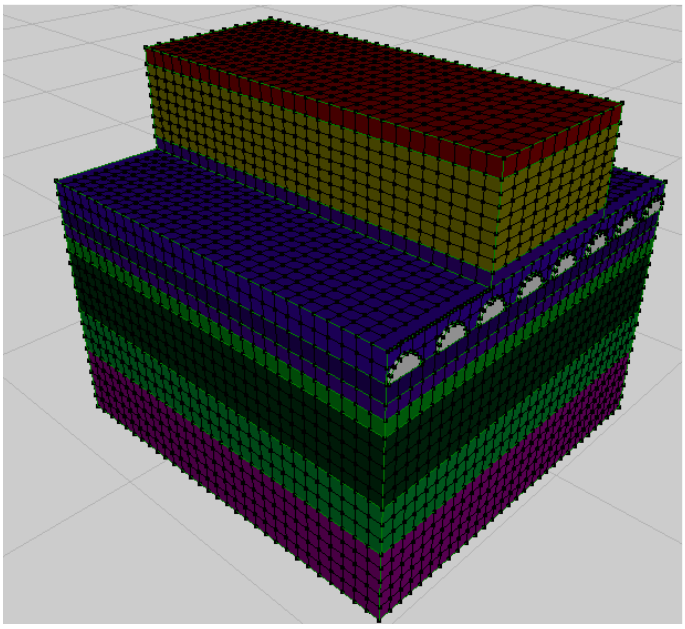

Fig. 3.1 A ridge waveguide meshed into cubic cells

In cases where the problem can be reduced to two dimensions, (i.e. fields can be assumed uniform in the third dimension) the computational domain becomes a surface. For example the propagation of light in a photonic crystal waveguide sufficiently long in height, can be reduced to a two dimensional problem. Fig. 3.2 shows the propagation of a wave inside an L-shaped photonic crystal waveguide solved by FDTD method. The black spots represent the rods with a relative permittivity of 12 and the background medium is free space. The filling ratio is 0.4 and the normalized frequency of the wave is 0.34.

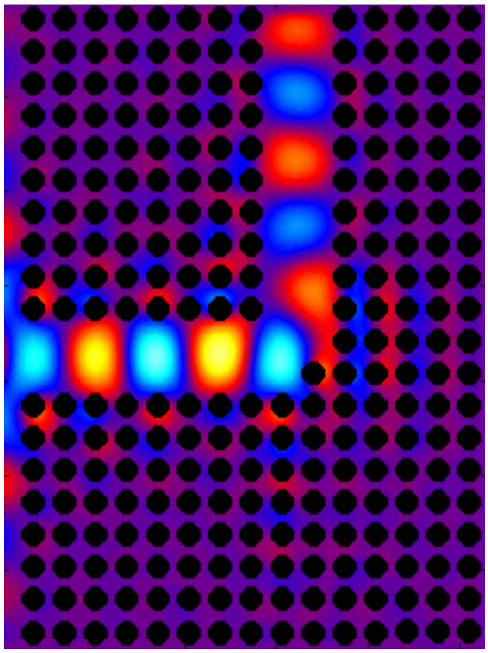

Fig. 3.2 The propagation of the wave inside a photonic crystal solved by FDTD method

Within a meshed surface each mesh has its own scalar constants such as the permittivity, ε, permeability, μ, conductivity, σ and vectorial variables such as $\vec{E}_x, \vec{E}_y$ and $\vec{H}_z$ for TE wave or $\vec{H}_x, \vec{H}_y$ and $\vec{E}_z$ for TM wave. Meshing can be thought as forming arrays holding the numerical values of these constants and variables. Consider we have a two dimensional grid of size 200 x 250 meshes. We have to allocate a 200 x 250 array in memory for each constant ε, μ, σ, and a 200 x 250 array for each field variable $\vec{E}_x, \vec{E}_y, \vec{H}_z$ for TE ($\vec{H}_x, \vec{H}_y, \vec{E}_z$ for TM) so the total is 6x200x250=3x10^5 memory locations. Field variables $\vec{H}$ and $\vec{E}$ will be continuously updated in each time step according to the difference equations as it is shown below.

3.3 The Yee Algorithm

3.3.1 The Maxwell's Equations

Maxwell's equations in three dimensions are as follows:

$$\frac{\partial \vec{H}_x}{\partial t} = \frac{1}{\mu}\left[\frac{\partial \vec{E}_y}{\partial z} - \frac{\partial \vec{E}_z}{\partial y} - (\vec{M}_x + \sigma^* \vec{H}_x)\right] \tag{3.1}$$

$$\frac{\partial \vec{H}_y}{\partial t} = \frac{1}{\mu}\left[\frac{\partial \vec{E}_z}{\partial x} - \frac{\partial \vec{E}_x}{\partial z} - (\vec{M}_y + \sigma^* \vec{H}_y)\right] \tag{3.2}$$

$$\frac{\partial \vec{H}_z}{\partial t} = \frac{1}{\mu}\left[\frac{\partial \vec{E}_x}{\partial y} - \frac{\partial \vec{E}_y}{\partial x} - (\vec{M}_z + \sigma^* \vec{H}_z)\right] \tag{3.3}$$

$$\frac{\partial \vec{E}_x}{\partial t} = \frac{1}{\varepsilon}\left[\frac{\partial \vec{H}_z}{\partial y} - \frac{\partial \vec{H}_y}{\partial z} - (\vec{J}_x + \sigma \vec{E}_x)\right] \tag{3.4}$$

$$\frac{\partial \vec{E}_y}{\partial t} = \frac{1}{\varepsilon}\left[\frac{\partial \vec{H}_x}{\partial z} - \frac{\partial \vec{H}_z}{\partial x} - (\vec{J}_y + \sigma \vec{E}_y)\right] \tag{3.5}$$

$$\frac{\partial \vec{E}_z}{\partial t} = \frac{1}{\varepsilon}\left[\frac{\partial \vec{H}_y}{\partial x} - \frac{\partial \vec{H}_x}{\partial y} - (\vec{J}_z + \sigma \vec{E}_z)\right] \tag{3.6}$$

where the parameters are,

$\vec{E}_i$ electric field pointing direction $\hat{i}$

$\vec{H}_i$ magnetic field pointing direction $\hat{i}$

$\vec{J}_i$ electric current density in direction $\hat{i}$

$\vec{M}_i$ equivalent magnetic current density in direction $\hat{i}$

μ magnetic permeability

ε electric permittivity

σ electric conductivity

σ^* equivalent magnetic loss

If we assume that the medium of interest is uniform in the z direction, we can set all $\frac{\partial}{\partial z}$ terms to zero. This leads us to Maxwell's equations in two dimensions:

$$\frac{\partial \vec{H}_x}{\partial t} = -\frac{1}{\mu}\left[\frac{\partial \vec{E}_z}{\partial y} + (\vec{M}_x + \sigma^* \vec{H}_x)\right] \tag{3.7}$$

$$\frac{\partial \vec{H}_y}{\partial t} = \frac{1}{\mu}\left[\frac{\partial \vec{E}_z}{\partial x} - (\vec{M}_y + \sigma^* \vec{H}_y)\right] \tag{3.8}$$

$$\frac{\partial \vec{E}_z}{\partial t} = \frac{1}{\varepsilon}\left[\frac{\partial \vec{H}_y}{\partial x} - \frac{\partial \vec{H}_x}{\partial y} - (\vec{J}_z + \sigma \vec{E}_z)\right] \tag{3.9}$$

$$\frac{\partial \vec{E}_x}{\partial t} = \frac{1}{\varepsilon}\left[\frac{\partial \vec{H}_z}{\partial y} - (\vec{J}_x + \sigma \vec{E}_x)\right] \tag{3.10}$$

$$\frac{\partial \vec{E}_y}{\partial t} = -\frac{1}{\varepsilon}\left[\frac{\partial \vec{H}_z}{\partial x} + (\vec{J}_y + \sigma \vec{E}_y)\right] \tag{3.11}$$

$$\frac{\partial \vec{E}_x}{\partial t} = \frac{1}{\varepsilon}\left[\frac{\partial \vec{H}_z}{\partial y} - (\vec{J}_x + \sigma \vec{E}_x)\right] \tag{3.12}$$

By carefully looking at the equations (3.7) through (3.12), we see that we can split them into two separate sets of equations involving only $\vec{H}_z, \vec{E}_x, \vec{E}_y, \vec{J}_x, \vec{J}_y, \vec{M}_z$ and $\vec{E}_z, \vec{H}_x, \vec{H}_y, \vec{M}_x, \vec{M}_y, \vec{J}_z$. Solutions of these equations can be interpreted as two independent propagating fields as transverse magnetic (TM) and transverse electric (TE) modes. Equations (3.7), (3.8) and (3.9) correspond to TM mode and Equations (3.10), (3.11) and (3.12) correspond to TE mode. Below we consider the discretization of TM mode wave equations, and the discretization of TE mode wave equations are similar.

3.3.2 Discretization of TM mode

We will assume that the electric and magnetic current densities $\vec{J}_x, \vec{J}_y$ and $\vec{M}_z$ are zero. Under these assumptions (3.7) through (3.9) can be written as :

$$\frac{\partial \vec{H}_x}{\partial t} = -\frac{1}{\mu}\left[\frac{\partial \vec{E}_z}{\partial y} + \sigma^* \vec{H}_x\right] \tag{3.13}$$

$$\frac{\partial \vec{H}_y}{\partial t} = \frac{1}{\mu}\left[\frac{\partial \vec{E}_z}{\partial x} - \sigma^* \vec{H}_y\right] \tag{3.14}$$

$$\frac{\partial \vec{E}_z}{\partial t} = \frac{1}{\varepsilon}\left[\frac{\partial \vec{H}_y}{\partial x} - \frac{\partial \vec{H}_x}{\partial y} - \sigma \vec{E}_z\right] \tag{3.15}$$

The derivative terms $\frac{\partial \vec{E}_z}{\partial t}$, $\frac{\partial \vec{H}_y}{\partial x}$ and $\frac{\partial \vec{H}_x}{\partial y}$ are calculated as $\partial t \to 0$, $\partial x \to 0$ and $\partial y \to 0$. Since we will decimate both time and space we will assume finite time steps Δt and finite steps in x and y dimensions Δx, Δy. Therefore we sample vectorial variables such as $\vec{H}_x$ at discrete points of space and time and denote it as $\vec{H}_x(i.\Delta x, j.\Delta y, n.\Delta t)$ or in a more compact form $\vec{H}_x^n(i, j)$. This means the value $\vec{H}_x$ at spatial location $(i.\Delta x, j.\Delta y)$ at time $n.\Delta t$.

The Yee algorithm has two important concepts, first is the Yee cell which has interleaved coordinates and the second one is the leapfrog processing scheme. After presenting these concepts we will show how TM equations (3.13)-(3.15) are discretized.

3.3.2.1 The Yee Cell

The sampling points of the field variables $\vec{H}$ and $\vec{E}$ are chosen as shown in Fig. 3.3. Each field variable is surrounded by four fields of the other type. According to Maxwell's equations derivative of a field variable in time is related to the variable itself and to the space derivative of other field(s) in space.

For example it is seen in 3.15 that $\frac{\partial \vec{E}_z}{\partial t}$ is dependent on itself by the term $-\frac{\sigma}{\varepsilon}\vec{E}_z$ and to the derivative of $\vec{H}_x$ in y dimension by the term $\frac{1}{\varepsilon}\frac{\partial \vec{H}_x}{\partial y}$ and to the

derivative of $\vec{H}_y$ in x dimension by the term $\frac{1}{\varepsilon}\frac{\partial \vec{H}_y}{\partial x}$.

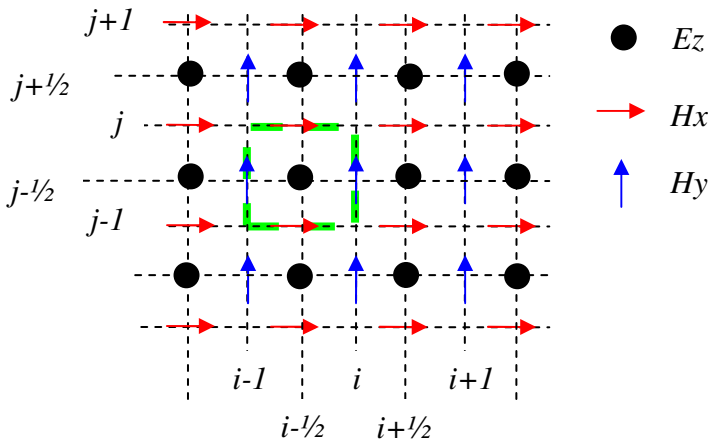

Fig. 3.3 The discretization in space and the Yee cell

While the field variable $\vec{E}_z$ is sampled at points $((k+½).\Delta x, (l+½).\Delta y)$, the field variable $\vec{H}_x$ is sampled at $((k+½).\Delta x,\ l.\Delta y)$ and $\vec{H}_y$ are sampled at $(k.\Delta x, (l+½).\Delta y)$, where $k,l \in \mathrm{Z}$.

In 3.15, in order to calculate the value of $\frac{\partial \vec{E}_z}{\partial t}$ at location $((i+½).\Delta x, (j+½).\Delta y)$ that is $\frac{\partial \vec{E}_z(i+½, j+½)}{\partial t}$, we also need the values of $\frac{\partial \vec{H}_x(i+½, j+½)}{\partial y}$ and $\frac{\partial \vec{H}_y(i+½, j+½)}{\partial x}$. Yee algorithm finds the values of these derivatives as:

$$\frac{\partial \vec{H}_x(i+½, j+½)}{\partial y} = \frac{\vec{H}_x(i+½, j+1) - \vec{H}_x(i+½, j)}{\Delta y} \tag{3.16}$$

and

$$\frac{\partial \vec{H}_y(i+½, j+½)}{\partial x} = \frac{\vec{H}_y(i+1, j+½) - \vec{H}_y(i, j+½)}{\Delta x} \tag{3.17}$$

The Yee cell concept shows us how to discretize derivatives of field variables in space. Now we will present the leapfrog processing scheme and see how the derivatives of field variables in time are discretized.

3.3.2.2 The Leapfrog Processing Scheme

Within one time step, Δt both $\vec{E}$ and $\vec{H}$ fields are updated. However they are not sampled at the same moment, rather in an interleaved scheme. In Yee's algorithm while the $\vec{H}$ fields are sampled at time intervals $n.\Delta t$ the $\vec{E}$ fields are sampled at $(n+½).\Delta t$, where $n \in Z$. However in equations (3.13) to (3.15) the field variables in the left hand side and in the right hand side are at the same time moment. To clarify this consider the moment $m.\Delta t$, where $m \in Z$. The field variables should satisfy the Maxwell's equation 3.15. If we write the time variable explicitly, 3.15 becomes

$$\frac{\partial \vec{E}_z^m}{\partial t} = \frac{1}{\varepsilon}\left[\frac{\partial \vec{H}_y^m}{\partial x} - \frac{\partial \vec{H}_x^m}{\partial y} - \sigma \vec{E}_z^m\right] \tag{3.18}$$

The exact values of $\vec{H}_y^m$ and $\vec{H}_x^m$ are known, however the values for $\frac{\partial \vec{E}_z^m}{\partial t}$ and $\vec{E}_z^m$ should be evaluated interpolating the values of $\vec{E}_z^{m+½}$ and $\vec{E}_z^{m-½}$. These are found by:

$$\frac{\partial \vec{E}_z^m(i+½, j+½)}{\partial t} = \frac{\vec{E}_z^{m+½}(i+½, j+½) - \vec{E}_z^{m-½}(i+½, j+½)}{\Delta t} \tag{3.19}$$

and

$$\vec{E}_z^m(i+½, j+½) = \frac{\vec{E}_z^{m+½}(i+½, j+½) + \vec{E}_z^{m-½}(i+½, j+½)}{2} \tag{3.20}$$

3.3.2.3 Combining Yee Cell and the Leapfrog Scheme

Now using the two equations brought by the interleaved coordinate concept and the two equations brought by leapfrog scheme we can discretize (3.15) as follows.

$$\frac{\partial \vec{E}_z^n(i+½, j+½)}{\partial t} =$$

$$\frac{1}{\varepsilon(i+½, j+½)}\left[\frac{\partial \vec{H}_y^{\,n}(i+½, j+½)}{\partial x} - \frac{\partial \vec{H}_x^{\,n}(i+½, j+½)}{\partial y} - \sigma(i+½, j+½).\vec{E}_z^{\,n}(i+½, j+½)\right] \tag{3.21}$$

$$\frac{\vec{E}_z^{\,n+½}(i+½,\, j+½) - \vec{E}_z^{\,n-½}(i+½,\, j+½)}{\Delta t} =$$

$$\frac{1}{\varepsilon(i+½,\, j+½)}\left[\frac{\vec{H}_y^{\,n}(i,\, j+½) - \vec{H}_y^{\,n}(i,\, j-½)}{\Delta x} - \frac{\vec{H}_x^{\,n}(i+½,\, j) - \vec{H}_x^{\,n}(i-½,\, j)}{\Delta y}\right] -$$

$$\frac{\sigma(i+½, j+½)}{\varepsilon(i+½, j+½)}\left[\frac{\vec{E}_z^{\,n+½}(i+½, j+½) + \vec{E}_z^{\,n-½}(i+½, j+½)}{2}\right] \tag{3.22}$$

Rearranging the terms, the equation simplifies to:

$$\vec{E}_z^{\,n+½}(i+½,\, j+½) =$$

$$\left(\frac{2\varepsilon - \Delta t.\sigma}{2\varepsilon + \Delta t.\sigma}\right)\vec{E}_z^{\,n-½}(i+½,\, j+½) + \left(\frac{2\Delta t}{\Delta x(2\varepsilon + \Delta t.\sigma)}\right)\left[\vec{H}_y^{\,n}(i,\, j+½) - \vec{H}_y^{\,n}(i,\, j-½)\right] -$$

$$\left(\frac{2\Delta t}{\Delta y(2\varepsilon + \Delta t.\sigma)}\right)\left[\vec{H}_x^{\,n}(i+½, j) - \vec{H}_x^{\,n}(i-½, j)\right] \tag{3.23}$$

Notice that in 3.23 the indices $(i+½, j+½)$ of constants ε and σ are not written for simplicity. In general these constants are sampled at the points same as the field variable at the left hand side of the equation.

Similarly (3.13) and (3.14) are discretized as

$$\frac{\vec{H}_x^{\,n+1}(i+\tfrac{1}{2},j)-\vec{H}_x^{\,n}(i+\tfrac{1}{2},j)}{\Delta t}=-\frac{1}{\mu}\left[\frac{\vec{E}_z^{\,n+\frac{1}{2}}(i+\tfrac{1}{2},j+\tfrac{1}{2})-\vec{E}_z^{\,n+\frac{1}{2}}(i+\tfrac{1}{2},j-\tfrac{1}{2})}{\Delta y}+\sigma^*\frac{\vec{H}_x^{\,n+1}(i+\tfrac{1}{2},j)+\vec{H}_x^{\,n}(i+\tfrac{1}{2},j)}{2}\right]$$

$$\vec{H}_x^{\,n+1}(i+\tfrac{1}{2},j)=\frac{2\Delta t}{\Delta y(2\mu+\Delta t\sigma^*)}\left[\vec{E}_z^{\,n+\frac{1}{2}}(i+\tfrac{1}{2},j+\tfrac{1}{2})-\vec{E}_z^{\,n+\frac{1}{2}}(i+\tfrac{1}{2},j-\tfrac{1}{2})\right]+\left(\frac{2\mu-\Delta t\sigma^*}{2\mu+\Delta t\sigma^*}\right)\vec{H}_x^{\,n}(i+\tfrac{1}{2},j)\qquad(3.24)$$

and

$$\frac{\vec{H}_y^{\,n+1}(i,j+\tfrac{1}{2})-\vec{H}_y^{\,n}(i,j+\tfrac{1}{2})}{\Delta t}=\frac{1}{\mu}\left[\frac{\vec{E}_z^{\,n+\frac{1}{2}}(i+\tfrac{1}{2},j+\tfrac{1}{2})-\vec{E}_z^{\,n+\frac{1}{2}}(i-\tfrac{1}{2},j+\tfrac{1}{2})}{\Delta x}-\sigma^*\frac{\vec{H}_y^{\,n+1}(i,j+\tfrac{1}{2})+\vec{H}_y^{\,n}(i,j+\tfrac{1}{2})}{2}\right]$$

$$\vec{H}_y^{\,n+1}(i,j+\tfrac{1}{2})=\frac{2\Delta t}{\Delta y(2\mu+\Delta t\sigma^*)}\left[\vec{E}_z^{\,n+\frac{1}{2}}(i+\tfrac{1}{2},j+\tfrac{1}{2})-\vec{E}_z^{\,n+\frac{1}{2}}(i-\tfrac{1}{2},j+\tfrac{1}{2})\right]+\left(\frac{2\mu-\Delta t\sigma^*}{2\mu+\Delta t\sigma^*}\right)\vec{H}_y^{\,n}(i,j+\tfrac{1}{2})\qquad(3.25)$$

In both 3.24 and 3.25 the constants μ and σ^* are sampled at the points same as the field variables at the left hand side of the equations. The discretization of the TE mode can be obtained with a similar procedure.

During computation the values for the vectorial variables $\vec{H}_x^{\,0}$, $\vec{H}_y^{\,0}$ and $\vec{E}_z^{\,-\frac{1}{2}}$ are given when initializing the corresponding arrays. The computation is carried on updating first the electric field variable $\vec{E}_z$ and then magnetic field variables, $\vec{H}_x$ and $\vec{H}_y$ or first the magnetic field variables and then the electric field variables for desired number of time steps. This is what the superscript denoting time such as n or $n+1$ in (3.23) to (3.25) implies.

Generally a source is used in the simulations. Defining a source is as simple as forcing the desired value to points in the grid considered as source, at each time step. The source can be a point or a line source or it can have any arbitrary shape. Fig. 3.4 shows a simulation result where there is a point source transmitting a second derivative Gaussian monopulse. The transmitted pulse reflects from a metallic circular target represented with a black spot as shown in the figure.

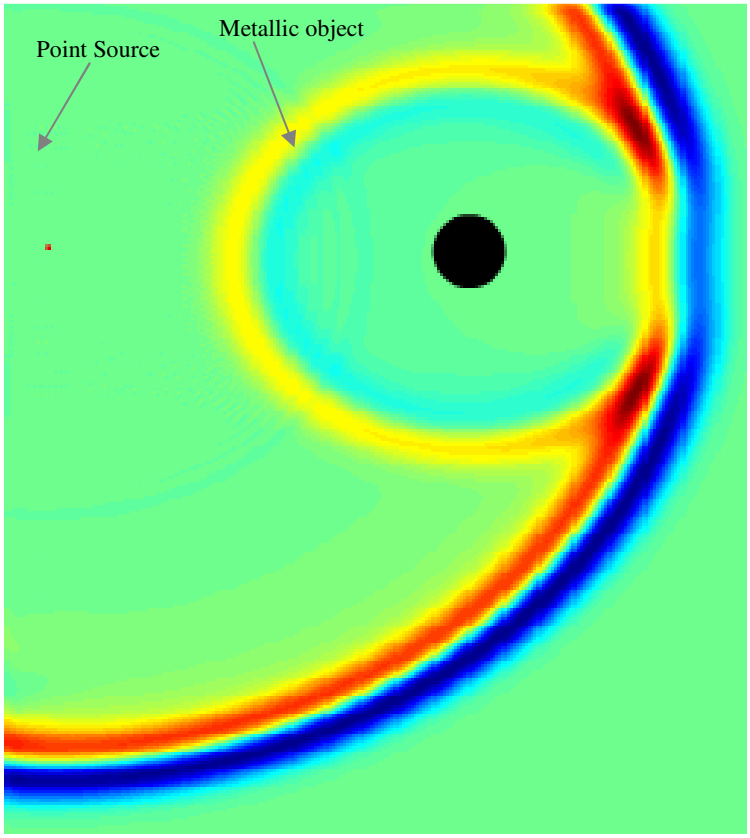

Fig. 3.4 A snapshot from FDTD simulation

3.4 Absorbing Boundary Conditions

Finite difference equations are solved for a finite computational domain. As the size of the computational area therefore the number of cells in the grid increases more computational time is required. However there is a way to emulate infinitely extending homogeneous mediums by defining a number of layers. If the region extends uniformly towards infinity, the impinging wave would not reflect back. This type of layers often used at the outermost edges of the computational domain are called Absorbing Boundary Layers and behaves as if the outermost regions were extending towards infinity by not reflecting back the incident fields.

Although there are various Absorbing Boundary Layer implementations such as Bayliss-Turkel, Trefethen-Halpern, Mur described in [30], however we will consider only Berenger's Perfectly Matched Layer Absorbing Boundary Conditions which is widely used and is efficient.

3.4.1 Perfectly Matched Layer Absorbing Boundary Conditions

Berenger proposed non-physical layers of cells defined at the edges of the computational domain as shown in Fig. 3.5 having special electrical conductances σ_x, σ_y and magnetic conductances σ_x^*, σ_y^* to absorb incident waves from all angles and for any frequency. Berenger's "split field" formulation of Maxwell's equations for a TM wave is as follows:

$$\mu \frac{\partial \vec{H}_x}{\partial t} + \sigma_y^* \vec{H}_x = -\frac{\partial \vec{E}_z}{\partial y} \tag{3.26}$$

$$\mu \frac{\partial \vec{H}_y}{\partial t} + \sigma_x^* \vec{H}_y = \frac{\partial \vec{E}_z}{\partial x} \tag{3.27}$$

$$\varepsilon \frac{\partial \vec{E}_{zx}}{\partial t} + \sigma_x \vec{E}_{zx} = \frac{\partial \vec{H}_y}{\partial x} \tag{3.28}$$

$$\varepsilon \frac{\partial \vec{E}_{zy}}{\partial t} + \sigma_y \vec{E}_{zy} = -\frac{\partial \vec{H}_y}{\partial x} \tag{3.29}$$

$$\vec{E}_z = \vec{E}_{zx} + \vec{E}_{zy} \tag{3.30}$$

where σ_i is the electric conductivity for the wave component in direction $\hat{\imath}$ and σ_i^* is the magnetic conductivity for the wave component in direction $\hat{\imath}$. Each cell in the computational domain holds six constants $\varepsilon, \mu, \sigma_x, \sigma_x^*, \sigma_y$ and σ_y^*. Notice that if we set $\sigma_x = \sigma_y$ and $\sigma_x^* = \sigma_y^*$, these equations are equivalent to Maxwell's equations presented in section 3.3.2. Therefore inside the medium excluding the boundary layers all physical materials should have $\sigma_x = \sigma_y$ and $\sigma_x^* = \sigma_y^*$.

In order to ensure that there is no reflection from the inner boundary following conditions should be satisfied

- $$\sigma_x^* = \frac{\mu_0}{\varepsilon_0}\sigma_x \tag{3.31a}$$

$$\sigma_y^* = \frac{\mu_0}{\varepsilon_0}\sigma_y \tag{3.31b}$$

- PML regions L,R,U,D and C should have the values of $\sigma_x, \sigma_x^*, \sigma_y, \sigma_y^*$ as written in Fig. 3.5.

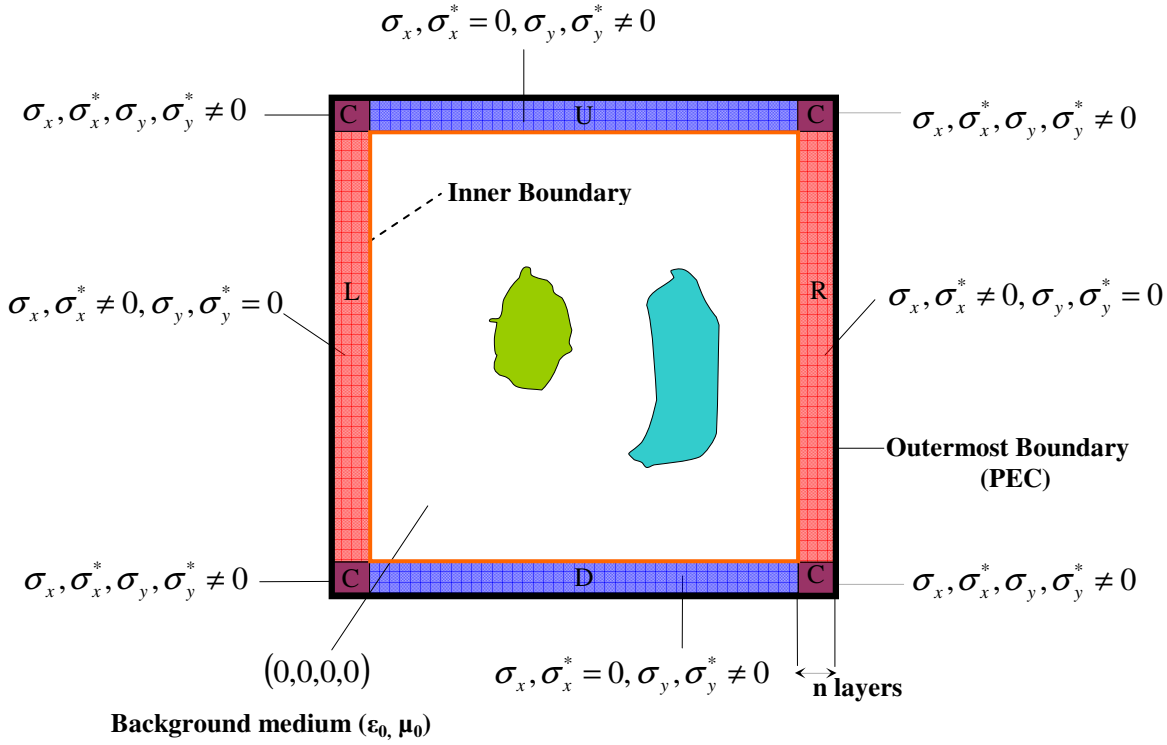

Fig. 3.5 The bondary layers and the values for conductivities at each boundary layer

The boundary layers L,R,U,D and C are non-physical because they exhibit different conductances in x and y directions. The values of σ_x, σ_x^* and σ_y, σ_y^* are increasing exponentially from interior boundary to exterior boundary starting from zero. For boundaries L and D this is illustrated in Fig. 3.6. In regions C the values of both and σ_y, σ_y^* are nonzero and they follow the values of their adjacent regions. Remember that σ_x^* and σ_y^* also satisfies (3.31). In regions C, while σ_x, σ_x^* increases exponentially in x direction and remains constant in y, σ_y, σ_y^* increases exponentially in y direction and remains constant in x. The profile of σ_x is drawn in detail in Fig. 3.6 for the boundary region L. Any monotonically increasing function can be used for the profile of conductivities, however their performance vary. A commonly used one is:

$$\sigma_x = \sigma_{x,\max} \cdot \left(\frac{x'}{nPML} \right)^2 \tag{3.32}$$

where x' is a newly defined coordinate as shown in Fig. 3.6 and *nPML* is the number of perfectly matched layers. For the remaining boundaries similar coordinates (starting at the interior boundary and increased towards exterior) are defined. Also $\sigma_{x,\max}$ is given by

$$\sigma_{x,\max} = -\log(\gamma)\sqrt{\frac{\varepsilon_0}{\mu_0}}.\frac{1}{\delta} \tag{3.33}$$

where γ is the desired reduction in amplitude when the wave moves a distance δ. Another important thing is that the values of electric fields $\vec{E}_{zx}$ and $\vec{E}_{zy}$ at the outermost cells of the computational domain which are indicated with thick black lines are enforced to zero throughout the simulation. Therefore the incident wave on the perfectly matched layers is attenuated gradually until they reach the outermost boundary which can be accounted as a perfect electrical conductor (PEC). Therefore the wave reflects back from the perfect electric conductor and keeps on attenuating again while traveling backwards in the boundary layers. Typical value for the reflection coefficient for a sixteen cell thick Berenger's perfectly matched layer is -110dB [30].

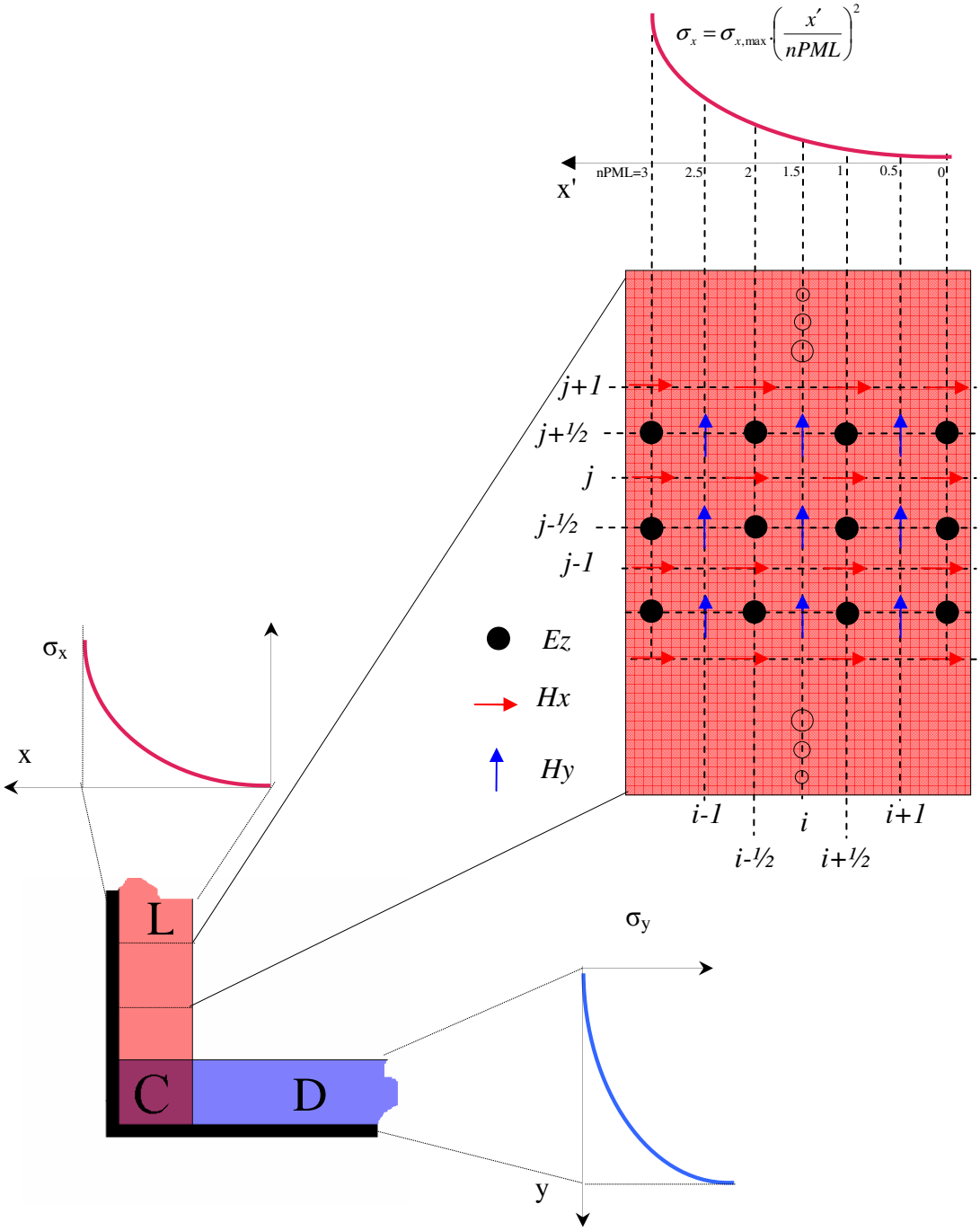

Fig. 3.6 The profile of conductivity in boundary layers

In order to discretize split field Maxwell's equations, this time we will use exponential differentiation [32] given by the formula:

$$\alpha.\frac{d\vec{A}^{n+½}}{dt}+\beta.\vec{A}^{n+½}\approx\beta\frac{\vec{A}^{n+1}-\vec{A}^{n}e^{-\beta dt/\alpha}}{1-e^{-\beta dt/\alpha}} \tag{3.34}$$

As in section 3.3.2.2 $\vec{H}$ fields are sampled at time intervals $n.\Delta t$ the $\vec{E}$ fields are sampled at $(n+½).\Delta t$, where $n\in \mathrm{Z}$. The Yee cell used here will be the same shown in Fig. 3.3. We discretize equation (3.26) at point $((i-½).\Delta x, j..\Delta y)$ and at time $(n+½).\Delta t$ as:

$$\frac{\partial \vec{H}_x^{n+½}(i-½,j)}{\partial t}+\frac{\sigma_y^*}{\mu}\vec{H}_x^{n+½}(i-½,j)=-\frac{1}{\mu}\frac{\partial \vec{E}_z^{n+½}(i-½,j)}{\partial y} \tag{3.35}$$

We started with $\vec{H}_x$ sampled at time interval $(n+½).\Delta t$ so that by using same interpolation method shown in equations (3.19), (3.20), we get $\vec{H}_x$ at time intervals $n.\Delta t$ and $(n+1).\Delta t$ which are the actual sampling points of the $\vec{H}$ fields. Discretizing in space and the time, we obtain

$$\frac{\sigma_y^*}{\mu}\left[\frac{\vec{H}_x^{n+1}(i-½,j)-\vec{H}_x^{n}(i-½,j)e^{-\frac{\sigma_y^*}{\mu}dt}}{1-e^{-\frac{\sigma_y^*}{\mu}dt}}\right]=-\frac{1}{\mu}\left[\frac{\vec{E}_z^{n+½}(i-½,j+½)-\vec{E}_z^{n+½}(i-½,j-½)}{\Delta y}\right] \tag{3.36}$$

Simplifying further for $\vec{H}_x^{n+1}(i-½,j)$ results in

$$\vec{H}_x^{n+1}(i-½,j)=-\frac{1-e^{-\frac{\sigma_y^*}{\mu}dt}}{\sigma_y^*\Delta y}\left[\vec{E}_z^{n+½}(i-½,j+½)-\vec{E}_z^{n+½}(i-½,j-½)\right]+\vec{H}_x^{n}(i-½,j)e^{-\frac{\sigma_y^*}{\mu}dt} \tag{3.37}$$

Similarly equations (3.27), (3.28) and (3.29) can be discretized as.

$$\vec{H}_y^{n+1}(i,j-½)=\frac{1-e^{-\frac{\sigma_y^*}{\mu}dt}}{\sigma_y^*\Delta x}\left[\vec{E}_z^{n+½}(i+½,j+½)-\vec{E}_z^{n+½}(i-½,j-½)\right]+\vec{H}_y^{n}(i,j-½)e^{-\frac{\sigma_y^*}{\mu}dt} \tag{3.38}$$

$$\vec{E}_{zx}^{n+½}(i-½,j-½)=\frac{1-e^{-\frac{\sigma_x}{\varepsilon}dt}}{\sigma_x\Delta x}\left[\vec{H}_y^{n}(i,j-½)-\vec{H}_y^{n}(i-1,j-½)\right]+\vec{E}_{zx}^{n-½}(i-½,j-½)e^{-\frac{\sigma_x}{\varepsilon}dt} \tag{3.39}$$

$$\vec{E}_{zy}^{n+½}(i-½,j-½)=-\frac{1-e^{-\frac{\sigma_y}{\varepsilon}dt}}{\sigma_y\Delta x}\left[\vec{H}_x^{n}(i-½,j)-\vec{H}_x^{n}(i-½,j-1)\right]+\vec{E}_{zy}^{n+½}(i-½,j-½)e^{-\frac{\sigma_y}{\varepsilon}dt} \tag{3.40}$$

$$\vec{E}_z^{\,n+½}(i-½, j-½) = \vec{E}_{zx}^{\,n+½}(i-½, j-½) + \vec{E}_{zy}^{\,n+½}(i-½, j-½) \quad (3.41)$$

In each equation the constant variables μ,ε, σ_x , σ_y, σ_x^* and σ_y^* are sampled at the same points as the field variable in left and side of the equation. Another important point is that in defining a source of electric field $\vec{E}_z$ both $\vec{E}_{zx}$ and $\vec{E}_{zy}$ must be assigned the same value.

Berenger's perfectly matched layers are one of the most commonly used absorbing boundaries in FDTD simulations. There is also a more simplified formulation of Berenger's perfectly matched layers, which is proposed by Chew and Weedon [33]. In this formulation the fields are not split in to its orthogonal components such as the ones we used $\vec{E}_{zx}$ and $\vec{E}_{zy}$. Also it enables the implementation of PML in cylindrical or spherical coordinates. In this context we have only considered the implementation of PMLs in two dimensions for transverse magnetic case. Readers who are interested in further implementations of PMLs can look at [30].

3.5 Numerical Dispersion

In FDTD the wave equations are discretized and therefore the resultant "numerical waves" are approximations of real ones. The difference equations of FDTD asymptotically converges to the Maxwell's equations when $\Delta x \to \delta x$, $\Delta y \to \delta y$ and $\Delta t \to \delta t$. There are errors introduced as a result of discretization. One of them is numerical dispersion error. Due to numerical dispersion the velocity of the wave can be different then the actual velocity or the velocity of the propagating wave can vary according to its direction of propagation with respect to major grid axis. The latter one is illustrated in Fig. 3.7. Wave B propagating with an angle to the axes of the grid lags wave A which is traveling along the x axis, due to numerical dispersion error. Typically the waves traveling along the grid diagonals are about 0.2% slower than wave propagating along the axes of the grid x and y. A detailed analysis of numerical dispersion error and methods to reduce this can be found in [30]

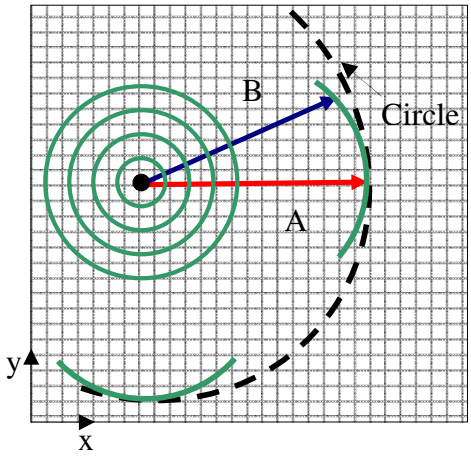

Fig. 3.7 Illustration of the numerical dispersion effect

3.6 Numerical Stability

In FDTD simulations when the stability conditions are not satisfied a numerical error grows rapidly as simulation time evolves and causes unphysical results. In this context we will only consider the stability problem of Yee algorithm in Cartesian coordinates due to time steps not being small enough. This is given by Courant stability condition. In general stability can occur due to boundary conditions, variable and unstructured meshing, lossy, dispersive, nonlinear, gain materials [30].

For two dimensional square lattice grid, Courant stability condition is given by:

$$c\frac{\Delta t}{\Delta x} \le \frac{1}{\sqrt{2}} \tag{3.42}$$

Readers who are willing to find a more detailed analysis of generalized numerical instability problems are suggested to consult [30].

CHAPTER 4

PROCESSING ALGORITHMS

4.1 Background

The processing algorithms explained below require a basic knowledge of uniform linear antenna arrays. Therefore we will first present the concept of Uniform Linear Antenna arrays (ULA).

4.1.1 Uniform Linear Antenna Arrays

Uniform Linear Antenna Array consists of multiple antennas usually identical, aligned in a line with uniform spacing. Fig. 4.1 shows an ULA of six elements and two point sources. The sources emit Gaussian monocycles as shown in the figure.

As the distance between the receiver array and the source increases the impinging wave on the receiver array approximates to a plane wave. Below we show analytically the output of a uniform linear array of receivers when a plane wave of frequency f_0 is incident with an angle θ with respect to antenna axis normal as shown in Fig. 4.2.

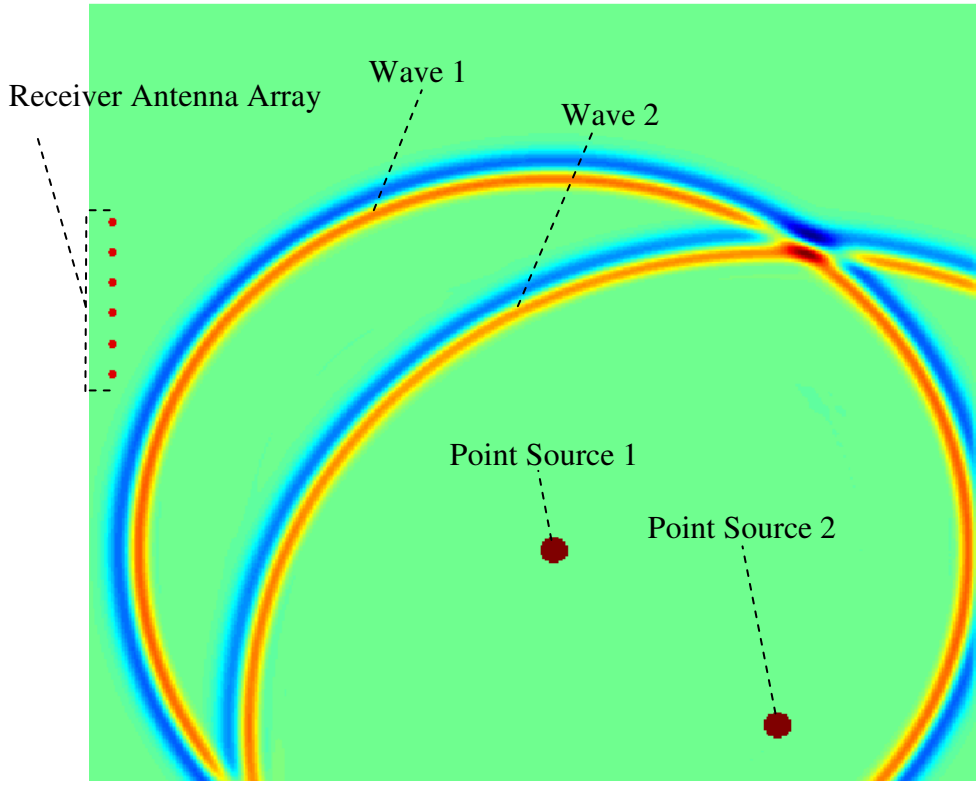

Fig 4.1 Two waves emitted from point sources having different distances to the receiver array

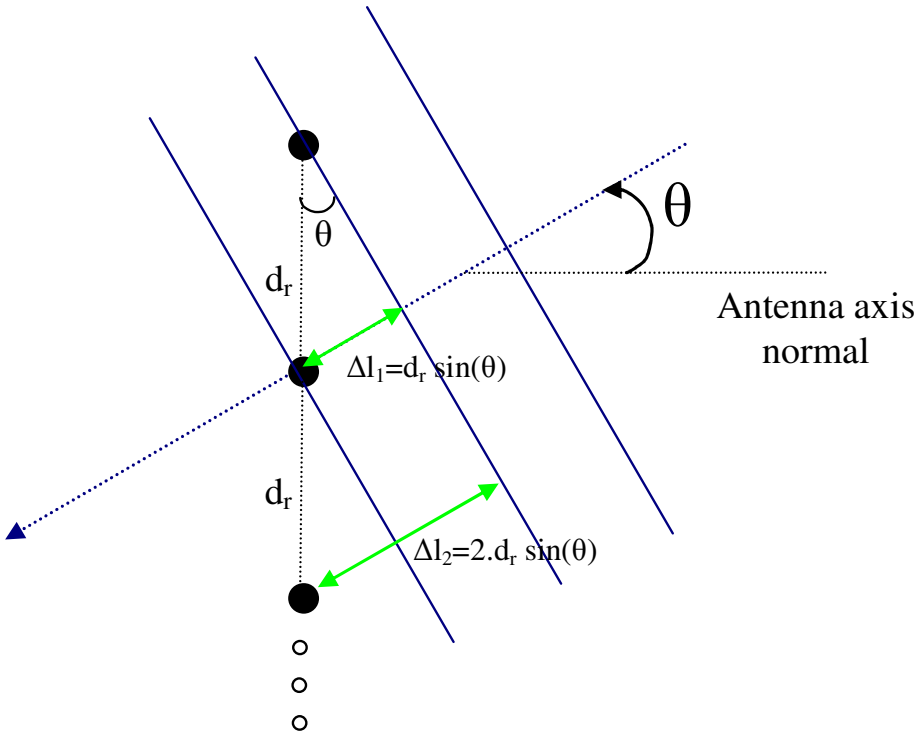

Fig. 4.2 Plane wave impinging on uniform linear array of antennas with an angle θ with respect to antenna axis normal

From trigonometry the phase difference between consecutive elements of the array is constant and given by

$$\Delta\phi = \frac{2\pi . f_0 d_r}{c_0} \sin(\theta) \tag{4.1}$$

where c_0 is the phase velocity of the impinging wave. Notice that the maximum magnitude of the phase shift is $\pm\frac{2\pi . f_0 d_r}{c_0}$ when $\theta = \pm\frac{\pi}{2}$. Since there is only one plane wave impinging, the output of the receiver array having *N* receivers can be written in phasor form as

$$s = \alpha . \left[1, e^{-j\Delta\phi}, e^{-j2\Delta\phi}, \ldots, e^{-j(N-1)\Delta\phi} \right]^T \tag{4.2}$$

where α is a complex number representing the amplitude and phase of the received signal by the first array element. If there are *M* plane waves impinging on the array at different angles, the output of the array is the superposition of the resultant outputs of the array for each individual plane wave.

$$s = s_1 + s_1 + \ldots s_M \tag{4.3}$$

where s_i is related with α_i and $\Delta\phi_i$ of i^{th} target according to (4.2).

After this brief review of uniform linear antenna arrays we will present the processing algorithms.

4.2 Multiple Signal Classification (MUSIC) Algorithm

Multiple Signal Classification (MUSIC) algorithm is firstly proposed by Ralph O. Schmidt, in 1981 in his thesis [34]. It is in the class of subspace based methods [35] and is also referred as a super resolution algorithm by its ability the distinguish target positions better than the classical limit which is half the wavelength of the processing frequency. MUSIC Algorithm was developed for detecting the directions of multiple emitters. Various preprocessing steps before applying MUSIC have been developed such as spatial smoothing techniques [36], [37] for better handling of correlated sources, using higher order cumulants to reduce the effect of noise [38] or correlation transformation using focusing matrices to combine multiple frequencies

[39], [40]. MUSIC algorithm can also be used in finding the time of arrivals of the multiple echoes in a waveform [41]. In this thesis we will consider both finding the directions of multiple targets and also finding the time of arrivals of the multiple echoes. Later we will present the Time Reversal MUSIC algorithm [42] which is applicable in radar applications where all received signals are correlated and classical MUSIC algorithm fails to locate targets.

4.2.1 Direction of Arrival (DOA) Estimation

In this section we will provide the mathematical model of the MUSIC algorithm for finding the directions of source using an array of receiver. This mathematical model can also be found in [36]. At the end of this section we included some numerical examples.

Consider waves from sources in different locations impinge on a uniform linear array (ULA) of n receivers. There are three basic assumptions:

1. All the sources are at frequency f_0,

2. Sources are distant enough from the receiver array so that received signals can be assumed as plane waves.

3. The incident signals and the noise are uncorrelated.

To summarize the procedure, first an *NxN* cross correlation matrix of receiver antenna outputs in phasor domain is formed, where *N* is the number of antennas. Then this cross correlation matrix is decomposed into its eigenvectors. *M* of these eigenvectors are "signal eigenvectors" and the remaining *N-M* are "noise eigenvectors". The number *M* can be determined at this step by looking at the multiplicity of the smallest eigenvalue. Signal eigenvectors span the space called signal subspace and similarly noise eigenvectors span the noise subspace. These two subspaces are orthogonal to each other. The locations of the sources are found by projecting "angle scanning vectors" to the noise subspace. An angle scanning vector is the expected output of the receiver array due to a source at corresponding angle. The projections resulting in zero will provide the solutions for the angles of the sources.

Mathematical model of the MUSIC algorithm is as follows. The received signal at each receiver can be written as the sum of all the impinging waves from all of the sources, that is,

$$\tilde{s}_n = \tilde{w}_n + \sum_{m=1}^{M} \tilde{u}_m . \exp(-j . \frac{2\pi f_0}{c_0} (n-1) . d_r \sin(\theta_m)) \ , \qquad n = 1,2,...,N \tag{4.4}$$

where the parameters are defines as follows:

$\tilde{s}_n$: Phasor of the output of n^{th} reveiver antenna.

$\tilde{w}_n$: Additive noise.

$\tilde{u}_m$: Phasor of wave coming from source m at the first receiver antenna.

M : Number of sources.

N : Number of receiver antennas of ULA.

d_r : distance between two consecutive antennas.

θ_m : Angle of m^{th} sources with respect to antenna axis.

c_0 : phase velocity of waves.

Notice that $\tilde{s_n}$ and $\tilde{u}_m$ and $\tilde{w}_m$ are in phasor domain. We can write equation (4.4) in matrix form as

$$\boldsymbol{S} = \boldsymbol{A}\boldsymbol{u} + \boldsymbol{w} \tag{4.5}$$

where

$$\boldsymbol{S} = [\tilde{s}_1 \ \tilde{s}_2 \ ... \ \tilde{s}_N]^T \tag{4.5.a}$$

$$\boldsymbol{A} = [\tilde{\boldsymbol{a}}_1 \ \tilde{\boldsymbol{a}}_2 \ ... \ \tilde{\boldsymbol{a}}_M] \tag{4.5.b}$$

$$\tilde{\boldsymbol{a}}_m = [1 \ e^{-j\beta_m} \ e^{-j2\beta_m} \ ... \ e^{-j(N-1)\beta_m}]^T \tag{4.5.c}$$

$$\beta_m = \frac{2\pi f_0}{c_0} d_r \sin(\theta_m) \tag{4.5.d}$$

$$\boldsymbol{u} = [\tilde{u}_1 \ \tilde{u}_2 \ ... \ \tilde{u}_M]^T \tag{4.5.e}$$

$$\boldsymbol{w} = [\tilde{w}_1 \ \tilde{w}_2 \ ... \ \tilde{w}_N]^T \tag{4.5.f}$$

The vector $\tilde{\boldsymbol{a}}_m$ is called the steering vector and the matrix $\boldsymbol{A}$ is called the array manifold.

The cross correlation matrix $\boldsymbol{R}_{SS}$ is given b

$$\boldsymbol{R}_{SS} = \mathcal{E}\{\boldsymbol{S}\boldsymbol{S}^H\} = \mathcal{E}\{(\boldsymbol{A}.\boldsymbol{u} + \boldsymbol{w})(\boldsymbol{A}.\boldsymbol{u} + \boldsymbol{w})^H\} \tag{4.6}$$

where $\mathcal{E}\{.\}$ is the expectation operator. In practice in order to find $\boldsymbol{R}_{SS} = \mathcal{E}\{\boldsymbol{S}\boldsymbol{S}^H\}$, only one snapshot, $\boldsymbol{S}_j$ of the antenna array output is not enough rather several independent snapshots are taken and they are averaged for obtaining an estimate.

$$\hat{\boldsymbol{R}}_{SS} = \frac{1}{J} \sum_{j=1}^{J} \boldsymbol{S}_j \boldsymbol{S}_j^H \tag{4.7}$$

where $\boldsymbol{J}$ is the number of snapshots taken. Using the third assumption which provides that the incident signals and the noise are uncorrelated, we can rewrite $\boldsymbol{R}_{SS}$ as

$$\boldsymbol{R}_{SS} = \boldsymbol{A}\,\mathcal{E}\{\boldsymbol{u}\boldsymbol{u}^{H}\}\boldsymbol{A}^{H} + \mathcal{E}\{\boldsymbol{w}\boldsymbol{w}^{H}\} = \boldsymbol{A}\boldsymbol{U}\boldsymbol{A}^{H} + \boldsymbol{W} \tag{4.8}$$

where $\boldsymbol{U} = \mathcal{E}\{\boldsymbol{u}\boldsymbol{u}^{H}\}$ is the covariance matrix of the sources and $\boldsymbol{W} = \mathcal{E}\{\boldsymbol{w}\boldsymbol{w}^{H}\}$ is the noise covariance matrix. If we assume zero mean, white Gaussian noise with variance σ^2 we can rewrite as:

$$\boldsymbol{R}_{SS} = \boldsymbol{A}\boldsymbol{U}\boldsymbol{A}^{H} + \sigma^{2}\boldsymbol{I} \tag{4.9}$$

where $\boldsymbol{I}$ is the identity matrix. If the sources are uncorrelated then $\boldsymbol{U}$ will be diagonal. On the other hand if completely correlated sources exist, $\boldsymbol{U}$ will be singular.

Now suppose that the number of antennas L is greater than the number of sources M and $\boldsymbol{U}$ is non-singular. Then will be singular and the rank of $\boldsymbol{A}\boldsymbol{U}\boldsymbol{A}^{H}$ will be M. Therefore the eigenvalues of $\boldsymbol{R}_{SS} = \boldsymbol{A}\boldsymbol{U}\boldsymbol{A}^{H} + \sigma^{2}\boldsymbol{I}$ will be:

$$\lambda_1 \geq \lambda_2 \geq \ldots \geq \lambda_M \geq \lambda_{M+1} = \lambda_{M+2} = \ldots = \lambda_N = \sigma^2 \tag{4.10}$$

Notice that the multiplicity of the smallest eigenvalue, σ^2 is *N-M*. Therefore the number of sources can be detected at this step utilizing the multiplicity of the smallest eigenvalue.

The subspace spanned by the *N-M* eigenvectors corresponding to eigenvalue σ^2 is called the noise subspace and is orthogonal to the signal subspace spanned by the *M* eigenvectors corresponding to the remaining *M* signal eigenvalues.

We will define a matrix $\boldsymbol{E}_{N}$ which contains noise eigenvectors in its columns. The square Euclidean distance of a vector $\tilde{\boldsymbol{a}}(\theta)$ to the signal subspace is given by

$$r^2 = \tilde{\boldsymbol{a}}^{H}(\theta)\boldsymbol{E}_{N}\boldsymbol{E}_{N}^{H}\tilde{\boldsymbol{a}}(\theta) \tag{4.11}$$

where $(.)^{H}$ is Hermitian transpose operator. Here θ is an arbitrary angle. The MUSIC spectrum, found by scanning the variable θ for all possible angles is given by

$$\boldsymbol{P}_{MU}(\theta) = \frac{1}{r^2} = \frac{1}{\tilde{\boldsymbol{a}}^{H}(\theta)\boldsymbol{E}_{N}\boldsymbol{E}_{N}^{H}\tilde{\boldsymbol{a}}(\theta)} \tag{4.12}$$

Whenever $\theta = \theta_m$, the direction of one of the source, the value of r^2 will be 0 since $\tilde{\boldsymbol{a}}(\theta_m)$ is orthogonal to noise subspace, and there will be a peak in the MUSIC spectrum.

The following figure, Fig. 4.3 shows the MUSIC spectrum at 150 MHz when there are six uncorrelated sources at angles -76˚, -30˚, -10˚, 0.5˚, 14˚ and 56˚. The

correlation matrix for this uncorrelated sources are found analytically using ideal matrices $\boldsymbol{A}$ and $\boldsymbol{U}$ and no noise is present. The uniform linear receiver array has eight elements with inter element spacing of 50cm. There the correlation matrix is eight by eight and has eight eigenvectors. Six of them are the basis vectors of the signal subspace and the remaining two are of the noise subspace. The two eigenvalues corresponding to two noise eigenvectors are zero since $\sigma = 0$. The values of the directions of sources are found exactly.

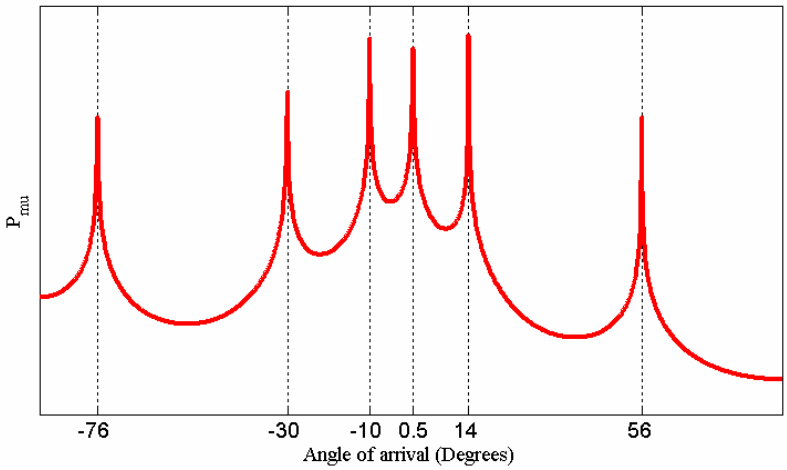

Fig. 4.3 Result of MUSIC algorithm for eight element ULA and six independent sources having angles -76˚, -30˚, -10˚, 0.5˚, 14˚ and 56˚

MUSIC algorithm also performs well when the targets directions are close. Fig. 4.4 shows the case for the same receiver arrangement, when the target angles are -30.6˚, -30˚, -29.5˚ and -29.2 ˚. The directions of sources are again found precisely.

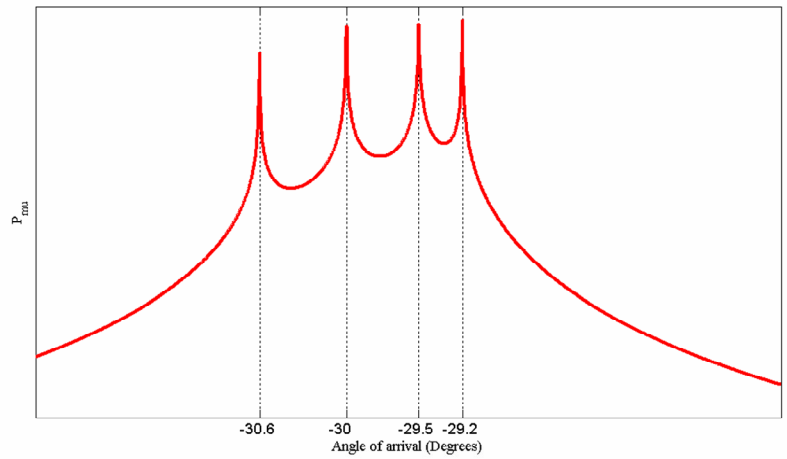

Fig. 4.4 Result of MUSIC algorithm for eight element ULA and four closely spaced independent sources having angles -30.6˚, -30˚, -29.5˚ and -29.2 ˚

If some of the sources are fully correlated, the number of signal eigenvalues will be less than the actual number of sources. The actual number of sources can not be determined using the multiplicity of the smallest eigenvalue. Therefore, the fully correlated sources can not be detected using MUSIC. In the first example where the sources were at angles -76˚, -30˚, -10˚, 0.5˚, 14˚ and 56˚, here the sources at -30˚ and -10˚ are assumed to be fully correlated while others are uncorrelated. There are three zero eigenvalues of the covariance matrix instead of two, which suggests that there are five targets in the environment. The MUSIC spectrum can be seen at Fig. 4.5. There are only four peaks found although the number of sources was chosen as five.

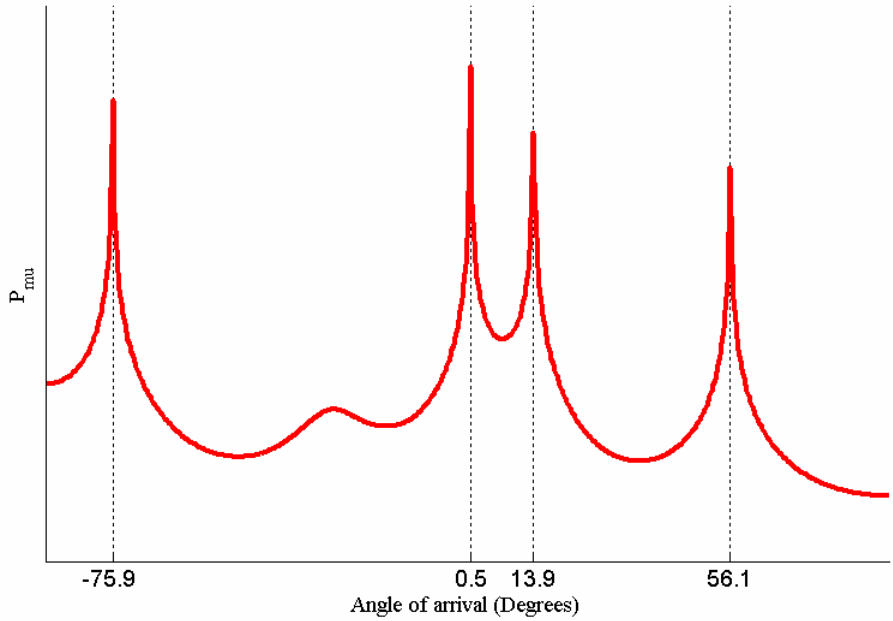

Fig. 4.5 Result of MUSIC algorithm for eight element ULA and six sources when a pair of sources at -30˚ and -10˚ are fully correlated.

As explained in [36] the existence of coherent sources can be determined noticing the inconsistency of the results of processing. Taking our case as an example we found that the multiplicity of the smallest eigenvalue (0 in this case since there is no noise) is found to be three, and therefore we expect to 8-3=5 peaks in the spectrum. However we found only four peaks. Therefore we can conclude that there exist coherent pairs.

In radar applications the signal reflected by the targets are fully correlated, which means that there will be only one signal eigenvalue. Therefore multiple target

detection will not be possible. However there are spatial smoothing techniques to overcome this problem of singularity of the source covariance matrix.

4.2.1.1 Spatial Smoothing

If fully correlated sources exist in the environment the source covariance matrix $\boldsymbol{U}$ becomes singular. We saw in the previous section that MUSIC fails to locate fully correlated sources. Spatial smoothing technique introduced by Evans et al. [43], is applied on the array outputs in order to "decorrelate" the sources. The procedure of spatial smoothing presented here can also be found in [36].

Assume that there are *N* elements in the ULA receiver array and these elements are divided into overlapping subgroups of length L as shown in Fig. 4.6.

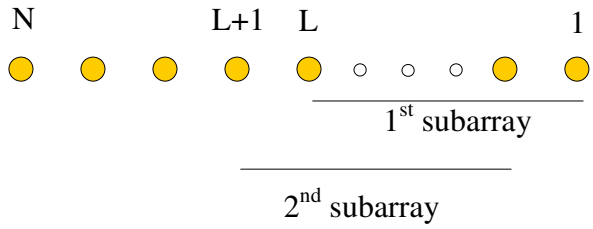

Fig. 4.6 The receiver array and subarrays

The steering vector of the k^{th} subarray of length *L* for the m^{th} target denoted by $\tilde{\boldsymbol{a}}_{\boldsymbol{m}}^{\boldsymbol{k}}$ is given by

$$\tilde{\boldsymbol{a}}_{\boldsymbol{m}}^{\boldsymbol{k}} = \left[\left(1 \;\; e^{-j\beta_m} \;\; e^{-j2\beta_m} \ldots \; e^{-j(L-1)\beta_m}\right) e^{-j(k-1).p.\beta_m}\right]^T \tag{4.13}$$

where *p* is the amount of shift between consecutive subarrays which is one in Fig. 4.6 and

$$\beta_m = \frac{2\pi f_0}{c_0} d_r \sin(\theta_m) \tag{4.14}$$

d_r being the distance between consecutive receiver antennas and θ_m is the direction of arrival of the signal reflected from the m^{th} target as in Fig. 4.2. The array manifold for the k^{th} subarray is represented by $\boldsymbol{A}_{\boldsymbol{k}} = \left[\tilde{\boldsymbol{a}}_{\boldsymbol{1}}^{\boldsymbol{k}} \tilde{\boldsymbol{a}}_{\boldsymbol{2}}^{\boldsymbol{k}} \ldots \tilde{\boldsymbol{a}}_{\boldsymbol{M}}^{\boldsymbol{k}}\right]$. The covariance matrix for k^{th} subarray is

$$\boldsymbol{R}_{\boldsymbol{SS}}^{\boldsymbol{k}} = \boldsymbol{A}_{\boldsymbol{k}} \boldsymbol{U} \boldsymbol{A}_{\boldsymbol{k}}^{\boldsymbol{H}} + \boldsymbol{W} \tag{4.15}$$

Again we assumed that the signals and the noise are independent from each other. $\boldsymbol{U}$ and $\boldsymbol{W}$ were defined in section 4.2.1.

The spatially smoothed covariance matrix is given by

$$\hat{\boldsymbol{R}}_{SS} = \frac{1}{K}\sum_{k=1}^{K} \boldsymbol{R}_{SS}^{k} \tag{4.16}$$

where K is the number of subarrays. After obtaining the spatially smoothed covariance matrix one can apply the MUSIC algorithm by decomposing the covariance matrix into its eigenvalues.

This technique required arrays having large number of elements. In our experiments we did not use this type of spatial smoothing since our array size is small. We will use an improved version of spatial smoothing in Delay Estimation MUSIC algorithm.

4.2.2 Delay Estimation MUSIC Algorithm

MUSIC algorithm can also be used the estimate the time of arrivals (TOA) of reflected echoes in a waveform as we have mentioned before. In the direction of arrival estimation using MUSIC, the phase difference of the echoes impinging on multiple receivers was used to estimate the direction of sources. Equivalent to multiple antennas in DOA estimation, in Delay Estimation MUSIC (DEM) algorithm multiple frequency information will be used. Therefore only one receiver antenna instead of an array is sufficient; however the experiment has to be performed for multiple frequencies. Now we will describe the mathematical model.

If there are M targets in the environment and a continuous wave of frequency f_n is transmitted from the transmitter. The received signal from the receiver will be

$$\tilde{s}_n = \tilde{w}_n + \sum_{m=1}^{M} \tilde{u}_m . \exp(-j.2\pi f_n . \tau_m) \tag{4.17}$$

where

$\tilde{s}_n$ **: Phasor of the receiver antenna output for** n^{th} **frequency.**
$\tilde{w}_n$ **: Additive noise.**
$\tilde{u}_m$ **:** *C***omplex reflectivity of the** m^{th}.
M **: Number of targets.**
τ_m **: Time of arrival of the echo coming from target** m**.**

Here the complex reflection coefficients of the targets, $\tilde{u}_m$ are assumed constant over the frequency range of interest. We can write the output of the receiver antenna for multiple frequencies as

$$\boldsymbol{S} = \boldsymbol{E}\boldsymbol{u} + \boldsymbol{w} \tag{4.18}$$

where

$$\boldsymbol{S} = \left[\tilde{s}_1 \ \tilde{s}_2 \ \ldots \tilde{s}_N\right]^T \tag{4.18.a}$$

$$\boldsymbol{E} = \left[\tilde{\boldsymbol{e}}_1 \ \tilde{\boldsymbol{e}}_2 \ \ldots \tilde{\boldsymbol{e}}_M\right] \tag{4.18.b}$$

$$\tilde{\boldsymbol{e}}_m = \tilde{\boldsymbol{e}}(\tau_{\boldsymbol{m}}) = \left[e^{-j\beta_1} \ e^{-j\beta_2} \ \ldots \ e^{-j\beta_N}\right]^T \tag{4.18.c}$$

$$\beta_n = 2\pi f_n . \tau_m \tag{4.18.d}$$

$$\boldsymbol{u} = \left[\tilde{u}_1 \ \tilde{u}_2 \ \ldots \tilde{u}_M\right]^T \tag{4.18.e}$$

$$\boldsymbol{w} = \left[\tilde{w}_1 \ \tilde{w}_2 \ \ldots \tilde{w}_N\right]^T \tag{4.18.f}$$

N is the number of frequency components used. Similar to the angle estimation case we need to compute the covariance matrix of, $\boldsymbol{R}_{SS} = \mathcal{E}\{\boldsymbol{S}\boldsymbol{S}^H\}$. In radar applications the phase and the amplitude of the received signals are the same independent of when the snapshot is taken, we can not estimate $\boldsymbol{R}_{SS}$ by averaging multiple snapshots. Averaging will only help eliminating the uncorrelated noise. Here we will neglect the effect of noise and write $\mathcal{E}\{\boldsymbol{S}\boldsymbol{S}^H\} = \boldsymbol{S}\boldsymbol{S}^H$. Since $\boldsymbol{S}$ is a vector, the rank of $\boldsymbol{R}_{SS}$ is one. Therefore it is not possible to detect multiple echoes in a waveform using this covariance matrix. This problem was also encountered in DOA estimation in section 4.2.1. The solution is equivalent, spatial smoothing method, but this time using multiple frequencies instead of multiple antennas.

We can define overlapping subvectors of the vector $\boldsymbol{S}$ having length *L* by

$$\boldsymbol{S}_k = \left[\boldsymbol{S}_{(k-1)p+1} \ \boldsymbol{S}_{(k-1)p+2} \ \ldots \ \boldsymbol{S}_{(k-1)p+L}\right]^T \tag{4.19}$$

where *p* is the amount of shift between consecutive subvectors. The covariance matrix of each subvector is $\hat{\boldsymbol{R}}_k = \boldsymbol{S}_k \boldsymbol{S}_k^H$. The choice of *L* is important. *L* should be greater than the number of targets to be detected. As *L* becomes larger DEM algorithm provides the TOA with higher resolution, however the performance of decorrelating the echoes in other words making $\boldsymbol{R}_{SS}$ non-singular, degrades [41]. The overall spatial smoothed covariance matrix is given by

$$\hat{\boldsymbol{R}}_{SS} = \frac{1}{K}\sum_{k=1}^{K}\left(\hat{\boldsymbol{R}}_k + \boldsymbol{J}\hat{\boldsymbol{R}}_k^{*}\boldsymbol{J}\right) \tag{4.20}$$

where $(.)^{*}$ represents the conjugate operator and

$$\boldsymbol{J} = \begin{bmatrix} 0 & \dots & 0 & 1 \\ \dots & \dots & 1 & 0 \\ 0 & \dots & \dots & \dots \\ 1 & 0 & \dots & 0 \end{bmatrix} \tag{4.21}$$

The operation $\boldsymbol{J}\hat{\boldsymbol{R}}_k^{*}\boldsymbol{J}$ rotates the matrix $\hat{\boldsymbol{R}}_k^{*}$ by 180 degree clockwise, so the result of $\hat{\boldsymbol{R}}_k + \boldsymbol{J}\hat{\boldsymbol{R}}_k^{*}\boldsymbol{J}$ is symmetric with respect to both diagonals. This smoothing process is called Modified Spatial Smoothing (MSS) [37]. The resultant covariance matrix $\boldsymbol{R}_{SS}$ is an *LxL* matrix which will be decomposed into its eigenvalues and eigenvectors. In this step the number of signal eigenvalues should be decided looking at the eigenvalues. In ideal cases the noise eigenvalues are significantly smaller than the signal eigenvalues. However due to noise or inefficiency of smoothing process they may be close to each other. So this is an estimation problem. If *L* is estimated to be larger than its actual value, in the spectrum there occur extra peaks. On the other hand, if *L* is chosen smaller, some of the actual peak will not be found [41]. Some methods for estimating *L* are also developed [44]. Using small values of *L* provides a better decorrelation performance and therefore a better distinction between the two sets of eigenvalues.

Since there are *M* signals *M* of the largest eigenvalues are signal eigenvalues and the remaining *L-M* are the noise eigenvalues. Signal eigenvectors that correspond to signal eigenvalues span the signal subspace and similarly noise eigenvectors span the noise subspace. These two subspaces are expected to be close to orthogonal depending on the performance of the decorrelation (smoothing) operation. If we define $\boldsymbol{E}_N$ as the matrix containing the noise eigenvectors in its columns, the MUSIC spectrum showing the likelihood of an echo versus time of arrival, τ is given by

$$\boldsymbol{P}_{MU}(\tau) = \frac{1}{\tilde{\boldsymbol{e}}^{H}(\tau)\boldsymbol{E}_N\boldsymbol{E}_N^{H}\tilde{\boldsymbol{e}}(\tau)} \tag{4.22}$$

Equation (4.22) will be referred to as the "temporal DEM spectrum". Whenever $\tau = \tau_m$ there will be a peak in the spectrum since $\tilde{\boldsymbol{e}}^{H}(\tau_m)\boldsymbol{E}_N \approx 0$.

The following figure, Fig. 4.7 shows the result of the delay estimation MUSIC method applied to the waveform seen in blue which is a real experimental data acquired by our radar prototype when there are two targets in the environment.

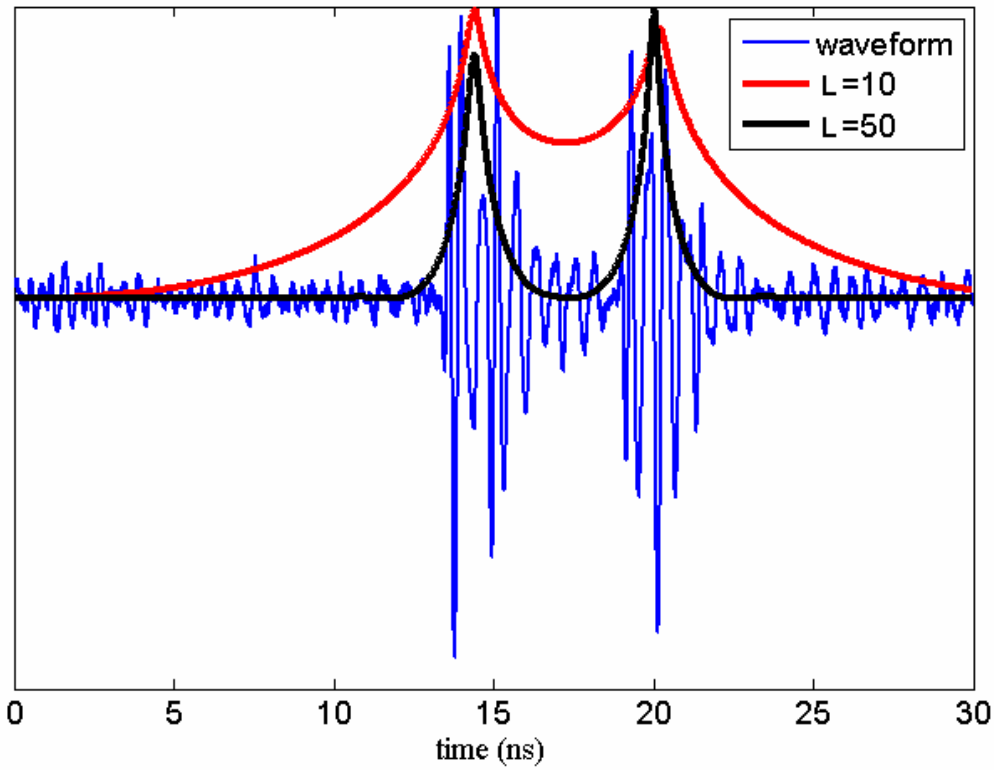

Fig. 4.7 Result of delay estimation MUSIC algorithm for different values of *L*

The increase in the value of *L* leads to sharper peaks however the computational time increases since the new covariance matrix is of size 50x50 instead of 10x10. As the covariance matrix increases in size, more computation time is needed eigen-decomposition of the matrix.

Fig. 4.8 shows another processing result when the echoes coming from the two targets are overlapped. For small values of *L*, the two targets can not be resolved. However when *L* is increases to 50 we can obtain two peaks. In cases where the number of echoes in the waveform are known *L* can be iteratively increased to reach the desired number of peaks.

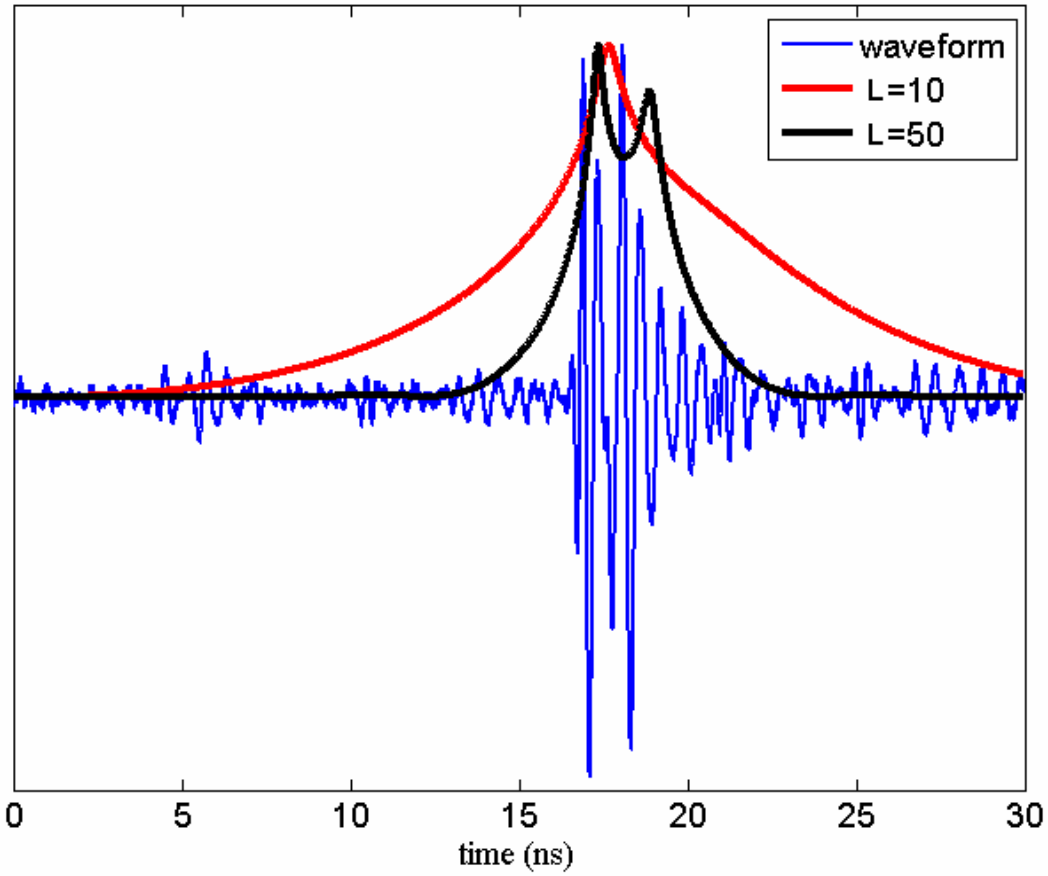

Fig. 4.8 Result of delay estimation MUSIC algorithm for different values of *L* when target echoes are overlapped

The time of arrival of an echo provides an ellipse as the possible locations of the target since the ellipse is defined as the locus of points in two dimensions where the sum of distances from every point to two fixed points called the foci are constant. TOA of an echo provides the distance the pulse traveled after being emitted by the transmitter antenna, being reflected by a target and being received by the receiver. Therefore the foci of the corresponding ellipse are the transmitter and the receiver antenna. Rather than providing an exact TOA for each echo, the temporal DEM spectrum of a received waveform shows the likelihood of an echo existing for a given TOA as shown in Fig. 4.7 or Fig. 4.8. Therefore each point in the DEM spectrum corresponds to an ellipse (in 2D problems and to a prolate spheroid in 3D problems) in space. Therefore when we map the DEM spectrum to space, we get the likelihoods of the existence of targets in spatial coordinates. We will refer this map as the "spatial DEM spectrum". Fig. 4.9 (a) depicts the mapping of temporal DEM spectrum to 2D space to obtain the spatial DEM spectrum. In the spatial DEM spectrum there occurs elliptic regions covering a certain

area in space having higher intensity than surroundings. We will refer to these regions as intense "elliptic bands". When we look at this plot from the top we see as shown in Fig 4.9 (b) we see higher intensity elliptic bands, locations that the targets are more likely to exist.

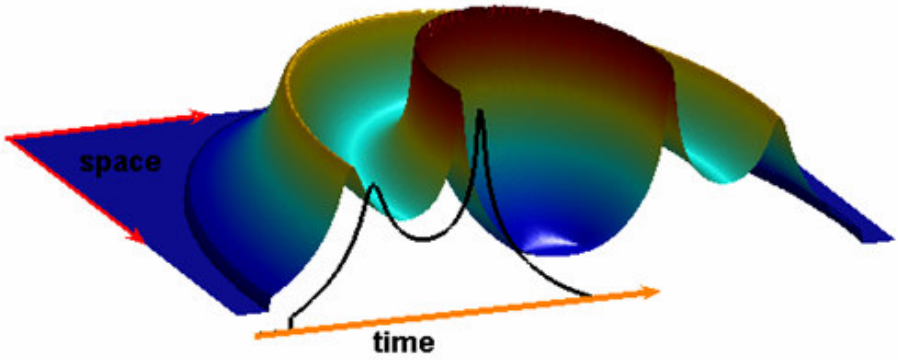

(a)

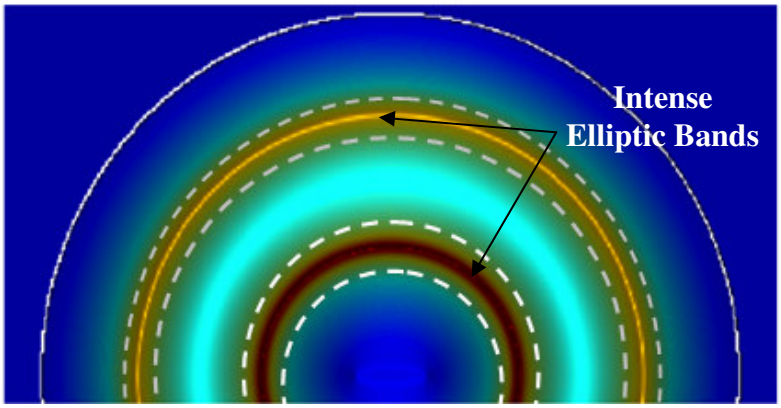

(b)

Fig. 4.9 (a) The conversion from temporal DEM spectrum to spatial DEM spectrum. **(b)** Top view of the same plot

There are also studies in which DOA MUSIC algorithm is applied to radar after spatially smoothing the acquired data by the method we saw in this section [45], [46].

4.3 Time Reversal MUSIC

Time Reversal MUSIC (TRM) algorithm is used in detecting multiple targets using multiple transmitter and multiple receiver antennas. It has been developed for ultrasound imaging [42] and is suitable to be used in radar applications. The name "Time Reversal" may evoke storing the received waveform, time reversing and

retransmitting into the medium which is a common technique used in acoustical imaging, however in TRM algorithm there is no re-transmission of the reversed signal. As we will explain later time reversing is done not physically but computationally. The process can be summarized as follows: First a continuous signal is transmitted from each transmitter one at a time. At each transmission step the receiver array output is stored as a vector in phasor form. Each of these vectors is a column of the so called multistatic matrix. Then the multistatic matrix is decomposed into its singular values and two noise subspaces are formed. One corresponds to the receiver array and the other to the transmitter array. The space where the imaging is performed is divided into meshes. For each point in the meshed space, transmitter and receiver steering vectors are calculated and projected to their corresponding noise subspaces to find the MUSIC spectrum.

4.3.1 Mathematical Formulation

Consider uniform linear arrays of receiver and transmitter antennas. These arrays can be in arbitrary positions. The Greens functions of the uniform medium is given by

$$G(\boldsymbol{r},\boldsymbol{r}') = \frac{1}{4\pi|\boldsymbol{r}-\boldsymbol{r}'|} e^{-j\beta|\boldsymbol{r}-\boldsymbol{r}'|} \tag{4.23}$$

where $\beta = \frac{2\pi f}{c_0}$ is the wavenumber. f is the frequency and c_0 is the phase velocity of the wave. $\boldsymbol{r}$ and $\boldsymbol{r}'$ are position vectors therefore $|\boldsymbol{r}-\boldsymbol{r}'|$ is the distance between points $\boldsymbol{r}$ and $\boldsymbol{r}'$. The N_R receivers are positioned at points $\boldsymbol{R}_1, \boldsymbol{R}_2 \ldots \boldsymbol{R}_{N_R}$ and N_T transmitters are positioned at $\boldsymbol{T}_1, \boldsymbol{T}_2 \ldots \boldsymbol{T}_{N_T}$.

The output of j^{th} receiver due to a source at $\boldsymbol{R}'$ radiating with unity amplitude can be represented by $G(\boldsymbol{R}_j, \boldsymbol{R}')$ and the output of the receiver array can be written in vector form as

$$\boldsymbol{g}_R(\boldsymbol{R}') = \left[G(\boldsymbol{R}_1,\boldsymbol{R}'), G(\boldsymbol{R}_2,\boldsymbol{R}'), \ \ldots\ , G(\boldsymbol{R}_{N_R},\boldsymbol{R}')\right]^T \tag{4.24}$$

The detected signal by receiver $\boldsymbol{j}$ when a unity amplitude signal is transmitted from i^{th} transmitter, reflecting from target $\boldsymbol{m}$ at $\boldsymbol{Q}_m$ is

$$v_m^j = \kappa_m G(\boldsymbol{Q}_m, \boldsymbol{T}_i) G(\boldsymbol{R}_j, \boldsymbol{Q}_m) \tag{4.25}$$

where κ_m is the complex scattering coefficient of the m^{th} target. If there are M targets in the environment and a unity amplitude signal is transmitted from i^{th} transmitter, the output of the j^{th} receiver can be derived from equation (4.23) as

$$v^j = \sum_{m=1}^{M} \kappa_m G(\boldsymbol{Q}_m, \boldsymbol{T}_i) G(\boldsymbol{R}_j, \boldsymbol{Q}_m) \tag{4.26}$$

This is the (i,j)-th entry of the multistatic response matrix $\boldsymbol{K}$, denoted as $\boldsymbol{K}_{ij}$. This means that j^{th} column of the multistatic response matrix is the receiver array output when a unity amplitude signal is transmitted from j^{th} transmitter. Multistatic response matrix can be formulated as

$$\boldsymbol{K} = \sum_{m=1}^{M} \kappa_m \boldsymbol{g}_R(\boldsymbol{Q}_m) \boldsymbol{g}_T(\boldsymbol{Q}_m) \tag{4.27}$$

$\boldsymbol{g}_T(\boldsymbol{R}')$ is defined similar to $\boldsymbol{g}_R(\boldsymbol{R}')$ as

$$\boldsymbol{g}_T(\boldsymbol{R}') = \left[G(\boldsymbol{R}', \boldsymbol{T}_1), G(\boldsymbol{R}', \boldsymbol{T}_2), \ \ldots, G(\boldsymbol{R}', \boldsymbol{T}_{N_T}) \right]^T \tag{4.28}$$

Notice that $\boldsymbol{g}_R$ and $\boldsymbol{g}_T$ are both column vectors. In practice the multistatic response matrix is formed by transmitting a unity amplitude signal from only one of the transmitters and recording the receiver array output. Each output is a column of $\boldsymbol{K}$.

Next step is applying singular value decomposition to the matrix $\boldsymbol{K}$. The singular system is given by

$$\boldsymbol{K}\boldsymbol{e}_p = \sigma_p \boldsymbol{v}_p \tag{4.29}$$

$$\boldsymbol{K}^H \boldsymbol{v}_p = \sigma_p \boldsymbol{e}_p \tag{4.30}$$

Where $(.)^H$ is the Hermitian transpose operator, $\boldsymbol{e}_p$ is the p^{th} right singular vector, $\boldsymbol{v}_p$ is the p^{th} left singular vector corresponding to singular value , σ_p. Equation (4.29) shows us that if an excitation vector $\boldsymbol{e}_p$ is applied to the transmitter array, the output of the receiver array will be $\sigma_p \boldsymbol{v}_p$. On the other hand the second equation shows that if the received signals $\boldsymbol{v}_p$ are back propagated from the receiver array in other words time reversed and sent by the receiver array, the signals at the transmitter would be $\sigma_p \boldsymbol{e}_p$. The matrix $\boldsymbol{K}^H$ is the time reversed version of the matrix $\boldsymbol{K}$.

Combining equations (4.29) and (4.30) we get the normal equations of the singular system

$$\boldsymbol{K}\boldsymbol{K}^{H}\boldsymbol{v}_{p} = \boldsymbol{\sigma}_{p}^{2}\boldsymbol{v}_{p} \tag{4.31}$$

$$\boldsymbol{K}^{H}\boldsymbol{K}\boldsymbol{e}_{p} = \boldsymbol{\sigma}_{p}^{2}\boldsymbol{e}_{p} \tag{4.32}$$

When we write equations (4.31) and (4.32) in explicit form

$$\sum_{k=1}^{M} \kappa_{m}\boldsymbol{g}_{R}(\boldsymbol{Q}_{m})\boldsymbol{g}_{T}(\boldsymbol{Q}_{m})^{T}\boldsymbol{e}_{p} = \boldsymbol{\sigma}_{p}\boldsymbol{v}_{p} \tag{4.33}$$

$$\sum_{k=1}^{M} \kappa_{m}^{*}\boldsymbol{g}_{T}^{*}(\boldsymbol{Q}_{m})\boldsymbol{g}_{R}^{H}(\boldsymbol{Q}_{m})\boldsymbol{v}_{p} = \boldsymbol{\sigma}_{p}\boldsymbol{e}_{p} \tag{4.34}$$

and than further expansion shows that $\boldsymbol{v}_{p}$ are linear combinations of receiver array steering vectors, $\boldsymbol{g}_{R}(\boldsymbol{Q}_{m})$ and $\boldsymbol{e}_{p}$ are linear combinations of transmitter steering vectors $\boldsymbol{g}_{T}(\boldsymbol{Q}_{m})$'s for $\boldsymbol{\sigma}_{p} > \boldsymbol{0}$. Therefore finding $\boldsymbol{g}_{R}(\boldsymbol{Q}_{m})$ and will provide us a solution for the position of m^{th} target.

Singular value decomposition of the multistatic matrix $\boldsymbol{K}$ results in N_T transmitter singular vectors, $\{\boldsymbol{e}_{1}, \boldsymbol{e}_{2}, ..., \boldsymbol{e}_{N_T}\}$ that span the space C^{T}, N_R receiver singular vectors $\{\boldsymbol{v}_{1}, \boldsymbol{v}_{2}, ..., \boldsymbol{v}_{N_R}\}$ that span the space C^{R} and $min(N_T, N_R)$ singular values $\{\sigma_{1} \geq \sigma_{2} \geq ... \geq \sigma_{M+1} = \sigma_{M+2}...\sigma_{min(N_T,N_R)} = 0\}$. Since there are M targets, $\{\boldsymbol{e}_{1}, \boldsymbol{e}_{2}, ..., \boldsymbol{e}_{M}\}$ are called signal singular vectors corresponding to singular values $\{\sigma_{1}, \sigma_{2}, ..., \sigma_{M}\}$ and span signal subspace of C^{T}. The remaining singular vectors $\{\boldsymbol{e}_{M+1}, \boldsymbol{e}_{2}, ..., \boldsymbol{e}_{N_T}\}$ are called noise singular vectors corresponding to singular values $\sigma_{M+1} = \sigma_{M+2}...\sigma_{min(N_T,N_R)} = 0$, and span the noise subspace of C^{T}. These two subspaces are orthogonal to each other. We define a matrix $\boldsymbol{N}_{E}$ that holds these noise singular vectors of the transmitter space in its columns. Similar relationship holds for the matrix $\boldsymbol{V}$ that contains singular vectors $\boldsymbol{v}_{j}$ in its columns. $\boldsymbol{N}_{V}$ is also defined as the matrix holding the noise singular vectors of the receiver subspace in its columns.

Next step is meshing the computational domain and calculating the receiver and the transmitter array steering vectors, $\boldsymbol{g}_{R}(\boldsymbol{R}')$ and $\boldsymbol{g}_{T}(\boldsymbol{R}')$ for every discrete point $\boldsymbol{R}'$ in the domain. The squared Euclidean distance of a receiver array steering vector corresponding to a target at $\boldsymbol{R}'$ to the receiver signal subspace is given by

$$\boldsymbol{d}_{R}^{2} = \boldsymbol{g}_{R}^{H}(\boldsymbol{R}')\boldsymbol{N}_{V}\boldsymbol{N}_{V}^{H}\boldsymbol{g}_{R}(\boldsymbol{R}') \tag{4.35}$$

The MUSIC spectrum is obtained by scanning possible values of $\boldsymbol{R}'$ in two dimensions.

$$\boldsymbol{P}_{\boldsymbol{R}}(R') = \frac{1}{\boldsymbol{g}_{\boldsymbol{R}}^{\boldsymbol{H}}(\boldsymbol{R}')\boldsymbol{N}_{\boldsymbol{V}}\boldsymbol{N}_{\boldsymbol{V}}^{\boldsymbol{H}}\boldsymbol{g}_{\boldsymbol{R}}(\boldsymbol{R}')} \tag{4.36}$$

Similarly the MUSIC spectrum regarding the transmitter array is

$$\boldsymbol{P}_{\boldsymbol{T}}(R') = \frac{1}{\boldsymbol{g}_{\boldsymbol{T}}^{\boldsymbol{H}}(\boldsymbol{R}')\boldsymbol{N}_{\boldsymbol{E}}\boldsymbol{N}_{\boldsymbol{E}}^{\boldsymbol{H}}\boldsymbol{g}_{\boldsymbol{T}}(\boldsymbol{R}')} \tag{4.37}$$

Both spectrums will have peaks whenever $\boldsymbol{R}' = \boldsymbol{Q}_{\boldsymbol{m}}$. These two spectrums can be combined in several ways such as

$$\boldsymbol{P}_{\boldsymbol{MU}}(R') = \boldsymbol{P}_{\boldsymbol{T}}(R') + \boldsymbol{P}_{\boldsymbol{R}}(R') \tag{4.38}$$

$$\boldsymbol{P}_{\boldsymbol{MU}}(R') = \boldsymbol{P}_{\boldsymbol{T}}(R') \times \boldsymbol{P}_{\boldsymbol{R}}(R') \tag{4.39}$$

or

$$\boldsymbol{P}_{\boldsymbol{MU}}(R') = \frac{1}{1/\boldsymbol{P}_{\boldsymbol{T}}(R') + 1/\boldsymbol{P}_{\boldsymbol{R}}(R')} \tag{4.40}$$

In fact only a single TRM spectrum $\boldsymbol{P}_{\boldsymbol{T}}$ or $\boldsymbol{P}_{\boldsymbol{R}}$ is sufficient to find the locations of the targets. However this only succeeds in ideal conditions. In practice rather than peaks at the locations of the targets, in a single TRM spectrum there will be linear regions with higher intensity representing the directions of the targets such as the white ones in Fig. 4.10. So combination of the two TRM spectra is often needed to find the locations of the targets. In Fig. 4.10, both receiver and transmitter spectra are sketched on the same computational domain. There are three targets in the environment. The spectrum regarding the receiver aray are the three rays diverging from the first receiver antenna. Similarly the spectrum regarding the transmitter array is represented by the three lines diverging from the first transmitter antena. The intensity of both spectrums are higher at the vicinity of the targets denoted by red and blue regions on the rays. When these two spectra are combined using (4.38)-(4.40) or any other appropriate way, there will occur six peaks due to the crossings of these two sets of rays. Three of them being more significant than the remaining correspond to the locations of the targets, since the high intensity regions of both spectra are coincident at target locations. These regions are circled with yellow. The remaining three lower peaks are also circled with red dashed lines. Remember that this kind of information is obtained at a single frequency using the multistatic data.

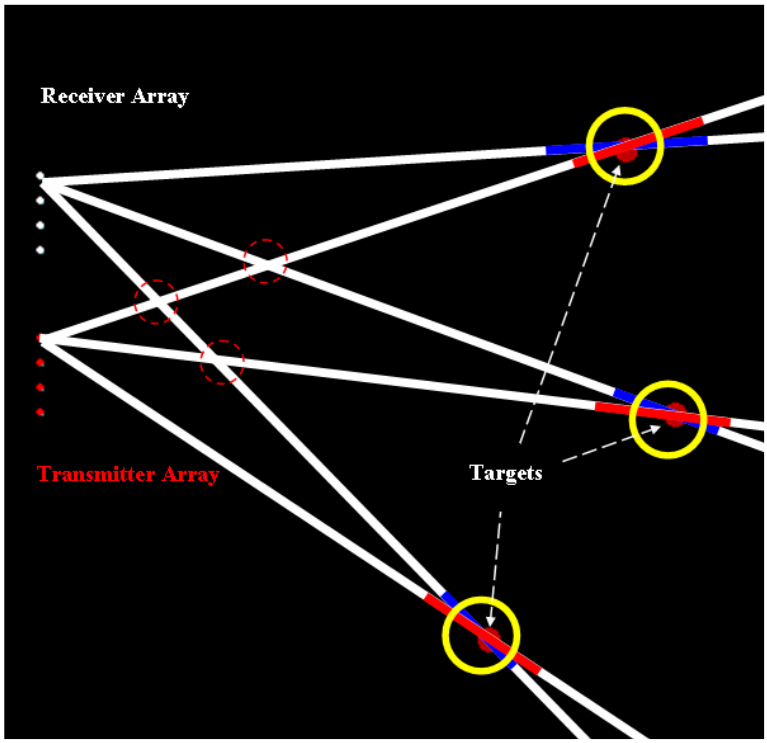

Fig. 4.10 Illustration of a typical TRM processing result

A more perpendicular crossing of the two sets of white lines would be obtained if the receiver array and the transmitter array were arranged as shown in Fig. 4.11. However this may not be practical in some applications where the radar has to be compact.

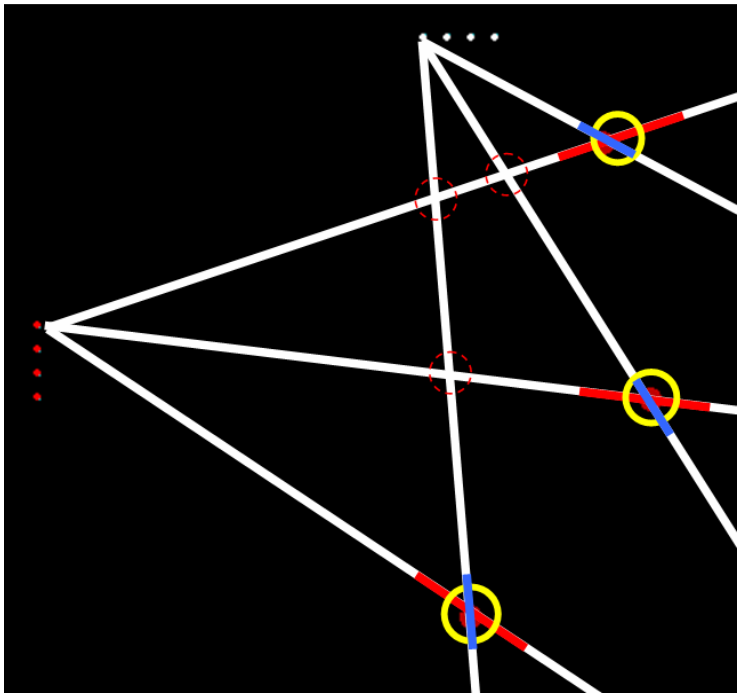

Fig. 4.11 A different arrangement of receiver and transmitter arrays providing a more perpendicular crossing of the lines of the two spectra

4.3.2 Simulation Results

The following figure, Fig. 4.12 shows the TRM applied to a FDTD simulation data at 330 MHz. There are ten point-transmitters outlined with red spots and ten point-receivers outlined with white spots. Inter-element distance for both arrays is 75cm. The actual locations of seven targets are represented with black circles.

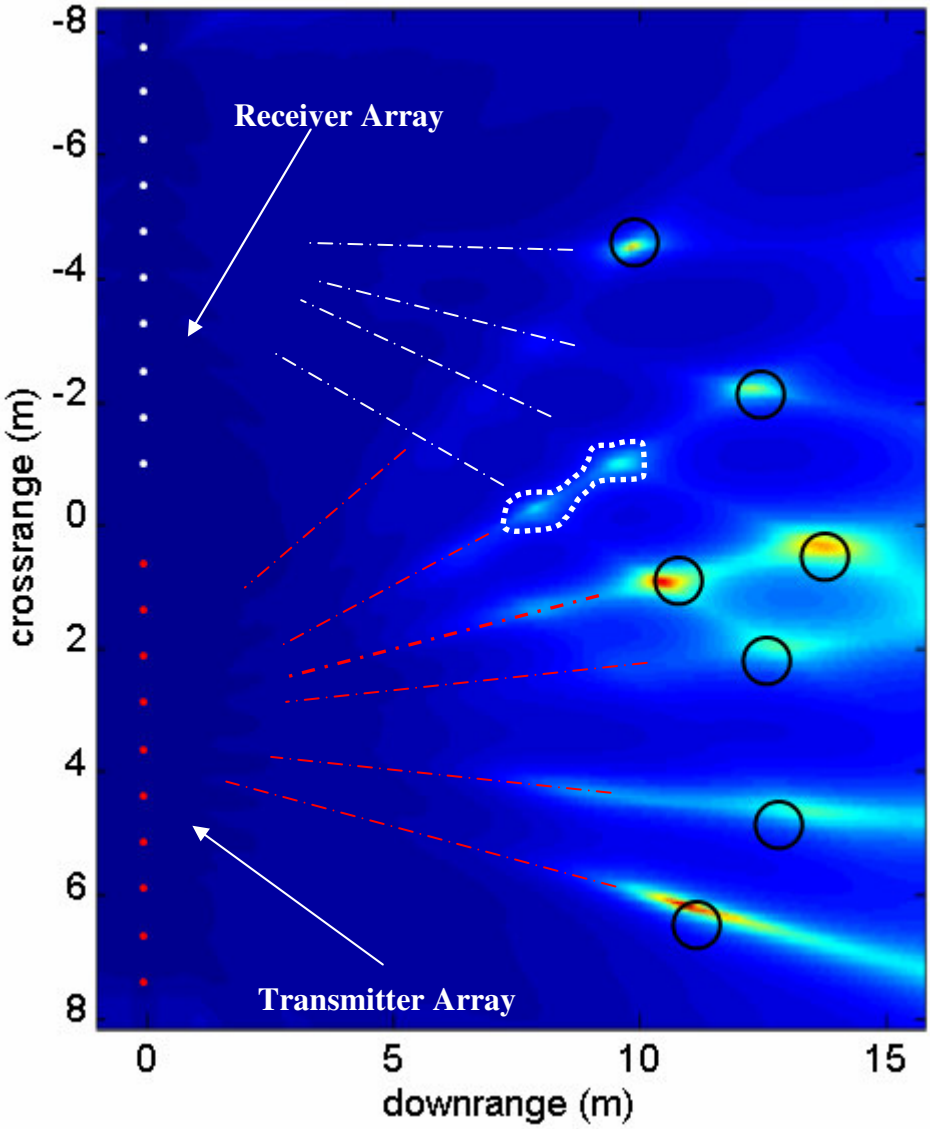

Fig. 4.12 Result of TRM algorithm at 330 MHz for seven point targets and ten element transmitter and receiver array

When Fig. 4.12 is examined carefully it is realized that the locations of the targets are found by the crossings of the rays diverging from the transmitter array and the rays diverging from the receiver array. Some of these are depicted with dashed

lines. Also there are some local peaks at locations different than the locations of the targets. Two of these are enclosed with a dashed contour.

When the processing is performed at frequencies from 25 MHz to 600 MHz in 25 MHz steps, 24 similar maps are obtained. Multiplication of these maps gives a better result for the locations of the targets as shown in Fig. 4.13. Small ambiguities that exist in Fig.4.12 are disappeared and also target locations became more apparent.

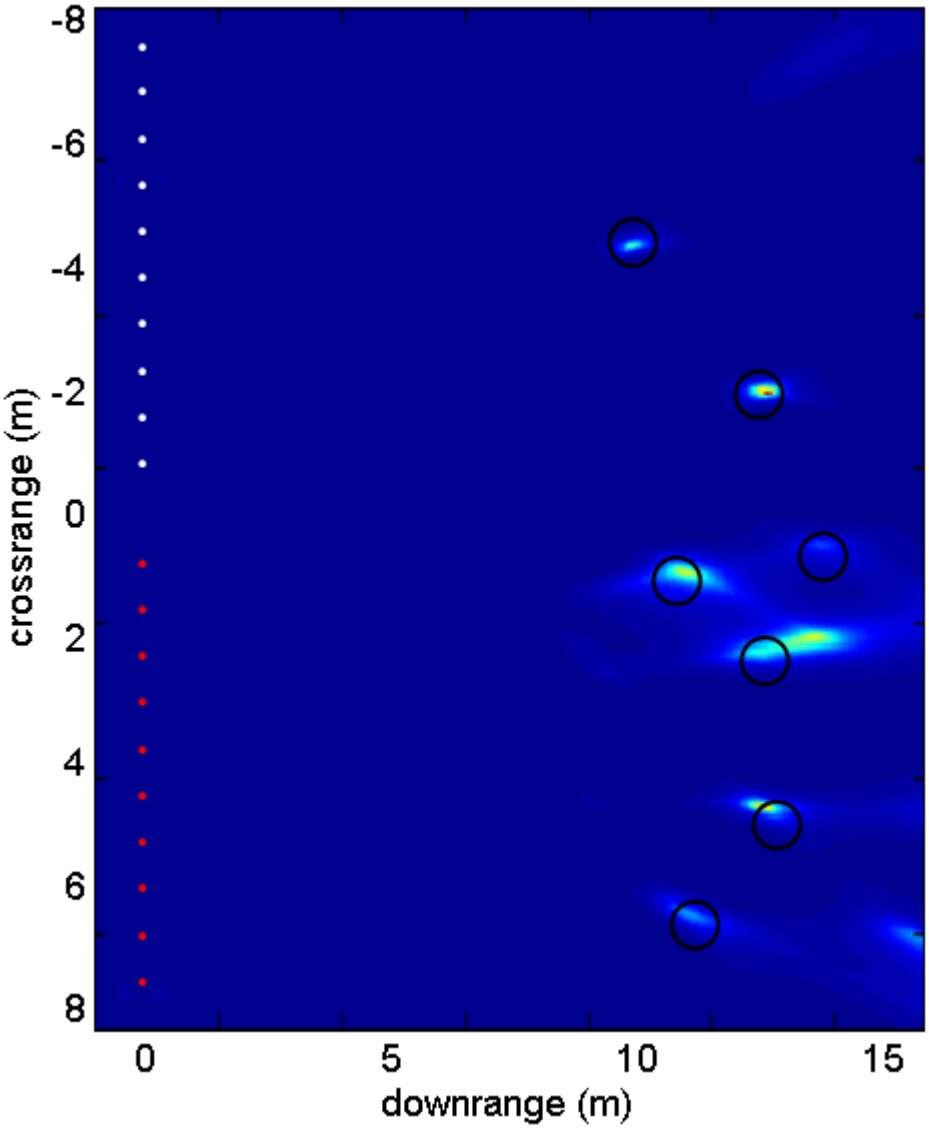

Fig. 4.13 Product of the results of TRM algorithm from 25 MHz to 600 MHz in 25 MHz steps.

There are various theoretical and experimental results on Time Reversal MUSIC algorithm in acoustics [47]-[49]. Also there are a few on electromagnetics [25], [50].

4.3.3 Ambiguities at High Frequencies

Suppose that receivers are arranged in a uniform linear array (ULA) and there is only one target which is far away from the receivers so that the impinging signal on the array can be considered as a plane wave. The consecutive phase difference between the antennas will be

$$\Delta\phi = \frac{2\pi.d_r}{\lambda}\sin(\theta) \tag{4.41}$$

Here θ is the angle between the direction of the target and the normal of antenna axis as shown in Fig. 4.2 and therefore satisfies

$$-\frac{\pi}{2} \le \theta \le \frac{\pi}{2} \tag{4.42}$$

Since a unique θ exists for each $\Delta\phi$, determining $\Delta\phi$ is sufficient for finding the direction of the target, θ.

From the two equations (4.35) and (4.36) we can write

$$-\frac{2\pi.d_r}{\lambda} \le \Delta\phi \le \frac{2\pi.d_r}{\lambda} \tag{4.43}$$

One important point is that the detected phase difference between the antennas arrays will always be in the $[-\pi, \pi]$ range because of the property of Fourier transform. We will shortly see that this property is the reason for having ambiguities.

The detected phase difference in other words phase differences of the result of the Fourier transforms will be denoted as.

$\Delta\hat{\phi} = \Delta\phi \pm 2m\pi$ where m is an integer so that $-\pi \le \Delta\hat{\phi} \le \pi$ is satisfied.

We want to find the number of θ^m s that satisfy both

$$\frac{2\pi.d_r}{\lambda}\sin\left(\theta^m\right) = \Delta\hat{\phi} \tag{4.44}$$

and

$$-\frac{\pi}{2} \le \theta^m \le \frac{\pi}{2} \tag{4.45}$$

From the first equation we can write

$$\theta_m = \sin^{-1}\left(\frac{\lambda.\Delta\hat{\phi}}{2\pi.d_r}\right) = \sin^{-1}\left(\frac{\lambda.\left(\Delta\phi \pm 2m\pi\right)}{2\pi.d_r}\right) \tag{4.46}$$

Combining with the second equation we get

$$-\frac{\pi}{2} \le \sin^{-1}\left(\frac{\lambda.(\Delta\phi \pm 2m\pi)}{2\pi.d_r}\right) \le \frac{\pi}{2} \tag{4.47}$$

or equivalently

$$-1 \le \frac{\lambda.(\Delta\phi \pm 2m\pi)}{2\pi.d_r} \le 1 \tag{4.48}$$

Simplifying further we obtain

$$-\frac{\Delta\phi}{2\pi} - \frac{d_r}{\lambda} \le m \le -\frac{\Delta\phi}{2\pi} + \frac{d_r}{\lambda} \tag{4.49}$$

Using equation (4.35) to replace $\Delta\phi$ we get

$$-\frac{d_r}{\lambda}(1+\sin(\theta)) \le m \le \frac{d_r}{\lambda}(1-\sin(\theta)) \tag{4.50}$$

The number of solutions for θ is the values of m that satisfy equation (4.42) and it is dependent on the actual angle of the target , θ.

From this result we can deduce that in order to ensure that there are no ambiguities

$$d_r < \frac{\lambda}{2} \tag{4.51}$$

or

$$f < \frac{c}{2d_r} \tag{4.52}$$

should be satisfied, where c is the phase velocity of the wave. Therefore as the processing frequency increases the number of ambiguities will also increase.

In deriving the number of ambiguities we assumed that the impinging signal is a plane wave and there is no noise in the environment. These results are also valid when the sources of the impinging waves are far from the array so that the incident waves are close to plane waves. Also notice that this analysis is valid for uniform linear arrays of receivers. For the case of multiple targets the ambiguities are the superposition of ambiguities arising from each individual target. The actual angle of the target, θ always exists as a solution independent of the processing frequency, however the remaining solutions for θ change depending on the processing frequency. As an example, consider Fig. 4.14 where there are two targets denoted by yellow circles and receiver and transmitter antenna arrays each having four elements. The TRM processing result

at 450MHz is shown at the left and the result of processing for 500 MHz is at the right. Here only the spectrum regarding the receiver array spectrum, given by (4.36) is used. While the peaks corresponding to actual target locations remain constant, the other solutions which are ambiguities shift as processing frequency changes. More ambiguities occur at 500 MHz since number of ambiguities increase with frequency.

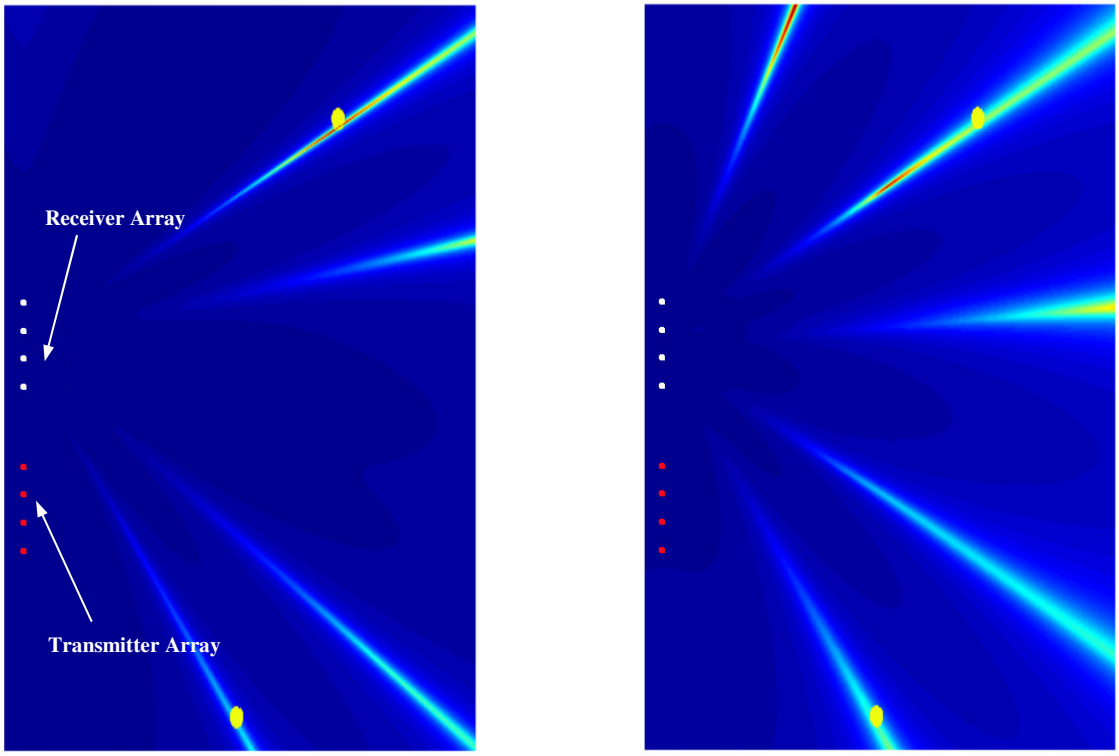

(a) **(b)**

Fig. 4.14 **(a)** The TRM spectrum regarding the receiver array at 450 MHz. **(b)** The spectrum at 500 Mhz

Combining the results of multiple frequencies these ambiguities can be eliminated. We will later show by simulation that by random orientation of the antennas the number of these ambiguities can also be reduced. This type of ambiguities that occur as a result of phase wrapping of Fourier transform will be mentioned as "Type 1 ambiguities."

4.3.3.1 Effect of Antenna Orientation

For a uniform linear antenna array the phase difference between consecutive antennas is same when a plane wave impinges. Adding a phase of 2π to the detected signals of each antenna becomes a valid solution as well. If we make no antenna pairs equivalent to each other so that plane wave impinging from no direction results the same amount of phase difference between any pair the number of ambiguities are is expected to decrease.

Fig. 4.15 (a) shows an antenna arrangement in which there are equivalent pairs however there are no equivalent pairs in the arrangement of Fig. 4.15 (b). Notice that in ULA arrangement there are many equivalent pairs.

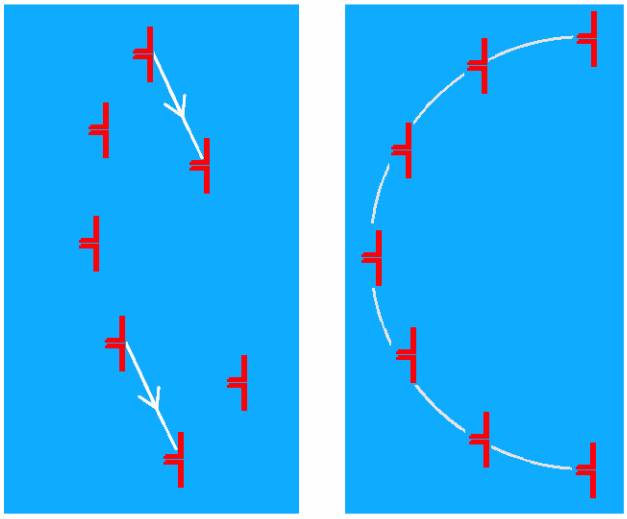

(a) **(b)**

Fig. 4.15 Different arrangements of multiple antennas. **(a)** An arrangement having equivalent pairs. **(b)** An arrangement having no equivalent pairs

In order to compare the performances of ULA and circular antenna orientations a Finite Difference Time Domain simulation has been performed. For a ULA of four receiver and four transmitter antennas ambiguities start to occur when $f_c > 2c_0/d_r$. For this case f_c =250 MHz. The processing results at 900 MHz are presented in Fig. 4.16 (a) for the ULA and 4.16 (b) for circular array. The yellow spots are the targets. It is seen that antenna orientation has a significant effect on the detection performance.

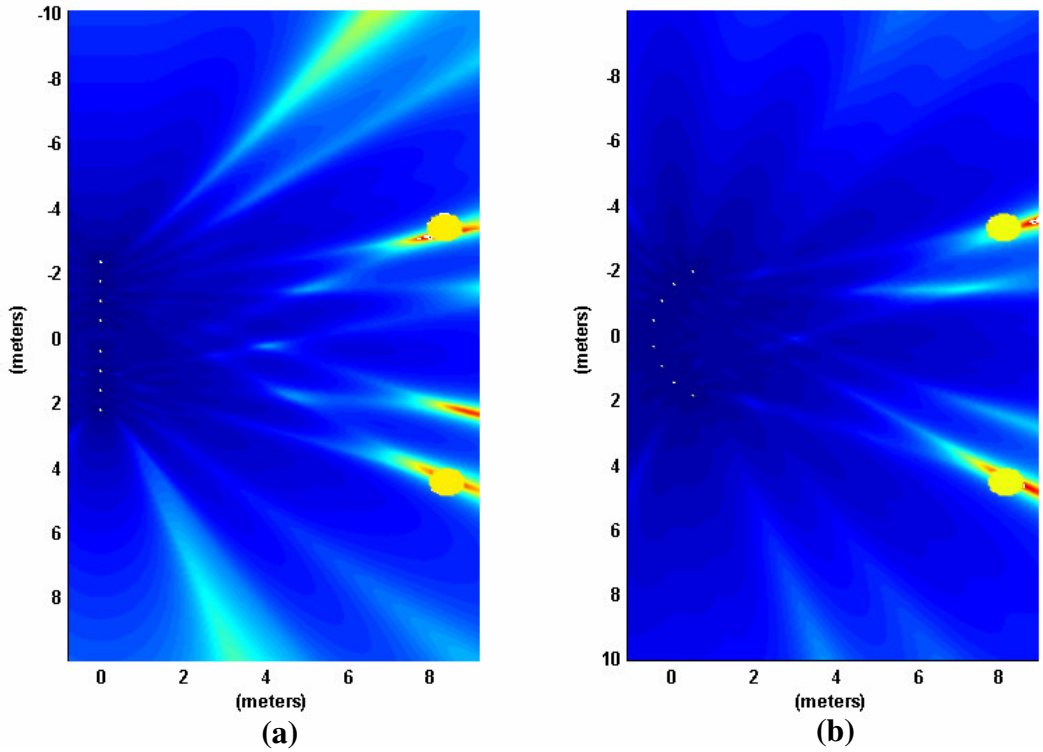

Fig. 4.16 The processing results at 900 MHz . **(a)** for the ULA and **(b)** for the circular array.

CHAPTER 5

EXPERIMENTS

5.1 Experimental Setup

The radar system can be considered in three main blocks: the transmitter block, the receiver block, and the signal processing block. The photo of the radar prototype can be seen in Fig. 5.1. Also the block diagram of the system can be seen in Fig. 5.2. Some of the parameters of the system are summarized in Table 5.1. The elements in each block will be explained in detail in the following sections.

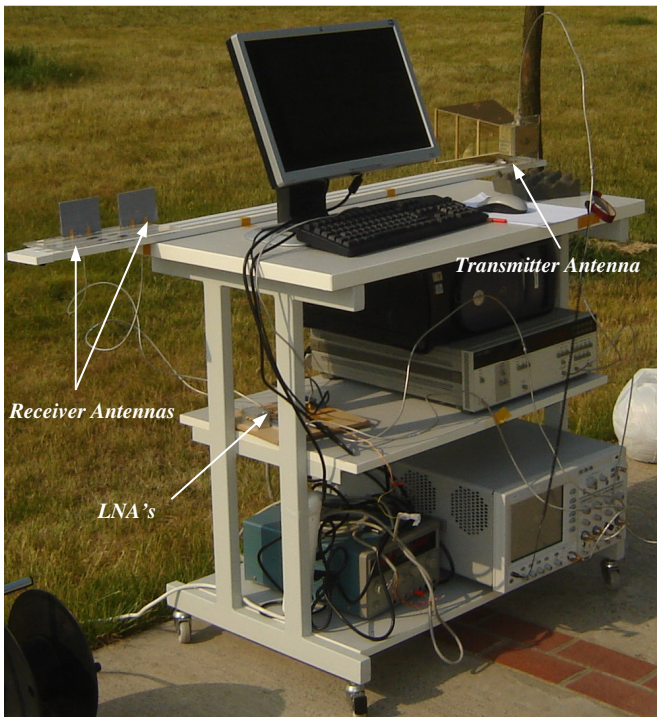

Fig. 5.1 The photograph of the UWB radar prototype used in the experiments

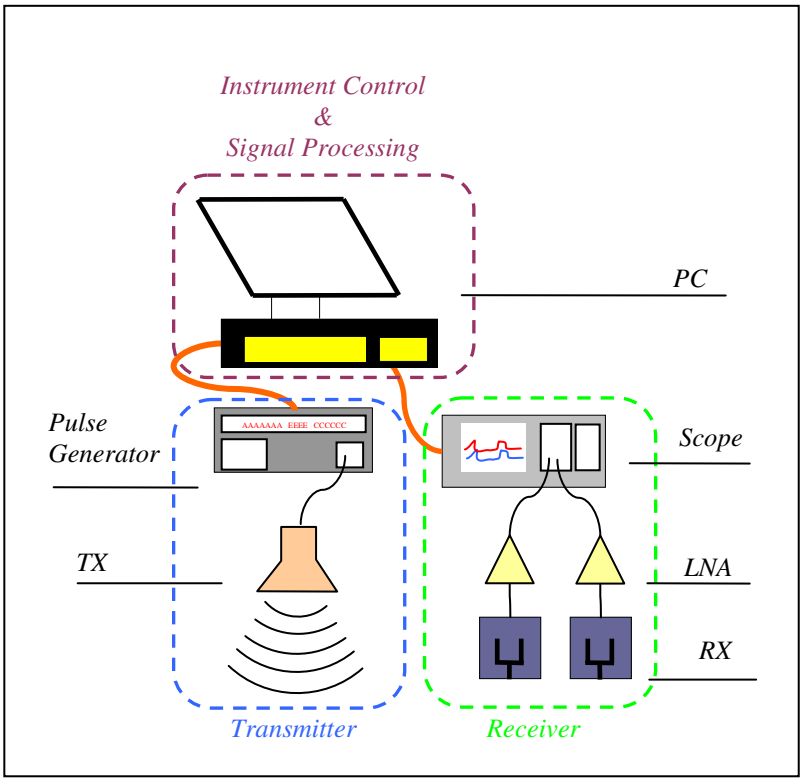

Fig. 5.2 The block diagram of the UWB radar prototype

RADAR PARAMETERS	
Frequency range	1.85-6.3 GHz
Maximum Radiated Power	110 mW
Pulse Repetition Frequency	33 MHz
Unambiguous Range	4.5 m

Table 5.1 Some of the important parameters of the radar prototype

5.1.1 The Transmitter Block

This block has two elements, the pulse generator and the transmitter antenna. The pulse generator is a commercially available Agilent 8133A which is used to generate impulses having full width half maximum (FWHM) duration of 150 picoseconds and a period of 33MHz. The peak amplitude of the impulses is 3.3 Volts. The transmitter horn antenna is directly fed with the transmitted signals. Frequency characteristic of the transmitter horn antenna is given in Table 5.2.

The antenna has an almost flat response between 1.5GHz and 5GHz. The average gain of the antenna in this frequency range is approximately 9.2dBi and the antenna can radiate 10 Watts of power to the free space.

Frequency (MHz)	Antenna Factor (dB/m)	Gain (dBi)	Gain (Numeric)
700	25,8	1,31	1,35
800	22,4	5,94	3,93
900	22,6	6,75	4,73
1000	23,1	7,1	5,13
1250	23,6	8,57	7,19
1500	24,1	9,68	9,28
1750	25,4	9,74	9,42
2000	28,7	7,57	5,71
2500	28,8	9,37	8,65
3000	30,2	9,58	9,08
3500	31,2	9,94	9,86
4000	33,6	8,71	7,43
4500	33,9	9,44	8,79
5000	35,2	9,05	8,03
5500	35	10,1	10,22
6000	35,7	10,12	10,28

Table 5.2 Transmission characteristics of the transmitter horn antenna

5.1.2 The Receiver Block

The receiver antennas are home built microstrip slot antennas on a FR4 board. [51]. In the receiver part there are two UWB microstrip antennas separated with a distance of 15cm from each other. The received signals are amplified by 26db with a low noise UWB amplifier connected to both receiver antennas. Finally the amplified signals are digitized by a 20GHz bandwidth sampling scope, Agilent 81600C.

5.1.3 Instrument Control and Signal Processing Block

The operation of the pulse generator and digital scope is controlled by a Personal Computer (PC). The data sampled by scope is collected by the PC and processed in

MATLAB. Both the control of the equipment and the signal processing is performed in Matlab.

The two basic processing algorithms are Time reversal MUSIC (TRM), Delay Estimation MUSIC (DEM). The TRM algorithm uses only a single frequency component and all of received waveforms whereas DEM algorithm uses a single waveform but uses multiple frequency information. We improve the capability of TRM method by combining the outputs for multiple frequencies.

5.2 Multistatic Data Acquisition

In our system we have one transmitter antenna and a receiver array of two antennas. However experimentally we need transmitter and receiver arrays both having four antennas. In order to emulate this we had to change the position of the transmitter and receiver antennas and take snapshots for different antenna positions. In one data acquisition cycle we position the transmitter antenna to one of its positions and change the receiver antenna position twice by taking snapshots each time. Then we reposition the transmitter antenna to its remaining three positions repeating the same steps. The acquisition method is illustrated in Fig. 5.3. By this way at the end of one data acquisition cycle sixteen waveforms are gathered. The waveforms of the previous cycle are then subtracted from the new data so that echoes coming from the stationary targets are eliminated. Because the echoes coming from moving targets have shifted in the second cycle, they can not cancel each other so at those regions a nonzero signal appears. The next step is extracting the direction and distances of the targets using these sixteen waveforms.

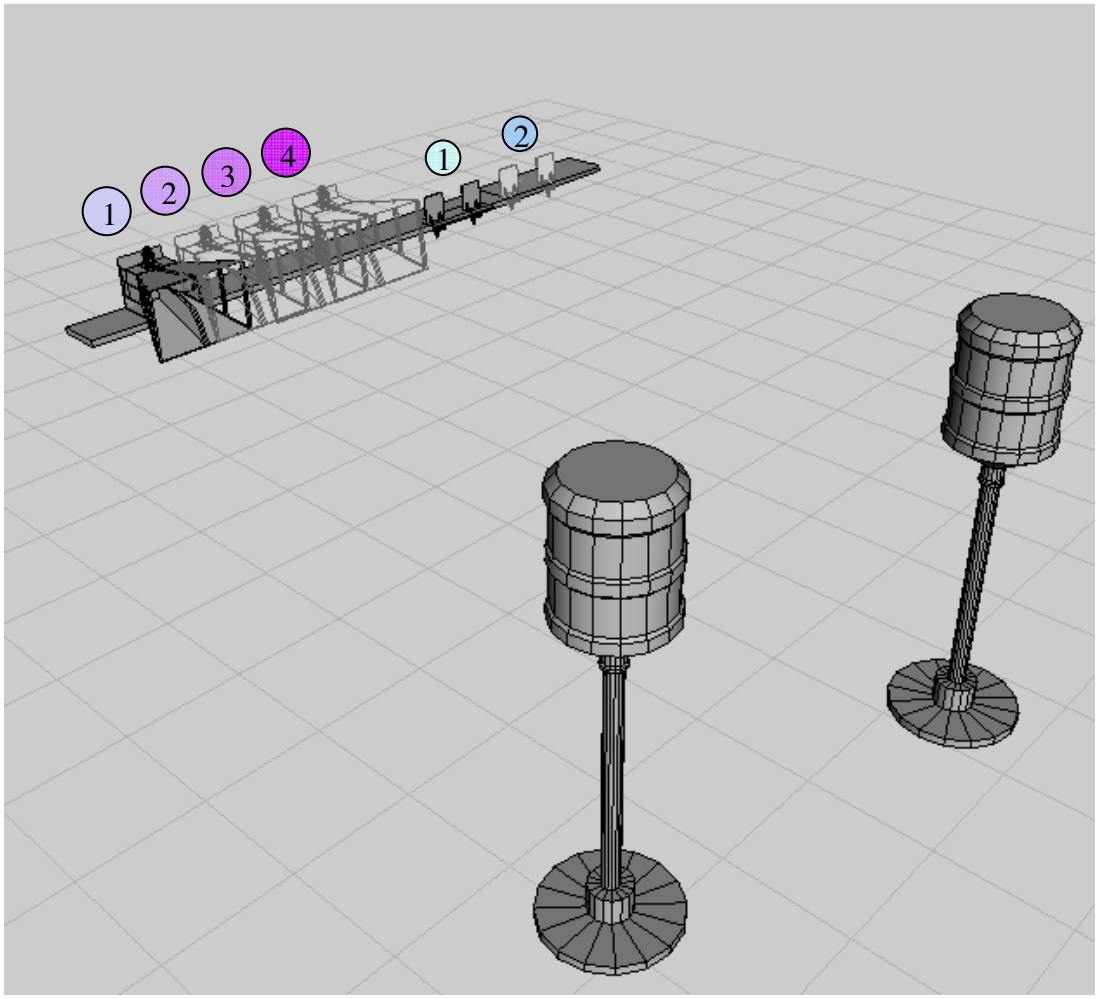

Fig. 5.3 The illustration showing four transmitter antenna positions, two receiver array positions and the targets

5.3 Application of Signal Processing Algorithms

5.3.1 Application of Time Reversal MUSIC

There are two unknown parameters for each echo: the direction of arrival (DOA) and the time of arrival (TOA). In ideal conditions the Time Reversal MUSIC algorithm gives accurate results for the locations of multiple targets as shown in Fig. 4.13. Unfortunately this is not the case when TRM algorithm is applied to data we collected by our prototype. Major reason for this is that there are multiple reflections in the components of the receiver block, which causes undesired phase shift in the received

signals. TRM algorithm is successful in detecting the directions of targets however it is sensitive to phase errors when detecting the ranges of the targets. To clarify this consider Fig. 5.4 which shows the results of TRM processing performed on the experimental data which was acquired when there were two targets in the environment. Fig. 5.4 (a) is the spectrum related with the receiver array (equation (4.36)) and Fig. 5.4 (b) is the spectrum related with the transmitter array (equation (4.37)). In both graphs the resultant maps obtained at frequencies ranging from 850 MHz to 3.5 GHz in 50 MHz steps are summed up. Looking at these figures it is not possible to say the exact location of the target, however directions of the targets are apparent.

By multiplying the spectrum of Fig. 5.4 (a) with the spectrum of Fig. 5.4 (b), we obtain the combined spectrum shown in Fig. 5.4 (c). Although we can vaguely see the intersection points of the two spectra, the exact target locations are still not clear. This is due to two reasons. One of them is that the DOA lines are not fine enough as a result of unideal effects such as noise or multiple reflections inside the system as mentioned earlier, are included in the experimental data. The second and the dominant reason is that the transmitter and the receiver arrays are located close and the DOA lines originating from both arrays cannot intersect each other at steep angles like in the configuration shown in Fig. 4.11.

For the experimental data, TRM spectra either for the receiver array (equation (4.36)) or for the transmitter array (equation (4.37)) results in good estimates for the directions of the targets. However combining these two spectra is not sufficient for finding the locations of the targets. We will refer to the regions with higher intensity (colored red) in the TRM spectra as “DOA lines”.

Remember that Time Reversal Music (TRM) algorithm uses all of the sixteen waveforms acquired at the data acquisition step and gives the resultant map at the desired frequency. In order to improve (i.e. to eliminate Type I ambiguities) the DOA estimation, the processing results at multiple frequencies are combined as explained in section 4.3.3.

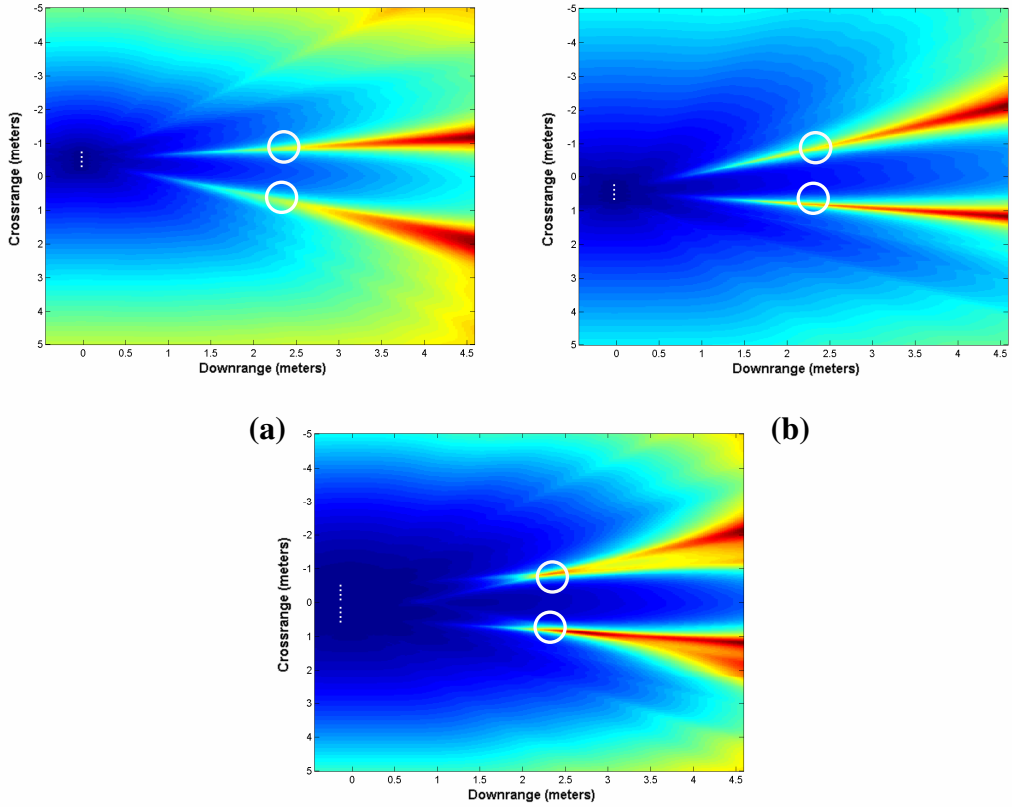

Fig. 5.4 (a) TRM spectrum for the receiver array. **(b)** TRM spectrum for the receiver array. **(c)** Combination of the two spectra.

5.3.2 Application of Delay Estimation MUSIC

A given TOA of an echo provides an ellipse as the possible locations of the target. The two foci of this ellipse are the coordinates of the receiver and the transmitter antennas, ($\boldsymbol{R}_i$,$\boldsymbol{T}_j$) that are used to obtain the waveform. In the special case when the transmitter and the receiver are collocated the possible locations of the target become a circle with center being the transceiver. In this section we will explain the application of DEM algorithm on the multistatic data. To better visualize the situation, consider Fig. 5.5 (a) showing an environment where there is a ULA of four point transmitter antennas, a ULA of four point receiver antennas and two targets. FDTD simulation to obtain the multistatic response of the environment is performed. A narrow pulse is transmitted from the transmitter antennas one at a time and the received waveforms are

recorded. Therefore, there are a total of sixteen received waveforms each containing two echoes from the two targets. One of the waveforms and its DEM spectrum can be seen in Fig 5.5 (b). For each of the sixteen waveforms first DEM is applied and sixteen spatial DEM spectra are obtained. Logarithms of the DEM spectra are used so that low peaks of weaker echoes become more apparent. Finally these sixteen spatial spectra are summed up to obtain the final spatial spectrum. Based on this procedure two simulations for two different transmitter and receiver antenna spacing are performed and the results are shown in Fig 5.6

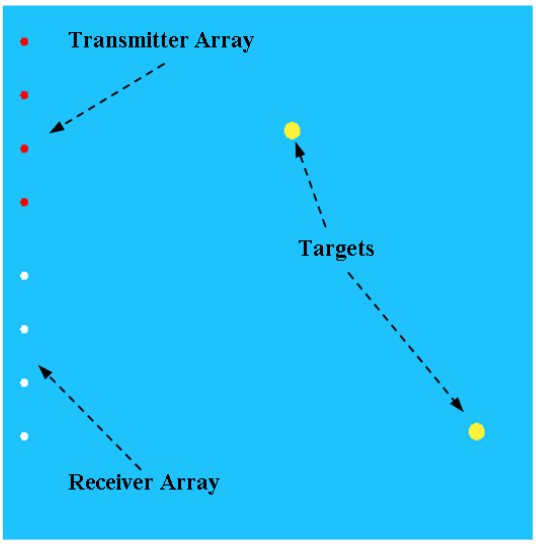

(a)

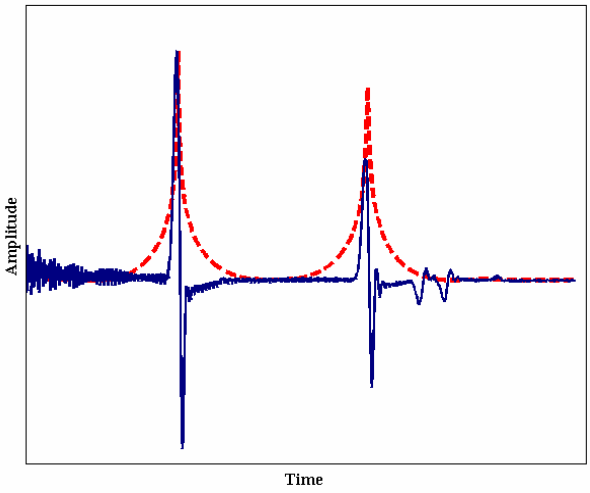

(b)

Fig. 5.5 (a) The arrangement of transmitter antennas, the receiver antennas and the targets used in the FDTD simulation **(b)** A sample experimental received waveform and its DEM spectrum

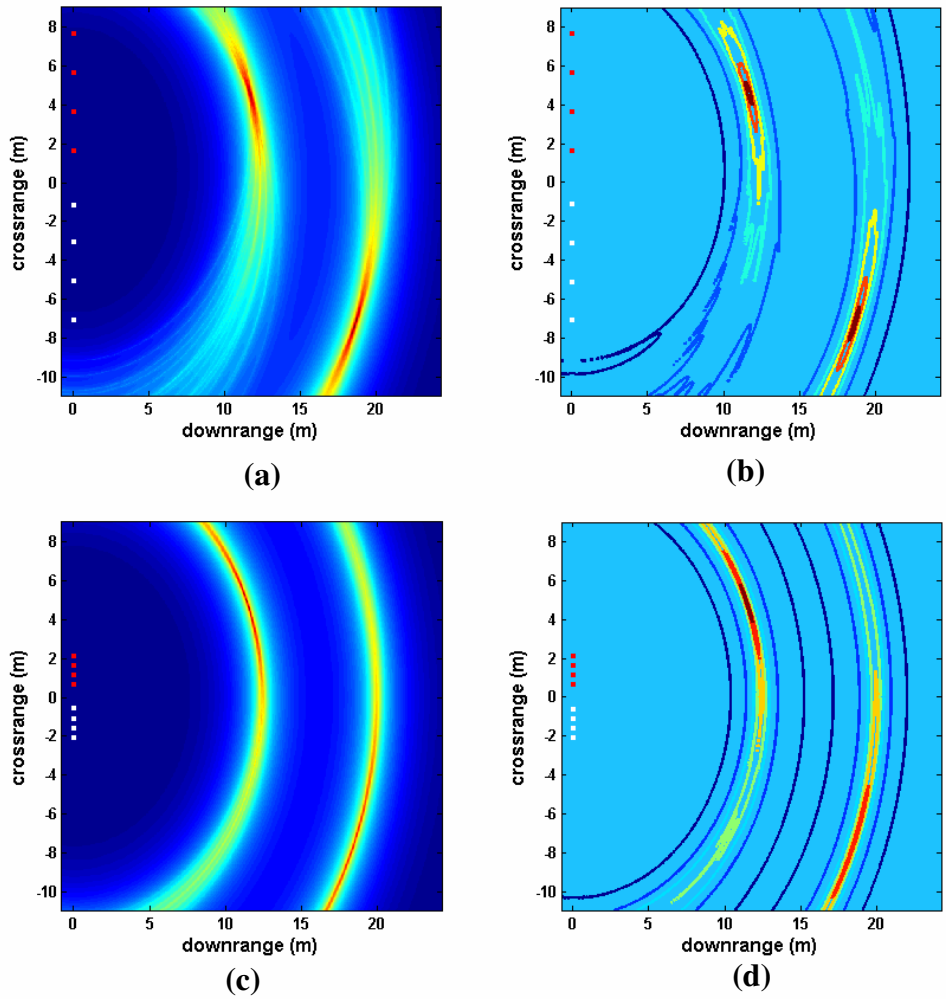

Fig. 5.6 Results of the performed simulations. **(a)** The inter-element spacing of both transmitter and receiver arrays is 2 meters. **(b)** The contour plot of the spectrum in **(a)**. **(c)** The inter-element spacing of both transmitter and receiver arrays is 50 cm. **(d)** The contour plot of the spectrum in **(c)**

The elliptic bands can be recognized in the spectrum of Fig. 5.6 (a). The regions where the elliptic bands associated with the same target echo intersect have a higher intensity and therefore represent the estimated target locations. In this spectrum the estimated target locations are the red regions. Looking at the figure it is easy to tell the approximate distance of each target with respect to the origin; however the directions of the targets are not clearly identified since the red regions are spread in azimuthal direction. This detection capability declines when the inter-element spacing of transmitter and receiver arrays is reduced. In this case ellipses associated with the same

target intersect at even more moderate angles resulting in a higher azimuthal spread. A better visualization of the situation is presented in Fig. 5.7.

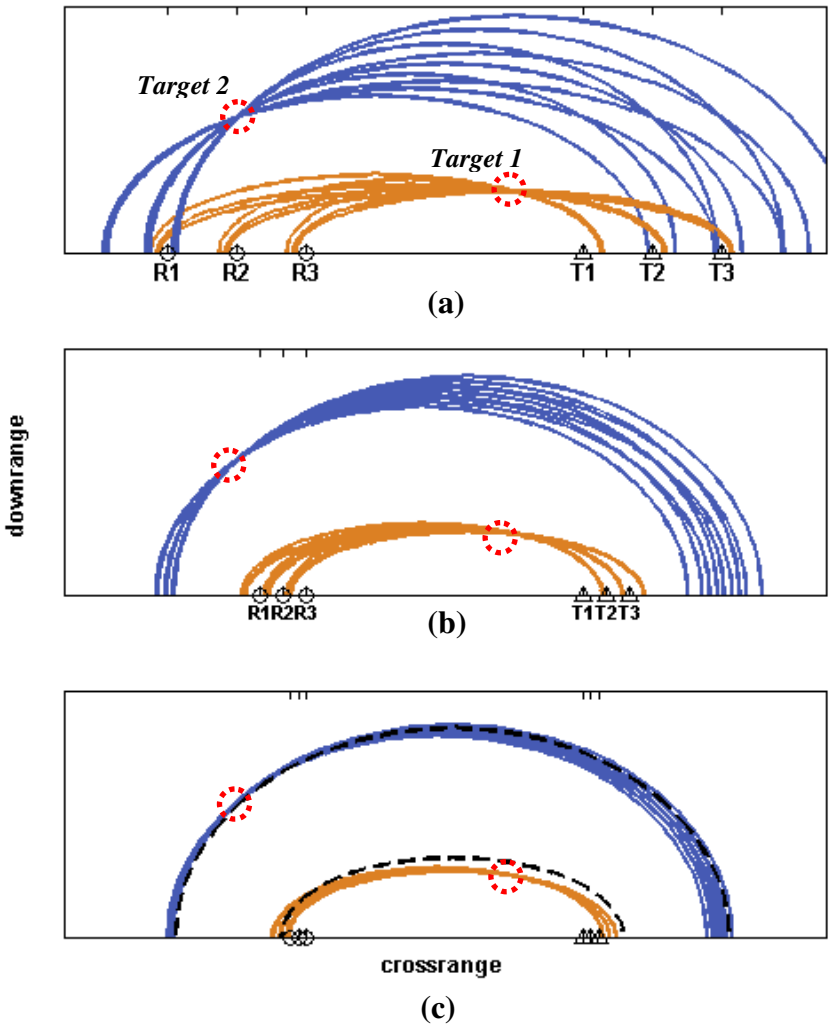

Fig. 5.7 (a) The visualization of target localization procedure using only the TOA information. **(b)** Inter-element spacing between the antennas is reduced **(c)** Inter-element spacing between the antennas is further reduced

In this example, there are two targets in the environment and the locations of the three receiver and the three transmitter antennas are indicated with circles and triangles respectively. Nine ellipses colored brown are associated with "target 1" and nine blue ones are associated with "target 2". The inter-element spacing between the antennas of the receiver array and the transmitter array decreases gradually from Fig 5.7 (a) to Fig 5.7 (c). While antennas become closer within each array the detection of the direction

of the target becomes harder. When the spacing of the antennas are small compared to the distances of the targets, the ellipses associated with each target becomes almost confocal. In such a case the ellipses associated with a target can be fitted into a single ellipse. The fitted ellipse associated with each target is shown in black, dashed lines. The foci of both are chosen as the center of the receiver array and the center of the transmitter array. This figure shows the ideal case.

Now consider that the echoes coming from both targets overlap in time. The DEM spectrum that will be obtained in such a case is illustrated in Fig. 5.8. The ellipses associated with both targets are overlapped. Therefore there are multiple intersection points between the ellipses related with the two targets and it is not possible to distinguish the ellipses belonging to “Target 1” from the ellipses belonging to “Target 2”. This situation makes the detection harder. In Fig 5.8 (c) where the antenna spacing of both transmitter and receiver array is small, all of these eighteen the ellipses can be fitted into one single ellipse shown with the black dashed line. Notice that this time the dashed line is drawn thicker in order to express that the fitted ellipse is spread in radial direction.

In experimental data the azimuthal spread is even more since there are elliptic bands instead of ellipses; therefore the spatial spectra obtained by the DEM can be used for estimating the distances of the targets but not for their directions. Since in our experiments we have sixteen waveforms acquired by different transmitter and receiver antenna pairs, we have sixteen ellipses associated with each target. In our experiments the spacing between elements of both arrays are very small compared to the distances of targets, therefore the condition in Fig. 5.7 (c) and Fig. 5.8 (c) holds. We have chosen to sum up all sixteen temporal DEM spectra and then map the resultant spectra to spatial coordinates assuming that the foci are the center of gravities of transmitter and receiver arrays. We will see the experimental examples in the subsequent sections.

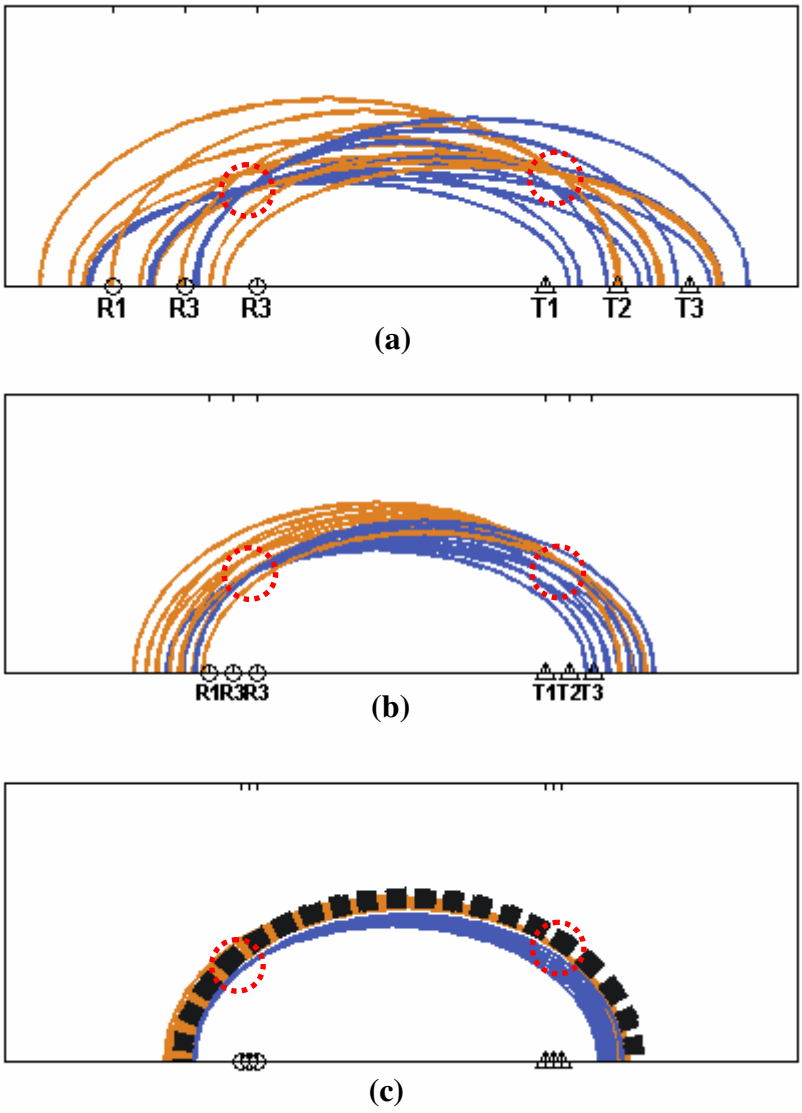

Fig. 5.8 (a) The same concept explained in Fig. 5.7 but this time **t**he echoes from two targets have almost the same times of arrivals. **(b)** Inter-element spacing between the antennas is reduced **(c)** Inter-element spacing between the antennas is further reduced

5.3.3 Combining TRM and DEM Spectra

In the preceding sections we have resulted that TRM is good at finding the direction and DEM algorithm performs well in finding the distance of the targets. The DOA lines of the TRM spectrum and the TOA ellipse of the DEM spectrum intersect almost perpendicularly which is something beneficial. In combining these two spectra ambiguous cases occur. In this section we will also provide a simple solution to resolve these ambiguities if the target echoes are separated enough in time.

As described earlier the spatial DEM spectra of the experimentally acquired data resembles Fig. 5.7 (c) or Fig. 5.8 (c), in which targets' distances are large compared to inter-element spacing of the arrays' elements. In Fig. 5.9 it is seen that position of a single target can be identified using the cross section of the ellipse obtained by the TOA information and the line found by the DOA information. The actual ellipses of spatial DEM spectrum are shown with light brown lines. These are fitted to a single ellipse shown with dashed black line. There is a mismatch between the actual target location and the detected target location due to this fitting.

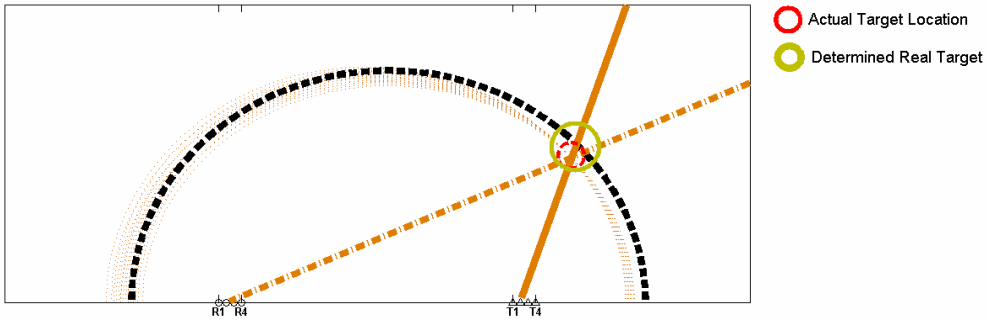

Fig. 5.9 The situation when there is a single target in the environment, four closely spaced receiver antennas and four closely spaced transmitter antennas

When there are multiple targets in the environment multiple DOAs and multiple TOAs are expected to be found. When a TRM spectrum having two DOA lines and a spatial DEM spectrum having two distant ellipses are combined, the result will be similar to the one illustrated in Fig. 5.10.

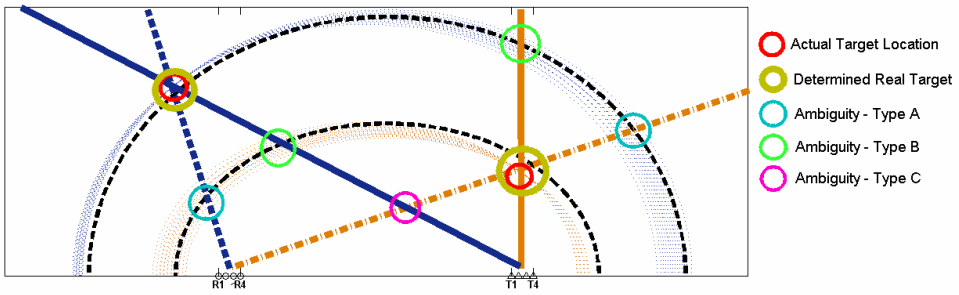

Fig. 5.10 The illustration of combining TRM and DEM spectra when there are two targets in the environment

In this figure, besides detected actual targets, there are ambiguities resulting from intersections of lines and ellipses. If only a single TRM spectrum, either the one regarding the receiver array (dashed DOA lines) or the one regarding the transmitter array (solid DOA lines) there will be no occurrence of "Type C" ambiguities. Besides one of the "Type A" or "Type B" ambiguities will remain.

The intensity of "Type C" ambiguity is related to how the TRM and DEM spectra are combined. If they are multiplied the intensity of "Type C" ambiguities will be negligible compared to "real targets", "Type A" or "Type B" ambiguities.

$$P^{2D} = P_{TRM}^{2D} \times P_{DEM}^{2D} \tag{5.1}$$

If they are added, still the intensity of "Type C" ambiguities is expected to be low, but may not be negligible.

$$P^{2D} = P_{TRM}^{2D} + P_{DEM}^{2D} \tag{5.2}$$

We will see processing results for experimental data soon. Before that one last case to consider is again in the two target case , when the echoes coming from both targets are overlapped in time. As we have shown in Fig. 5.11, the sets of ellipses (brown and blue) corresponding to each of the targets can not be distinguished and will be fitted into one single ellipse. In this case the detection error will be greater than the previous cases but not as much as error caused by "Type A", "Type B" and "Type C" ambiguous cases depicted in Fig. 5.10.

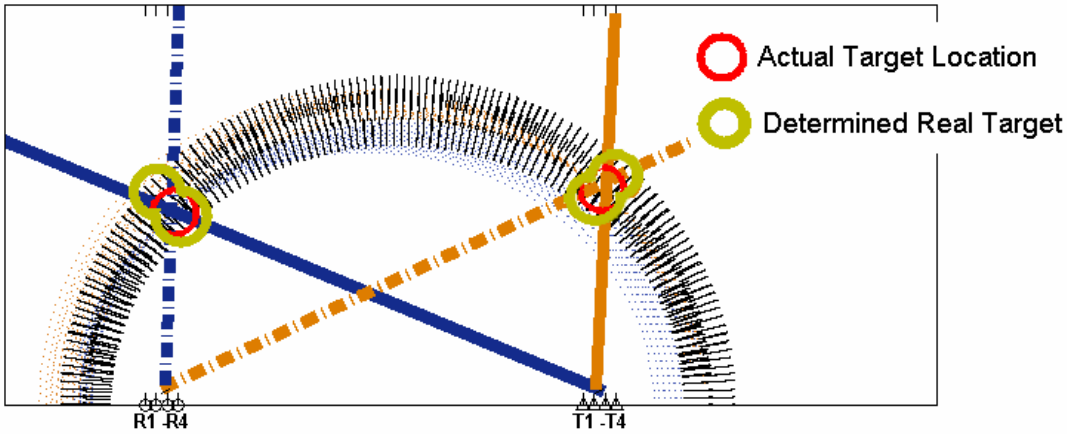

Fig. 5.11 A single ellipse obtained by fitting the ellipses obtained by DEM spectra

5.3.3.1 Segmentation

The ambiguities referred to as “Type A”, “Type B” or “Type C” in Fig. 5.10 will be called in general “Type 2 ambiguities”. As number of targets increases these ambiguities will also increase since there will be more DOA lines and TOA ellipses; however can be resolved, if the echoes of the targets are separated enough in each of the acquired waveforms. Consider again the case when there are two targets in the environment and four receiver and four transmitter antennas are used. In this case all of the sixteen waveforms will be divided from the same time instant so that each segment contains only one echo. This case is illustrated in Fig. 5.12.

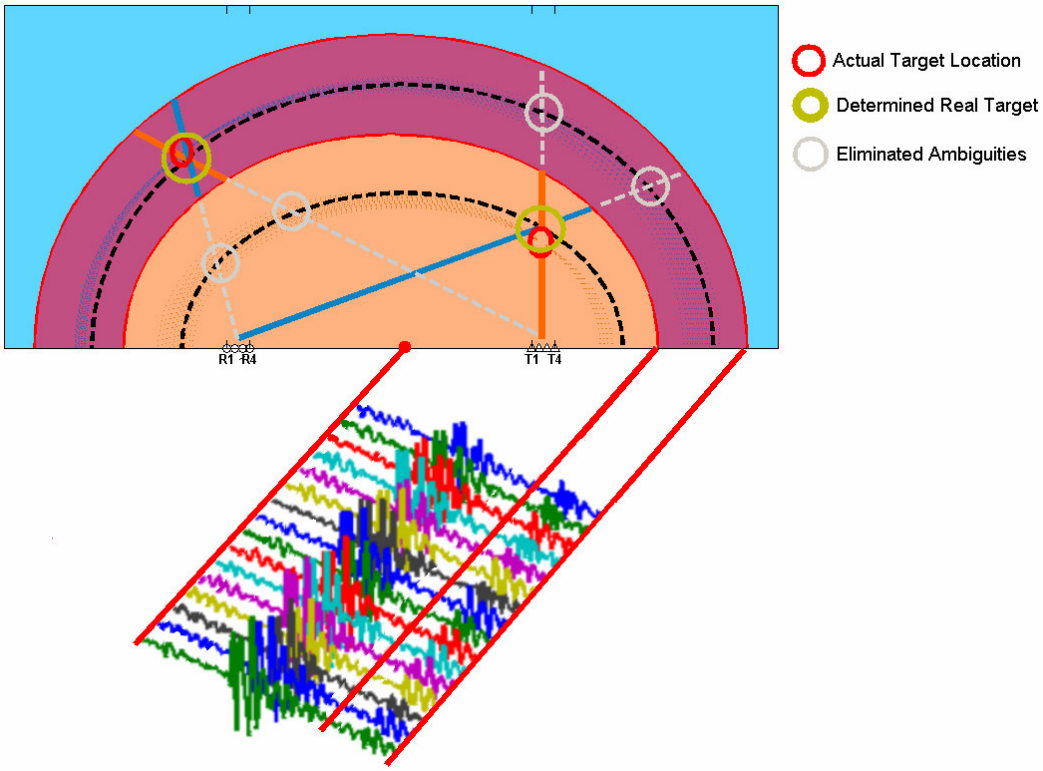

Fig. 5.12 Illustration of the processing result when segmentation is applied

The waveforms shown can be segmented into two from the time moment represented by the red line. Each segment is associated with a region in space limited by ellipses. These regions are colored with light orange and purple. The boundary of these regions is determined by the time instant the waveforms are separated at. The remaining light blue region is outside the unambiguous range (section 2.1.2). Each of these waveform segments are processed separately and the results are spliced at the end. Since the resultant DOA lines found for each segment are valid only in their corresponding region, ambiguities are eliminated. In the case when there are more than two targets, some of the echoes may be separated while others can not. The waveforms should be segmented into as many parts as possible in order to reduce the number of ambiguous targets.

Besides reducing ambiguities, segmentation also increases the performance of detection algorithms. Both TRM and DEM algorithms perform better when there are less number of targets to be identified which implies a higher dimensional noise subspace and a lower dimensional signal subspace. Distinction between noise and signal subspaces become more perspicuous and the shadowing effect of stronger targets

on the weaker ones can be avoided. Notice that segmentation procedure comes with a cost of increased processing which is a crucial issue in real time applications.

5.3.4 Processing Steps

The first step is subtracting the acquired data of the previous step from the current one to eliminate stationary signals which are either the echoes from stable targets or the antenna couplings. Because the echoes coming from moving targets have shifted in the second cycle, they can not cancel each other so at those regions a nonzero signal appears. We will refer to the waveforms obtained this way as "difference waveforms." Consider Fig. 5.13 where examples of the resultant difference waveforms for different amount of shifts in the received echo are presented. In Fig. 5.13 (a) the target is moving slowly while in (b) the target is fast. How will the signal processing algorithms TRM and DEM respond in both cases?

In fact it turns out that there is no problem for the TRM algorithm as long as the moving targets' direction does not change too much. In [48] it is proven theoretically and by simulation that Time Reversal MUSIC algorithm performs well even if there is a significant amount of second order scattering, that is the reflected waves from a target also impinges on another target and causes a secondary wave radiated by that target. Assuming that the targets' directions do not change significantly, subtracting two waveforms has a similar effect. The targets' echoes in the subtracted waveform can be thought as a second order scattered wave from the target.

On the other hand our empirical studies show that if the target moves fast the resultant difference waveform causes shifts in the original DEM spectrum. However these are not abrupt so can be tolerated up to some extent. For the experiment we have perfomed this error is negligible.

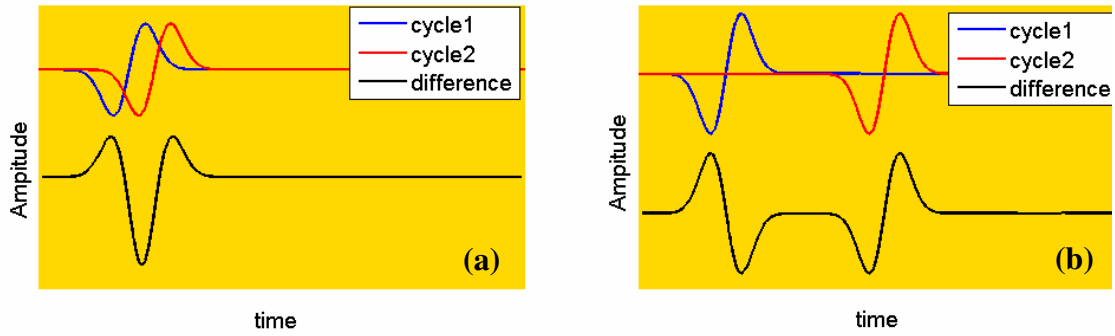

Fig. 5.13 The shape of difference signals. **(a)** When the target is slow **(b)** When the target is fast

An advantage of UWB mentioned in section 2.2 was mentioned as the ability to detect slowly moving targets. As the pulse with gets narrower the difference between the pulse and a slightly shifted version of itself will be higher in amplitude. This is illustrated in Fig. 5.14. There are two UWB pulses in the blue waveform having equal power but one of the having wider bandwidth therefore narrower in time. Red waveform is the shifted version of the blue one. The difference of the red and the blue waveforms is the black waveform. As it is seen the difference of the narrower pulses results in both a higher amplitude and higher power. So the pulses getting narrower in time, enables the detection of targets moving with a smaller velocity.

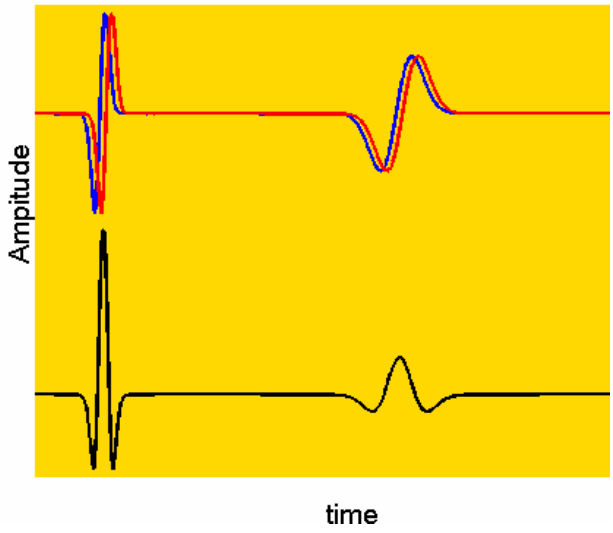

Fig. 5.14 Comparison of the difference echoes having different bandwidths

Fig 5.15 (a) shows the sixteen waveforms acquired by different receiver and transmitter pairs using our radar system while there were two moving targets in the environment. Fig. 5.15 (b) shows the waveforms resulted by taking the difference of successive snapshots. The antenna coupling effects are completely canceled and since the targets have changed position in the second cycle a signal appeared in the vicinity of the positions of the their echoes in time.

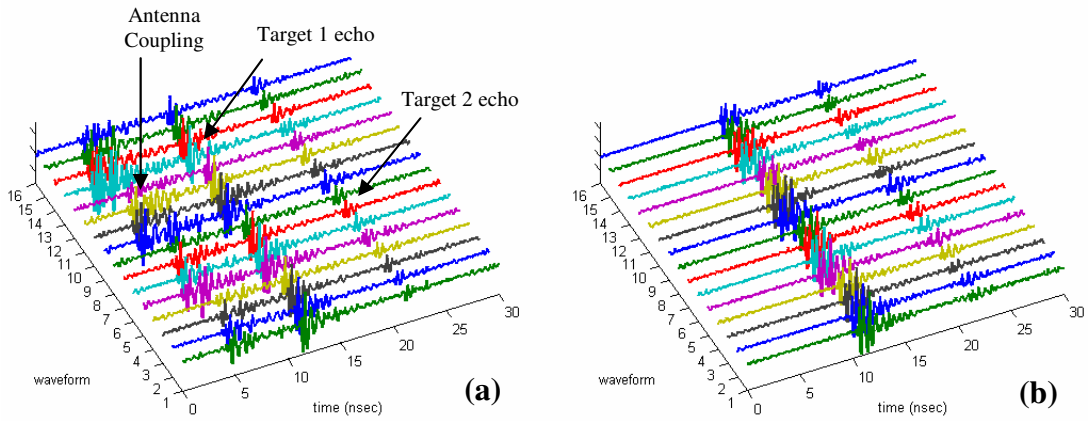

Fig. 5.15 a) Sixteen received waveforms for the first target position **b)** Difference waveforms resulted by subtracting the waveforms acquired for the second target positions from the waveforms acquired for the first target position

TRM algorithm finds the locations of targets by utilizing the phase differences of echoes between antennas. Since we are interested in UWB signals, when we compare the waveforms received by different antennas for the same position of the target, we would like to see that only the position of the echoes have shifted preserving their shape. Using difference signals may not satisfy this property as we saw that the shape of the difference signal is dependent on the velocity of the target. Fig. 5.16 shows two sample difference signals. To clarify, there are multiple receiver and transmitter antennas. We acquired data for some position of the target and after moving the targets slightly we acquired a second snapshot. The red waveform is the result of subtraction of the waveform acquired in the first cycle using the first transmitter and the first receiver, (T_1, R_1) from the one acquired in the second cycle using the same antenna pair. Similarly the black one is the difference of waveforms obtained by first transmitter and the second receiver (T_1, R_2).

The echoes coming from both targets are circled with dashed lines. Within a waveform, the shapes of the two "difference echoes" may be different since targets may have different velocities. Also comparing red and black waveforms, the echoes related with the same target are not equivalent since the amount phase shift of a target's echo varies for different antenna pairs when the target moves and therefore taking the difference may result in different signal shapes.

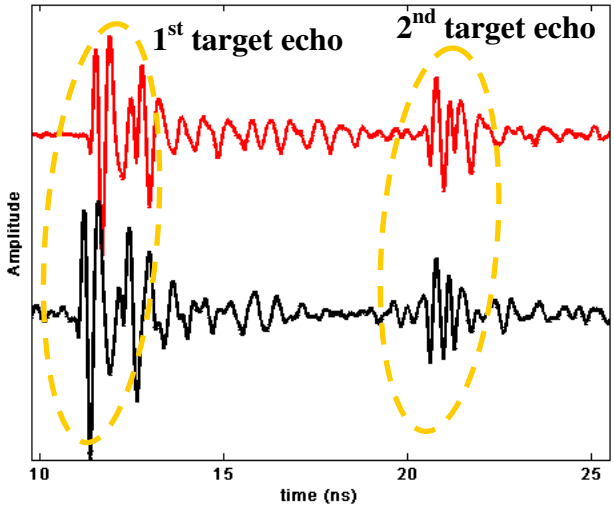

Fig. 5.16 Comparison of two difference waveforms of different antenna pairs

However as we have mentioned these effect do not degrade the performance of TRM algorithm and their effect on DEM algorithm is negligible. There are multiple reflections in the receiver block of the system which degrades the performance of both algorithms. After finding the difference between waveforms acquired in consecutive cycles, as the second step the temporal delay spectra of the resultant sixteen waveforms are obtained using the DEM algorithm and they are averaged to obtain a single profile. The averaged profile will be used to determine if there are well separated target echoes. Fig. 5.17 (a) and (b) shows two cases for experimentally obtained difference waveforms and the average of their delay profiles. In the case of Fig. 5.17 (a) looking at the averaged delay profile we can conclude that the waveforms can be segmented since it has two distinct peaks. On the other hand the averaged delay profile in Fig 5.17 (b) has only one peak although the waveforms include echoes from two targets. In this case the waveforms can not be segmented.

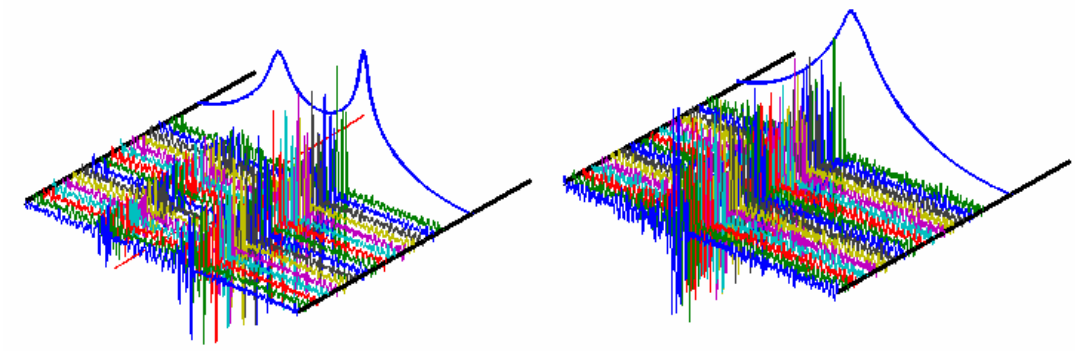

(a) **(b)**

Fig. 5.17 a) The averaged DEM spectrum when the two target echoes are seperate **(b)** The averaged DEM spectrum when the two target echoes are overlapped

If it is possible to segment the waveforms a secondary DEM is applied the waveforms in each segment and the resultant profiles are averaged again. Fig. 5.18 shows the resultant spatial DEM spectra with and without segmenting. In the first plot the black temporal DEM profile is the averaged delay profiles of the sixteen waveforms, the red one is the averaged delay profile of the left hand side segment and the blue one is for the right hand side segment. The secondary DEM profile composed of red and blue parts has sharper peaks. Since the amplitudes of the peaks in the DEM spectrum is directly related with the amplitudes of the corresponding echoes, in the primary spectrum which is colored black, the peak associated with the weaker group of echoes is lower in amplitude. As done in the secondary profile, processing each segment separately, normalizing the resultant spectra and splicing them provide the echoes to be equally treated.

Segmentation improves the performance of finding the directions of the targets as well. To prove this TRM algorithm is performed on an experimental data at frequencies ranging from 850MHz to 3.5GHz in 50MHz steps. The resultant receiver array spectra are averaged and similarly the resultant transmitter array spectra are averaged up. Finally these two averaged spectra are multiplied. This process is done with and without segmentation an the results are plotted in Fig. 5.19. The dashed circles represent the target positions. Looking at the plot at the right hand side which is the result without segmentation the TRM algorithm fails to find the directions of the targets while in the left hand side plot the directions of the targets can be observed.

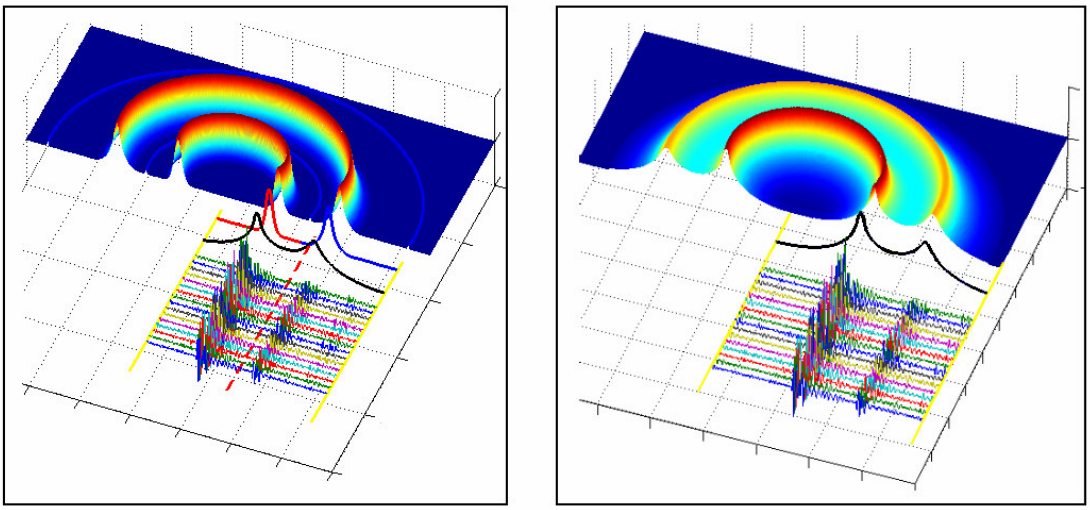

(a) **(b)**

Fig. 5.18 (a) Mapping of averaged DEM spectrum obtained by segmenting **(b)** Mapping of averaged DEM spectrum obtained without segmenting

The final job is to combine these two maps obtained by DEM and TRM methods and locate the targets. We preferred to multiply these two maps; however they can be combined in various other ways. Fig 5.20 shows the result with segmentation (at left) and without segmentation (at right).

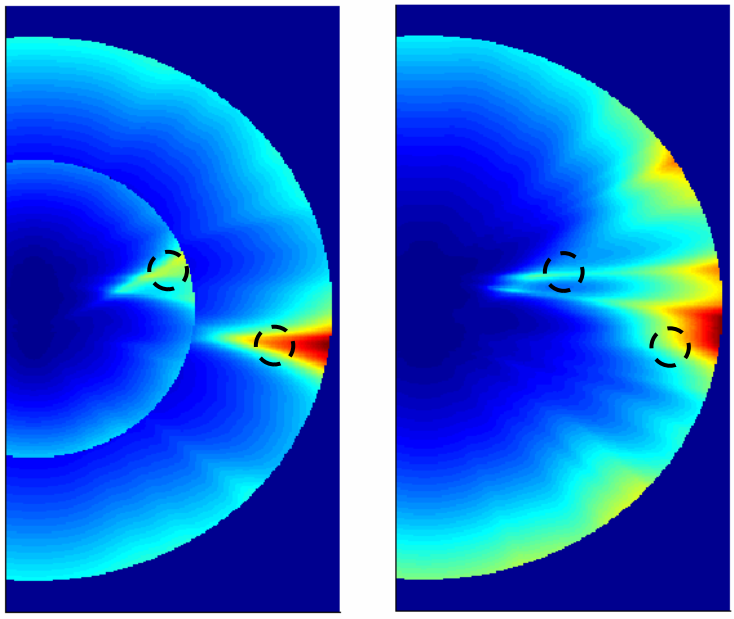

(a) **(b)**

Fig. 5.19 (a) The TRM spectrum obtained by averaging spectra at different frequencies with segmentation **(b)** The TRM spectrum obtained by averaging spectra at different frequencies without segmentation

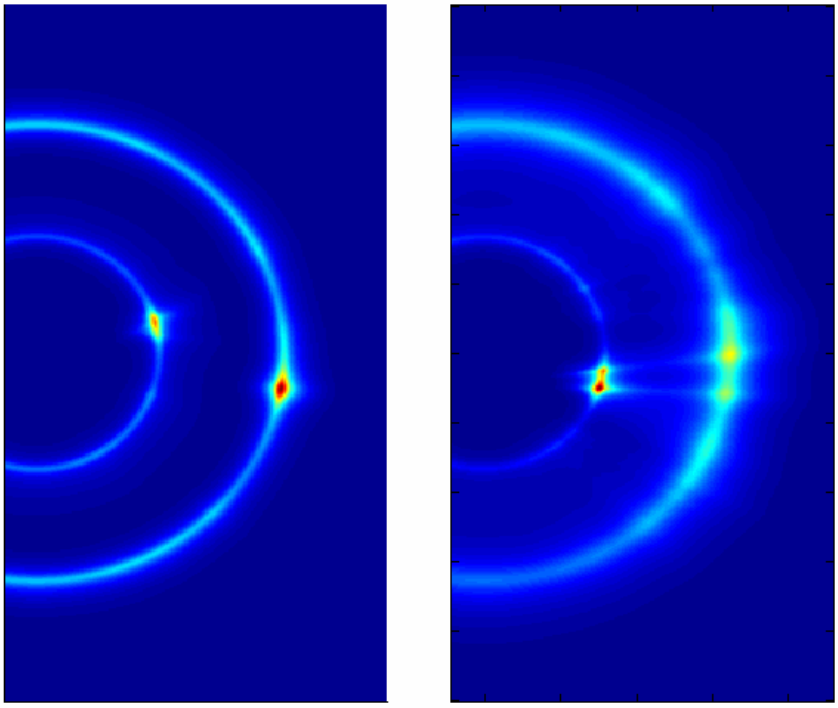

(a) **(b)**

Fig. 5.20 **(a)** Final result with segmentation **(b)**) Final result with out segmentation

An overview of the proposed processing scheme can be seen in the schematic below.

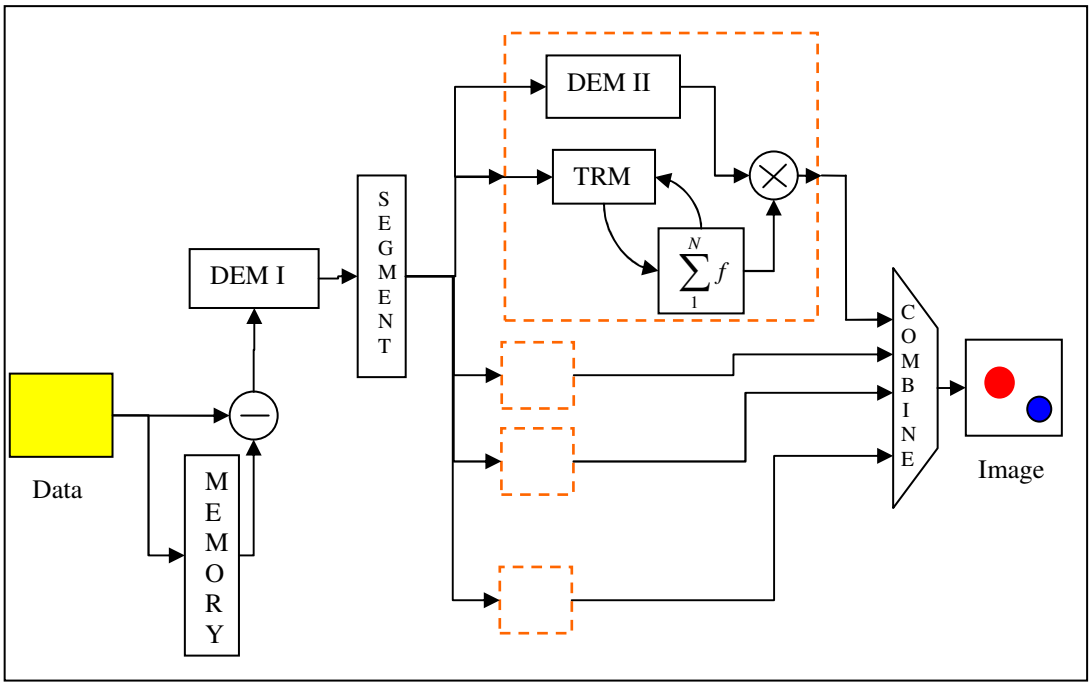

Fig. 5.21 The diagram showing the processing scheme

5.3.4.1 Estimation of Number of Targets

The procedure of estimating the number of target is something that we did not spent much effort on due to the limitations in time. Here we will briefly mention some experimental results which can be used in estimating the number of targets. As we have mentioned in Chapter 3, the number of targets in the environment is determined looking at the multiplicity of the smallest singular value in TRM algorithm, and the multiplicity of the smallest eigenvalue in DEM algorithm. In noise free, ideal conditions the smallest singular value of TRM algorithm is zero. In DEM the smallest eigenvalue is not zero but small depending on the performance of correlation. Since we are using the difference waveforms some other things should also be taken into account. Here, we will briefly mention about the singular values of a sample TRM process on the difference waveforms of the experimental data.

Since we used four transmitter and four receiver antennas, the multistatic response matrix is four by four. So there exist four singular values related. These four singular values are plotted in Fig. 5.22 against frequency in dB scale as in [25] for four different experimental difference waveforms. In the environment there are two targets, therefore two of the largest singular values are signal singular values. The gray dashed curve represents 15dB below of the first (greatest) singular value, the blue curve. A thresholding may be a solution for the number of targets.

The following figure, Fig. 5.23 shows the resultant eigenvalues of the DEM algorithm for the whole data we obtained in our experiment which will be presented in the next section. To obtain this figure the parameter L of the DEM algorithm is chosen to be 4, therefore there are four eigenvalues of the covariance matrix. Remember that choosing L small provides better decorrelation and therefore better distinction between the eigenvalues. To explain briefly, we have fourteen data sets each containing sixteen difference waveforms. Therefore totally we have 224 difference waveforms. For each of the fourteen data sets, four eigenvalues are plotted in different colors against the waveforms used. As shown in the figure there are discrete levels for each of the four eigenvalues. The plot of eigenvalues for L=5,6 and 7 are also shown in Fig. 5.24. As we have told we did not further study on how to deduce the number of targets but again applying a threshold may be a solution.

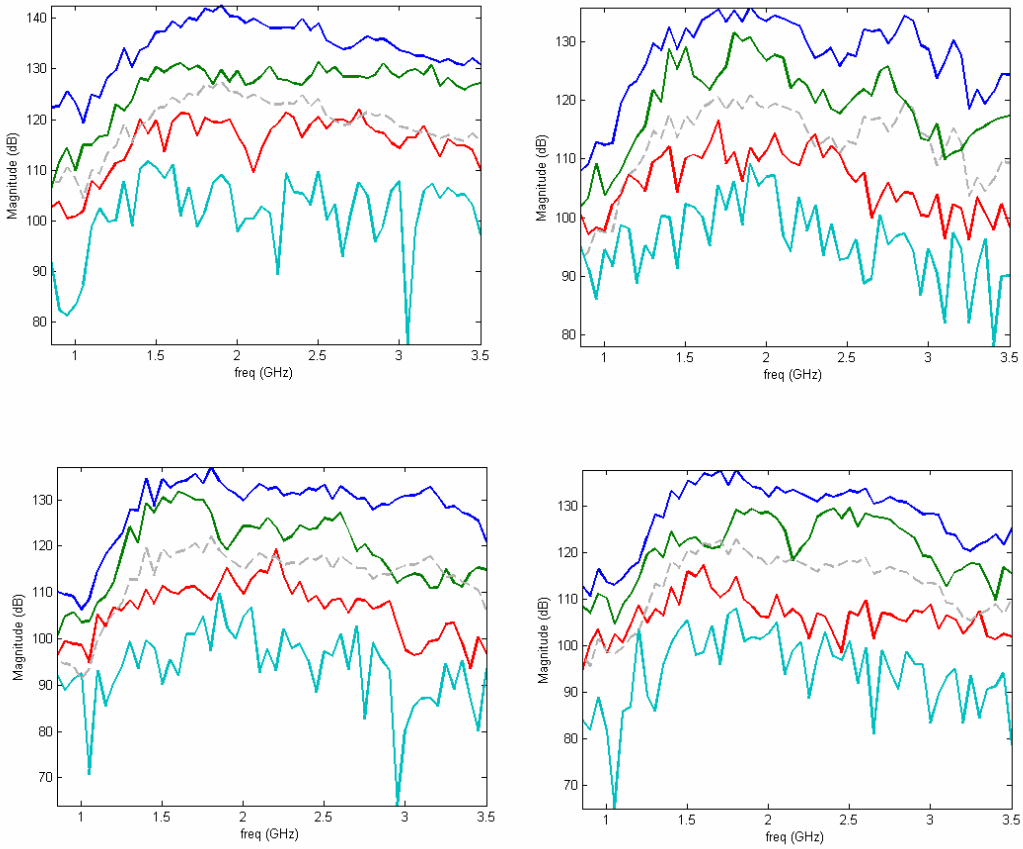

Fig. 5.22 Four singular values of the TRM algorithm plotted for four different experimental results

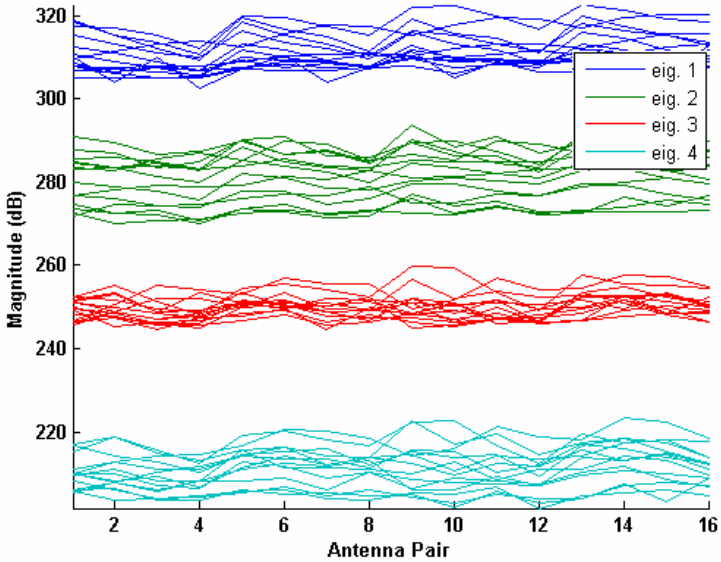

Fig. 5.23 Eigenvalues of DEM algorithm for L=4

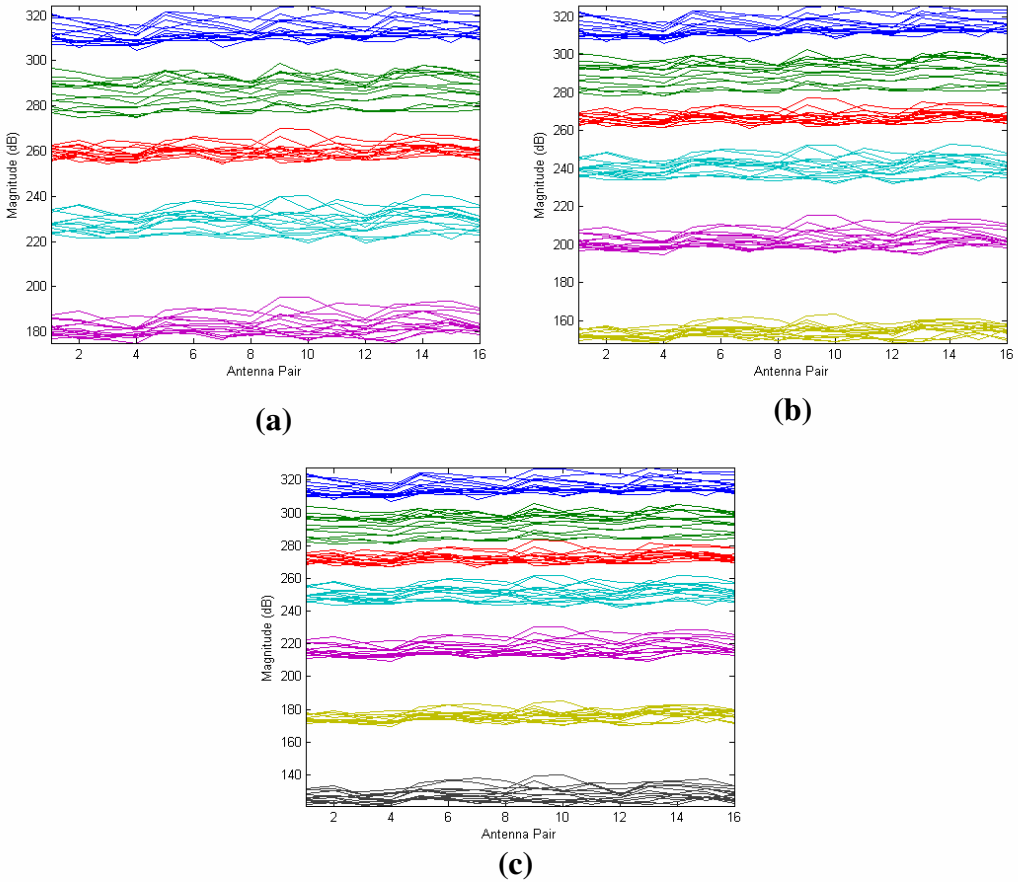

Fig. 5.24 Eigenvalues of DEM algorithm **(a)** *L*=5 **(b)** *L*=6 **(c)** *L*=7

Until now we have presented the theoretical aspect of the processing algorithms, the applications of these algorithms, the problems encountered and the scheme to be followed in order to improve target localization. In the next section we will introduce the real life experiments we have performed using our radar setup and the results obtained.

5.4 The Experiment

In the experiment we are trying to detect two identical moving targets. The environment is a square shaped court surrounded by brick walls. The drawing in Fig .5.25 illustrates the experimental environment.

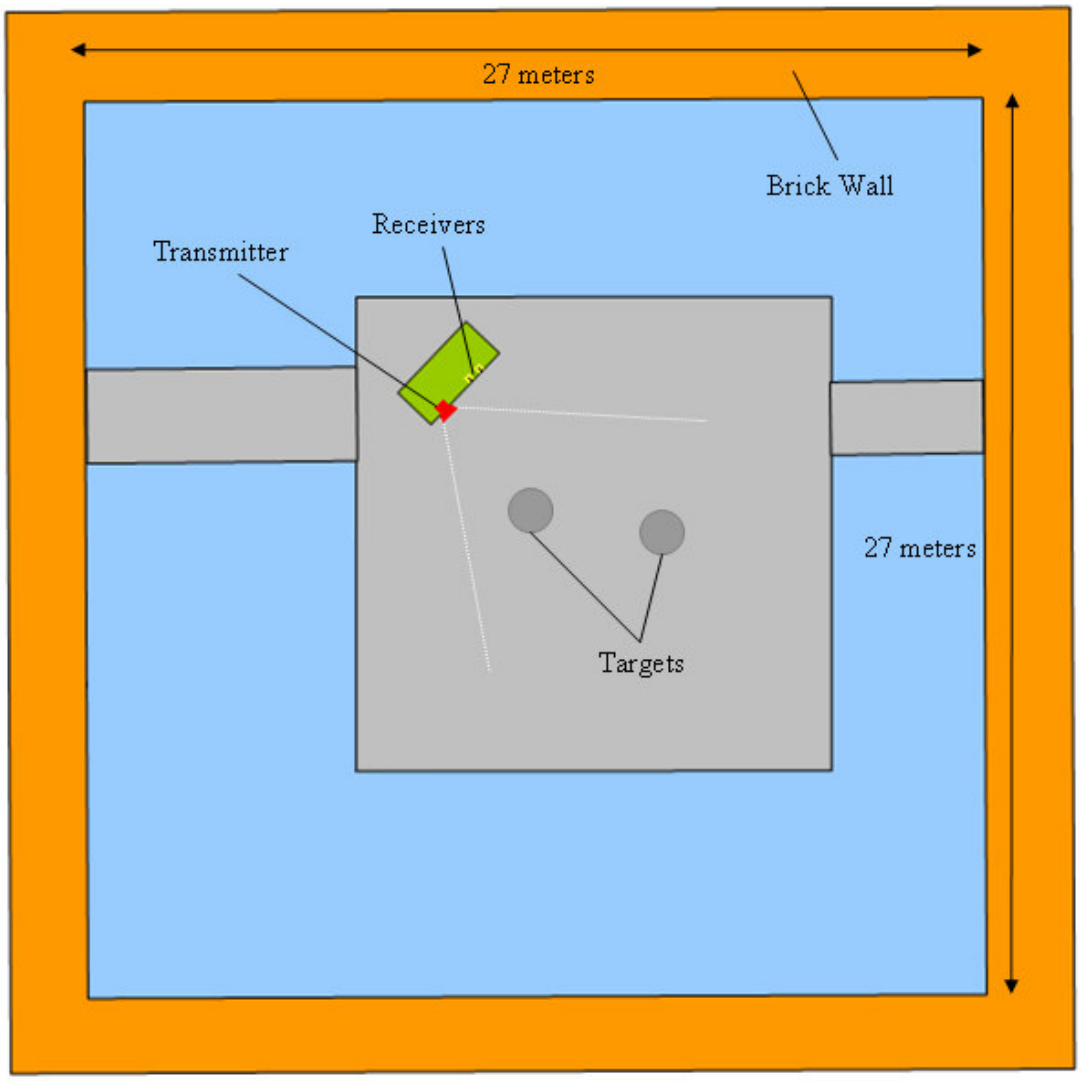

Fig. 5.25 Illustration of the experimental environment

The radar setup is positioned facing the corners of the building in order to reduce the effect of reflections coming from the walls. In fact the reflections coming from stable objects are eliminated by taking the difference of consecutive snapshots; however since there are multiple reflections inside the receiver block due to mismatched components, they may degrade the performance up to some degree. Therefore strong reflections from stable objects are avoided where possible.

The trajectory of the targets resembles a circular path as seen in Fig. 5.26. Each target is a cylinder with 26 cm diameter and 40 cm height, elevated from the ground so that, midpoint of its height is in the same x-y plane with the antennas.

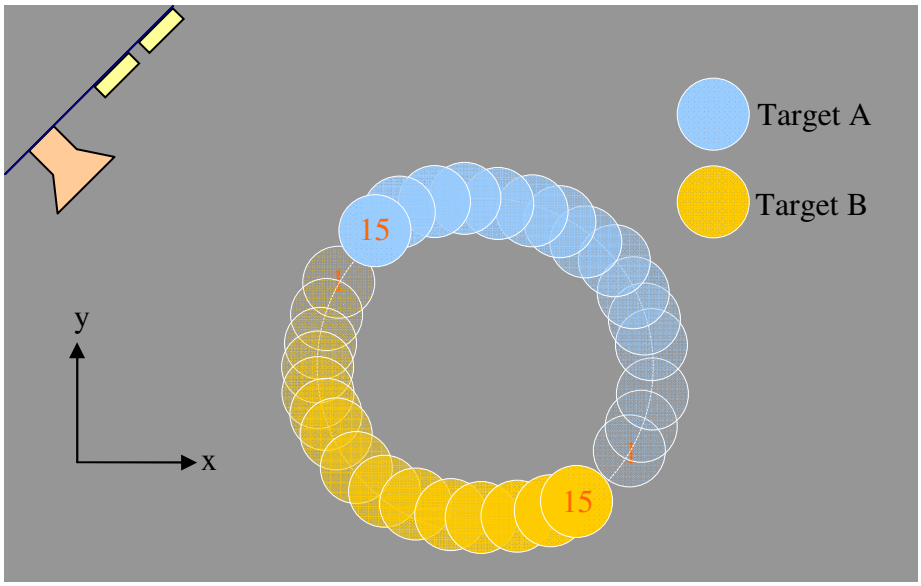

Fig. 5.26 The motion path of the targets

There are a total of fifteen target positions. When a data acquisition cycle described in section 5.2 finishes, the targets are moved to their next positions for the next acquisition cycle. Since we will use the difference of consecutive snapshots, we will obtain fourteen sets of difference waveforms which means fourteen frames at the end of processing.

Fig. 5.27 shows a sample received waveform and its Fourier transform. The first arriving pulses are the ones coupled directly from the transmitter antenna to the receiver antenna. Two echoes coming from the two targets are also seen.

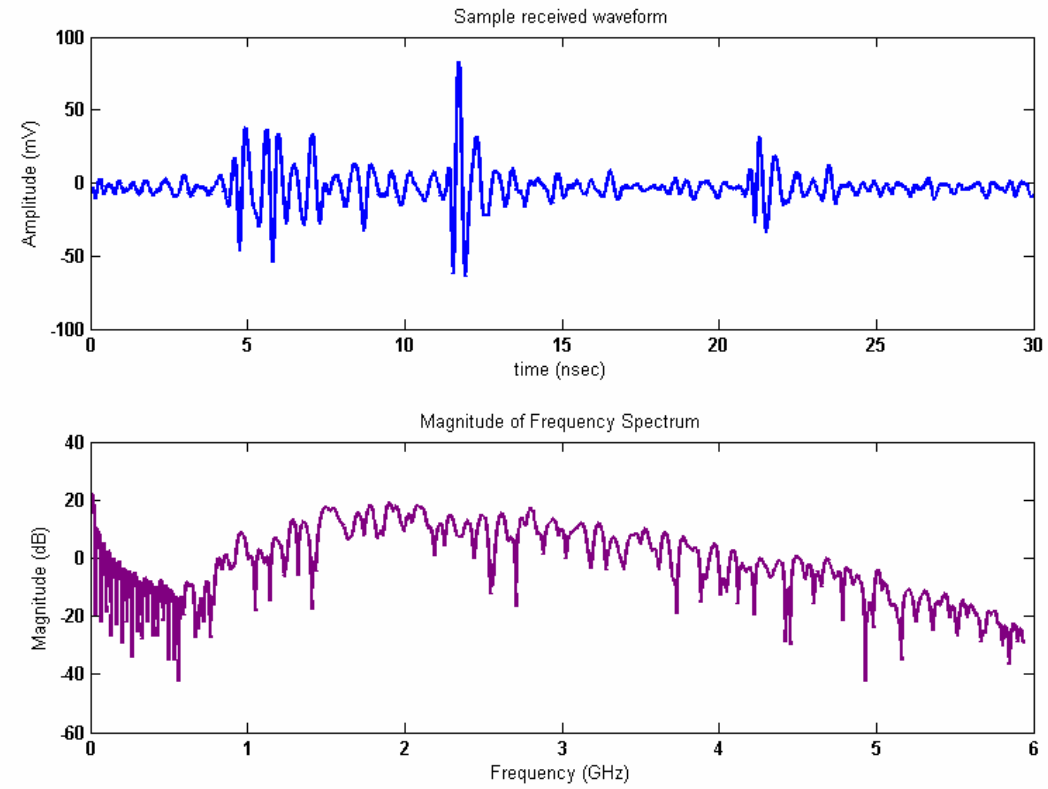

Fig. 5.27 A sample difference waveform and its Fourier transform magnitude

is subtracted from the snapshot taken for their previous arrangement. The effect of antenna coupling is removed since the delays and shapes of the coupled pulses are stationary and at the neighborhood of the actual targets echoes there occurs non-zero signals that can be accounted for target echoes. The remaining processing steps described in section 5.3.4 are carried out.

Since we are using DEM method to estimate the delays of the echoes, combining the two TRM spectra may not be necessary. First we will present the fourteen frames where the TRM spectrum related with the receiver array (equation (4.36)) is used together with the DEM spectrum. The obtained spectrum for the j^{th} segment can be written as:

$$P^{j} = P^{j,DEM} \times \left[P_R^{j,TRM}(f_1) + P_R^{j,TRM}(f_2) ... + P_R^{j,TRM}(f_N) \right] \qquad (5.3)$$

where $P_R^{j,TRM}(f_n)$ is the receiver array related TRM spectrum at frequency f_n and $P^{j,DEM}$ is the DEM spectrum of segment j. Each segment is then spliced. Resultant fourteen frames are seen in Fig. 5.28. The computational domain is 10 meters in vertical dimension and 4.5 meters in horizontal dimension.

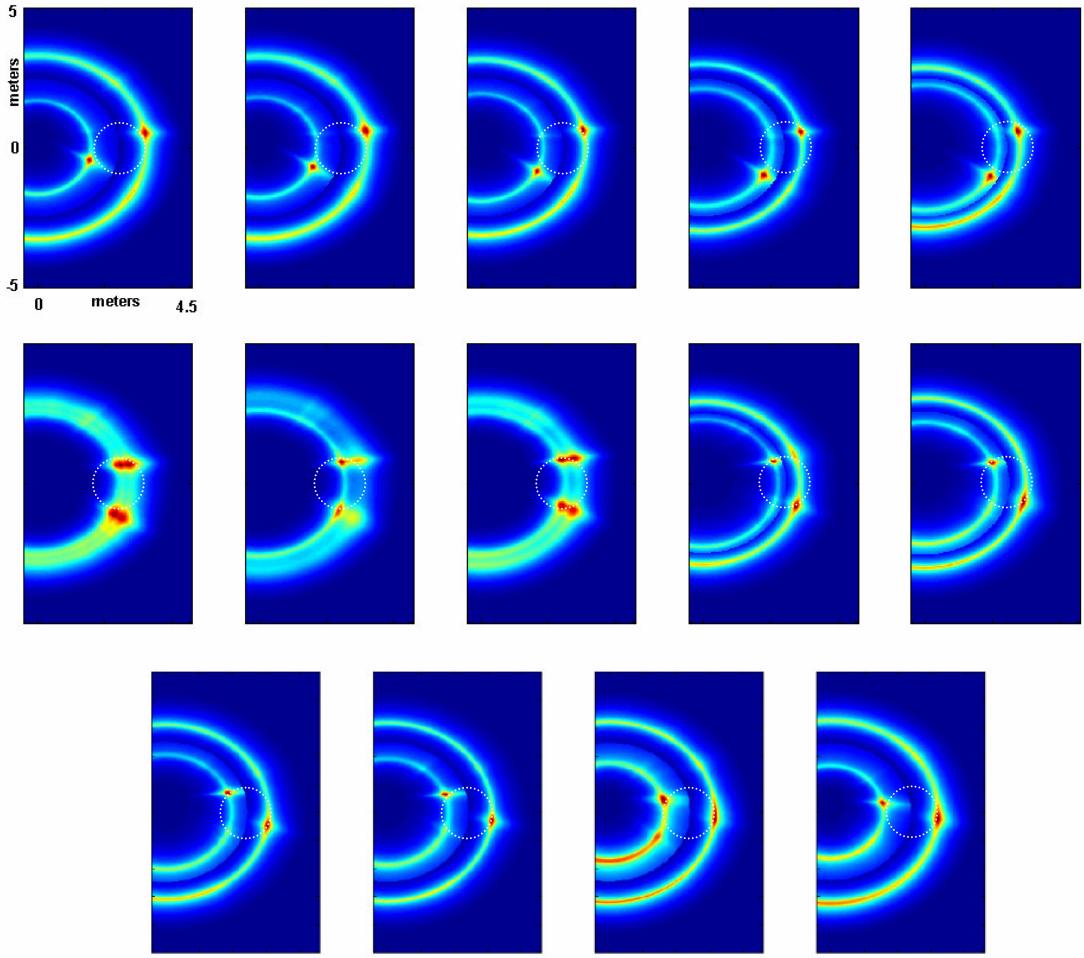

Fig. 5.28 Resultant fourteen frames at the end of processing the experimental data by combining the receiver related TRM spectrum and the spatial DEM spectrum

The circular motion of the targets can be observed. The locations of the targets can be identified looking at the intense (red) regions in the plots. In plots 1 to 5 and 9 to 14, segmentation is applied since the waveforms were suitable. The elliptical trace separating the two regions can be recognized. In 6, 7 and 8 there is no segmentation since the target echoes are overlapped in time. In there images, there appears false images of the targets close to actual ones. The performance of detection is the poorest for 13th frame where there is azimuthal spread.

When we use the DEM spectrum together with the transmitter array spectrum of the TRM the graphs shown in Fig.29 are obtained. This formula representing the overall spectrum of the j^{th} segment is

$$P^{j} = P^{j,DEM} \times \left[P_T^{j,TRM}(f_1) + P_T^{j,TRM}(f_2) \ldots + P_T^{j,TRM}(f_N) \right] \qquad (5.4)$$

where $P_T^{j,TRM}(f_n)$ is the receiver array related TRM spectrum at frequency f_n.

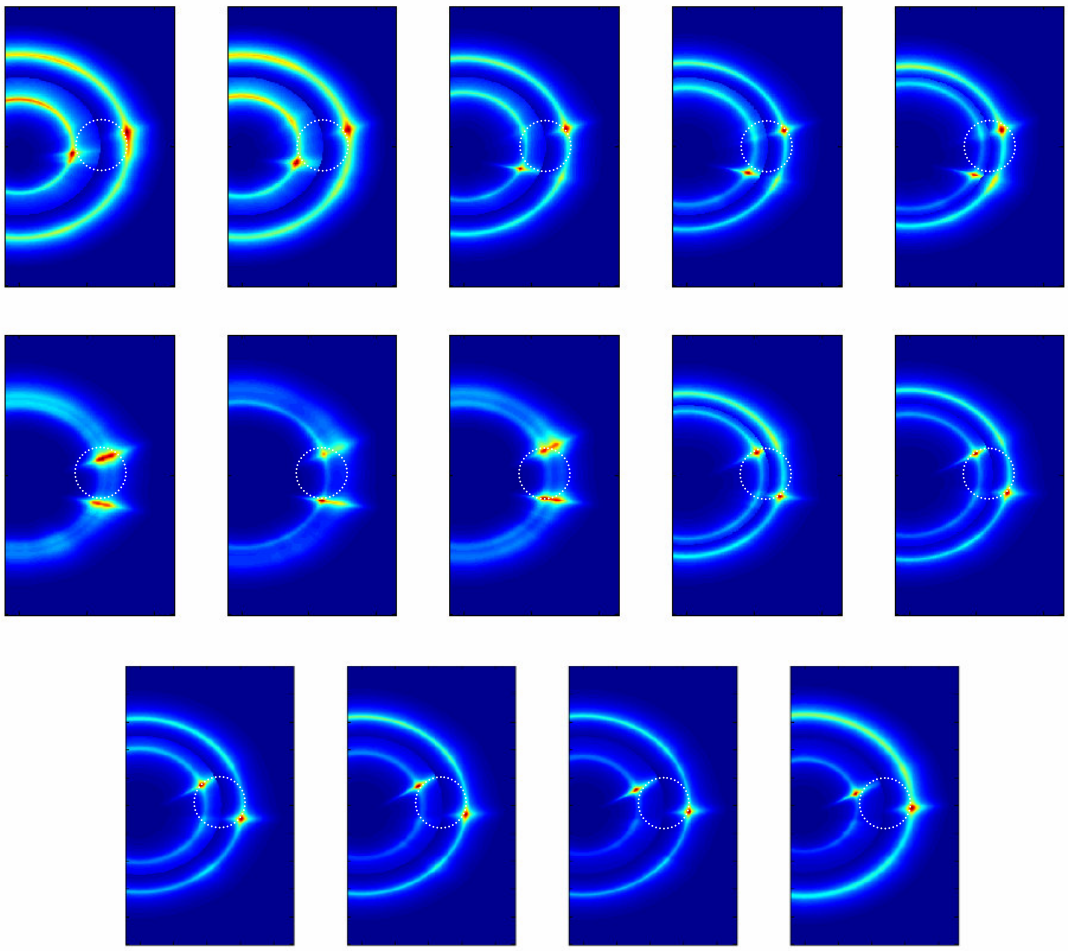

Fig. 5.29 Resultant fourteen frames at the end of processing the experimental data by combining the transmitter related TRM spectrum and the spatial DEM spectrum

The circular motion of the targets can be observed in this figure as well. Fig. 5.30 is the result when the receiver array spectrum and the transmitter array spectrum is combined using formula (4.40) and the resultant spectrum is multiplied by the DEM spectrum. We can not say that there has been a significant improvement when we compare Fig. 5.30 with Fig. 5.28 and Fig. 5.29.

Fig.5.31 is obtained by multiplying the maps of Fig. 5.28 and 5.29. The locations of the targets became more clear while the clutter in the maps are disappeared. Finally Fig. 5.32 shows the processing result obtained similar to Fig. 5.31 however without segmentation. The Type 2 ambiguities can be seen.

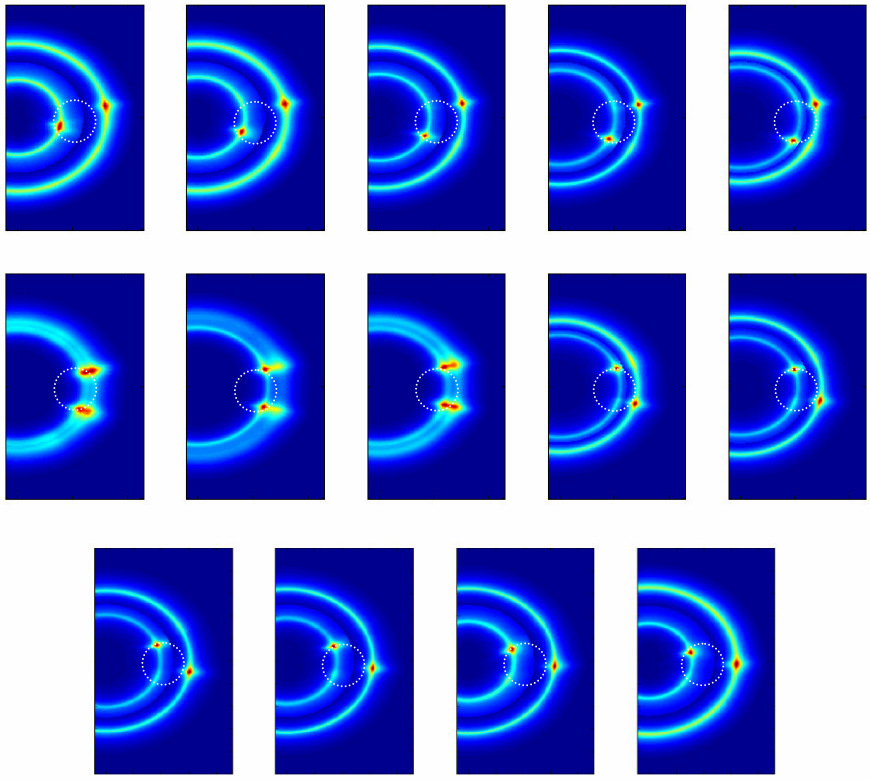

Fig. 5.30 Resultant maps when the spectrum in (4.40) is multiplied with the spatial DEM spectrum

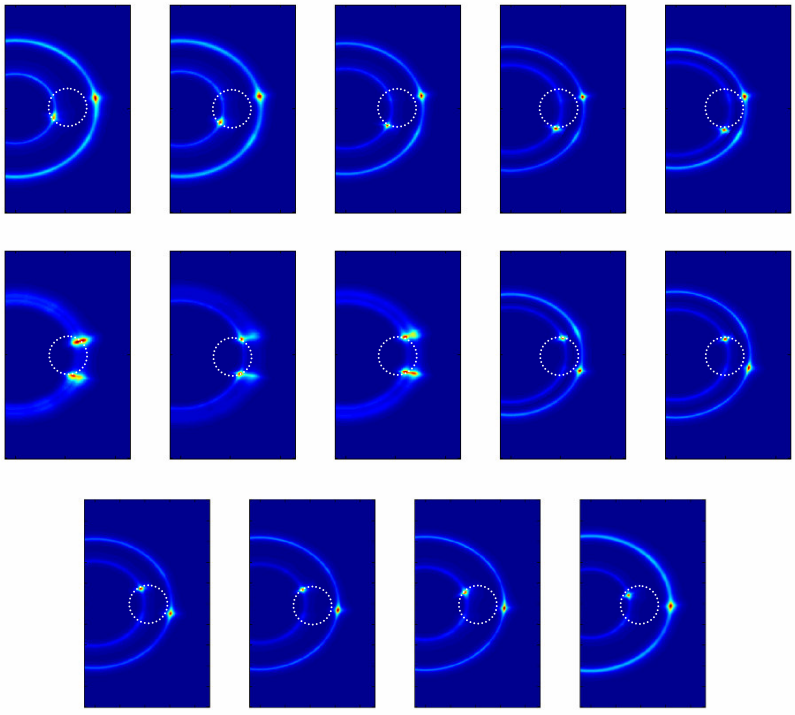

Fig. 5.31 Multiplication of two maps obtained in Fig. 2.28 and Fig. 5.29

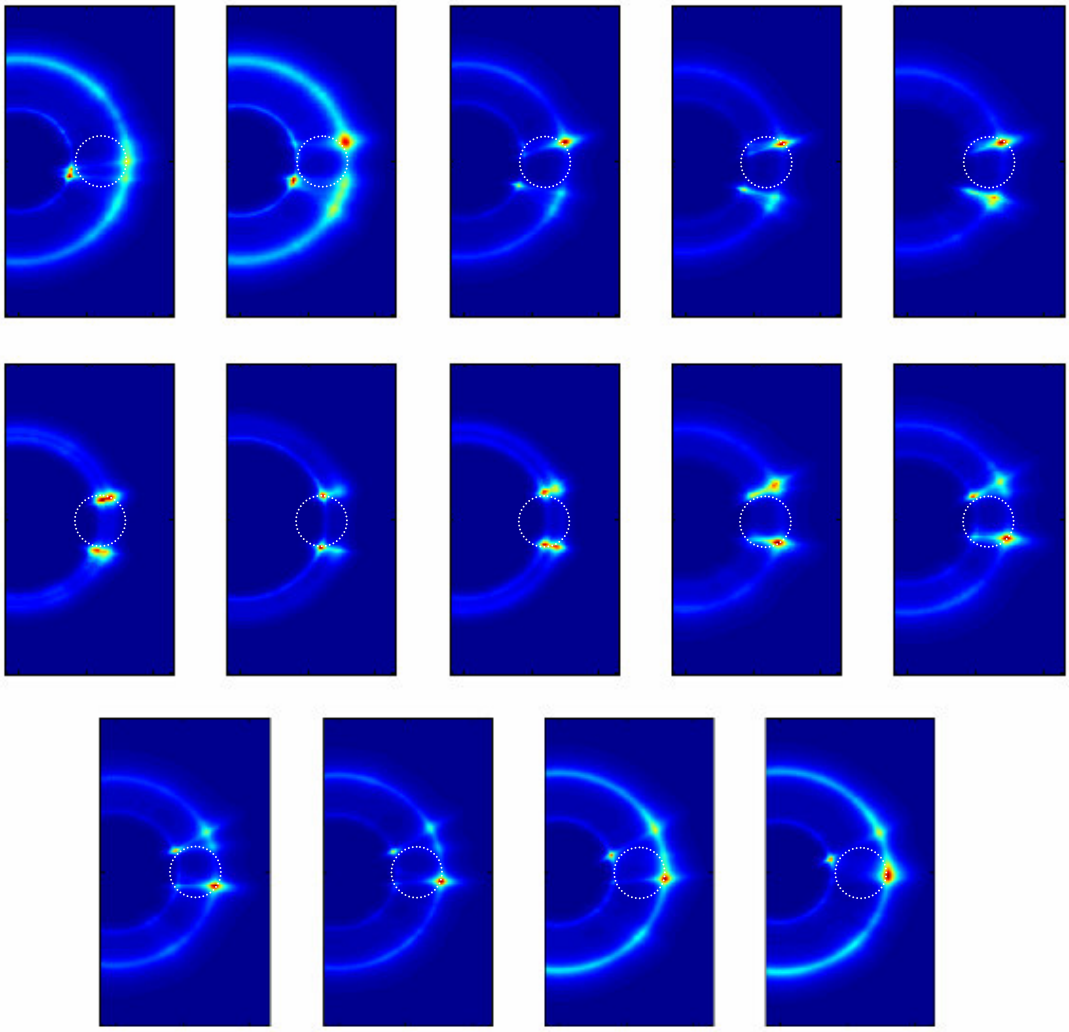

Fig. 5.32 The multiplication of the receiver array related TRM spectrum, the transmitter array related TRM spectrum and the spatial DEM spectrum without segmentation

As a summary of the chapter, we described our experimental setup, how we utilized the processing algorithms to improve target localization and presented the results. In the next chapter we will summarize the study we have done so far, provide final comments and discuss what can be done next in order to improve the detection capability of our radar system further.

CHAPTER 6

CONCLUSIONS AND FUTURE WORK

In this study our main aim was to improve the detection performance of our Ultra Wideband (UWB) radar system using super-resolution algorithms. Therefore the major effort is spent on signal processing. We used Multiple Signal Classification (MUSIC) algorithms to estimate both the directions and the ranges of the targets. The Time Reversal MUSIC (TRM) algorithm was originally developed for acoustical imaging and uses a single frequency. We improved the capability of TRM algorithm with the wide frequency information available as a result of using UWB pulses.

Finite Difference Time Domain (FDTD) computer simulations were run throughout the research. The performance of the signal processing algorithms is tested by computer simulations and also using the data acquired by our Ultra Wideband radar system. The major source of undesired effects was the internal reflection inside the receiver block of the system. However the results of the detection were successful but still needs to be improved.

Three methods to eliminate ambiguities in detection are also explained. First one is combining processing results of TRM algorithm at multiple frequencies, secondly processing echoes that are distant enough from each other in time separately and lastly by proper antenna orientation. We used the first two methods in processing the experimental data; however the effectiveness of the third method is shown by FDTD simulations.

As future improvements in the hardware side, the system internal reflections due to unmatched components should be solved. This will increase the performance of detection and allow the usage of less number of frequency components to achieve results. As a result the computational time will be increased. Also adding more antennas will make the usage of the radar more practical especially when collecting

multistatic data. In order to perform through-wall or subsurface detection experiments, the power of the transmitter should be increased.

For the signal processing side, for real time operation of the system the processing speed should be reduced. Eigenvalue decomposition of the covariance matrices is the major time consuming step. Instead of performing computation for different components a method is to transform all the covariance matrices at different frequencies to a common frequency and performing the singular value decomposition only on this matrix. However this is an iterative method and we are not sure whether this will reduce the computation time or not at this time. In order to eliminate Gaussian noise, instead of using second order covariance matrices, the usage of fourth or higher order cumulants will be investigated. If successful results are obtained the system can be commercialized at the end.

REFERENCES

[1] F. R. Dickey, JR., M. Labitt, F. M. Staudaher, "Development of Airborne Moving Target Radar for Long Range Surveillance," IEEE Transactions on Aerospace and Electronic Systems, vol. 14, no. 6, pp. 959-972,November 1991.

[2] J. Clarke, "Airborne Early Warning Radar," Proceedings of the IEEE, vol. 73, no.2, pp. 312-324, February 1985.

[3] W. W. Shrader, "Radar Technology Applied to Air Traffic Control," *IEEE Transactions on Communication*, vol. com-21, no. 5, pp. 591-605, May 1973.

[4] P. R. Drouilhet, Jr., "The Development of the ATC Radar Beacon System: Past, Present, and Future, *IEEE Transactions on Communication*, vol. com-21, no. 5, pp. 408-421, May 1973.

[5] B. A. Kumar, D. Ghose, "Radar-Assisted Collision Avoidance/Guidance Strategy for Planar Flight," *IEEE Transactions on Aerospace and Electronic Systems, vol.37, no. 1, pp. 77-90, January 2001.*

[6] C. E. Moore and J. D. ELPI, "Optimum Collision Avoidance for MerchantShips," *IEEE Transactions on Industry Applications, vol. IA-9, no. 6, pp. 640-647, November/December 1973.*

[7] K. Lai, M. Cherniakov, "Super Fast Scanning Radar With Tomographic Gap Application For Weather Phenomena Studies," in *Proc. IEEE International Geoscience and Remote Sensing Symposium*, July 2000, pp. 521-523.

[8] E. Im, S. L. Durden, Y. Rahmat-Samii, H. Fang, V. Cable, M. Lou, J. Huang, "Advanced Geostationary Radar for Hurricane Monitoring and Studies," in *Proc.* IEEE Radar Conference, April 2004, pp.307-311.

[9] Potin, D.; Duflos, E.; Vanheeghe, P.; "Landmines Ground-Penetrating Radar Signal Enhancement by Digital Filtering," *IEEE Transactions on Geoscience and Remote Sensing*, vol. 44, issue 9, pp. 2393-2406, September 2006.

[10] V. P. Prokhorenko, V. E. Ivashchuk, S. V. Korsun, "Ground penetrating radar VIY-2," *IEEE Aerospace and Electronic Systems Magazine*, vol. 20, issue 7, pp. 16-18, July 2005.

[11] T. Counts, A. C. Gurbuz, W. R. ScottJr., J. H. McClellan, K. Kim, "Multistatic Ground-Penetrating Radar Experiments," *IEEE Transactions on Geoscience and Remote Sensing*, vol. 45, issue 8, pp. 2544-2553, August 2007.

[12] John K. Harmon, "Planetary Delay-Doppler Radar and the Long-Code Method," *IEEE Transactions on Geoscience and Remote Sensing*, vol. 40, issue 9, pp. 1904-1916, September 2002.

[13] H. R. Raemer, *Radar System Principles. Boca Raton, FL: CRC, 1995.*

[14] J. Taylor, Ed., *Introduction to Ultra-Wideband Rader Systems*. Boca Raton, FL: CRC, 1995.

[15] R.J. Fontana, "Recent System Applications of Short-Pulse Ultra-Wideband (UWB) Technology," *IEEE Trans. Microwave Theory Tech.,* vol. 52, no. 9, pp. 2087–2104, September 2004.

[16] I. I. Immoreev**,** Ten questions on UWB, *IEEE Aerospace and Electronic Systems Magazine*, vol. 18, issue 11, pp.8-10, November 2003.

[17] S. Azevedo, T. E. McEwan, "Micropower Impulse Radar," *IEEE Potentials*, vol. 16, issue 2, pp 15-20, April-May 1997.

[18] T. E. McEwan. "Phase coded, micro-power impulse radar motion.", U.S. Patent 5 519 400, May 21, 1996.

[19] T. E. McEwan. "Ultra-wideband receiver.", U.S. Patent 5 523 760, June 4, 1996.

[20] T. E. McEwan. "Ultra-wideband radar motion sensor.", U.S. Patent 5,361,070, November 1, 1994.

[21] T. E. McEwan. "Body monitoring and imaging apparatus and method.", U.S. Patent 5,766,208, June 16, 1998.

[22] S. Gogineni, K. Wong, S. Krishnan, P. Kanagaratnam,.T. Markus, V. Lytle, "An ultra-wideband radar for measurements of snow thickness over sea ice," in *Proc. IEEE International Geoscience and Remote Sensing Symposium*, July 2003, pp. 2802-2804.

[23] P. Kanagaratnam, T. Markus, V. Lytle, B. Heavey, P. Jansen, G. Prescott, and S.P. Gogineni, "Ultrawideband Radar Measurements of Thickness of Snow Over Sea Ice," *IEEE Transactions on Geoscience and Remote Sensing,* vol. 45, no. 9, pp. 2715–2724, September 2007.

[24] S .K. Davis, H. Tandradinata, S.C. Hagness, and B.D. Van Veen, "Ultrawideband microwave breast cancer detection: A detection-theoretic approach using the generalized likelihood ratio test," *IEEE Trans. Biomed. Eng.,* vol. 52, no. 7, pp. 1237–1250, July 2005.

[25] G. Micolau, M. Saillard, P. Borderies, "DORT method as applied to ultrawideband signals for detection of buried objects," *IEEE Transactions on Geoscience and Remote Sensing,* vol. 41, issue 8, pp. 1813-1820, August 2003.

[26] C. Prada, S. Manneville, D. Spoliansky, and M. Fink, ''Decomposition of the time reversal operator: Detection and selective focusing on two scatterers,'' *J. Acoust. Soc. Am.*, vol. 99, issue 4, pp. 2067–2076, April 1996.

[27] E. Kerbrat, C. Prada, D. Cassereau, and M. Fink, "Imaging in the presence of grain noise using the decomposition of the time reversal operator ," *J. Acoust. Soc. Am., vol.* 113, issue 3, pp. 1230-1240, March 2003

[28] C. Prada and J.L. Thomas, "Experimental subwavelength localization of scatterers by decomposition of the time-reversal operator interpreted as a covariance matrix*", J. Acoust. Soc. Am., vol.* 114, issue 1, pp. 235-243, July 2003.

[29] Yee, K. S., "Numerical solution of initial boundary value problems involving Maxwell's equations in isotropic media," *IEEE Trans. Antennas and Propagation*, vol. 14, issue 3, pp. 302-307, May 1966.

[30] A. Taflove and S. C. Hagness, Computational Electrodynamics: The Finite-Difference Time-Domain Method, 2nd ed. Norwood, MA: Artech House, 2000.

[31] J. De Poorter and D. Botteldooren, "Acoustical Finite-Difference Time-Domain Simulations of Subwavelength Geometries," *J. Acoust. Soc. Am., vol.* 104, issue 3, pp. 1171-1177, September 1998.

[32] X. Yuan, D. Borup, J. W. Wiskin, M. Berggren, R. Eidens, S. A. Johnson, "Formulation and validation of Berenger's PML absorbing boundary for the FDTD simulation of acoustic scattering," *IEEE Transactions on Ultrasonics, Ferroelectrics and Frequency Control*, vol. 44, issue 4, pp. 816-822, July 1997.

[33] W. C. Chew and W. H. Weedon, "A 3-D Perfectly Matched Medium from modified Maxwell's equations with stretched coordinates," *Microwave and Optical Technology Letters*, vol. 7, issue 13, pp. 599-604, September 1994.

[34] R. O. Schmidt, "A signal subspace approach to multiple emitter location and spectral estimation," Ph.D. dissertation, Stanford Univ., Stanford, CA, Nov. 1981.

[35] A. L. Swindlehurst, T. Kailath, "A Performance Analysis of Subspace-Based Methods in the Presence of Model Errors: Part II-Multidimensional Algorithms," *IEEE Trans. Signal Processing*, vol. 41, no. 9, September 1993.

[36] T.-J. Shan, M. Wax, and T. Kailath, "On spatial smoothing for direction-of-arrival estimation of coherent signals," IEEE Trans. Acoust., Speech, Signal Processing, vol. ASSP-33, no. 4, pp. 806-811, Aug. 1985.

[37] R. T. Williams, S. Prasad, A. K. Mahalanabis, "An Improved Spatial Smoothing Technique for Bearing Estimation in a Multipath Environment," *IEEE Trans. Acoust., Speech, Signal Processing*, vol. 36, no. 4, pp. 425-432, April 1988.

[38] B. Porat, B. Friedlander, “Direction finding algorithms based on high-order statistics,” *IEEE Transactions on Signal Processing*, vol.39, issue 9, pp. 2016-2024, September 1991.

[39] H. Wang, M. Kaveh, “Coherent signal-subspace processing for the detection and estimation of angles of arrival of multiple wide-band sources,” *IEEE Trans. Acoust., Speech, Signal Processing*, vol. ASSP-33, no. 4, pp. 823-831, August 1985.

[40] S. Valaee, P. Kabal, **“**Wideband array processing using a two-sided correlation transformation,” *IEEE Transactions on Signal Processing*, vol.43, issue 1, pp. 160-172, January 1995.

[41] Kyung-Tae Kim, Dong-Kyu Seo, and Hyo-Tae Kim, “Efficient Radar Target Recognition Using the MUSIC Algorithm and Invariant Features,” *IEEE Trans. Antennas and Propagation*, vol. 50, no. 3, pp. 325-337, March 2002.

[42] H. Lev-Ari and A.J. Devaney, “The time-reversal technique re-interpreted: Subspace-based signal processing for multi-static target location,” in *Proc. IEEE Sensor Array and Multichannel Signal Processing Workshop*, Cambridge, MA, March 2000, pp. 509-513.

[43] J. E. Evans, J. R. Johnson, and D. F. Sun, “Application of advanced signal processing techniques on angle of arrival estimation in ATC navigation and surveillance systems,” M.I.T. Lincoln Lab., Lexington, MA. Tech. Rep. 582, June 1982.

[44] M. Wax, T. Kailath, "Detection of signals by information theoretic criteria," *IEEE Transactions on Acoustics, Speech, and Signal Processing*, vol.33, no.2, pp. 387-392, April 1985.

[45] A. Quinquis, E. Radoi, F.-C. Totir, "Some radar imagery results using superresolution techniques," *IEEE Transactions on Antennas and Propagation,* vol.52, no.5, pp. 1230-1244, May 2004

[46] J. W. Odendaal, E. Barnard, C. W. I. Pistorius, "Two-dimensional superresolution radar imaging using the MUSIC algorithm," *IEEE Transactions on Antennas and Propagation,* vol.42, no.10, pp.1386-1391, Oct 1994

[47] S. K. Lehman, A. J. Devaney, “Transmission mode time-reversal super-resolution imaging,” *J. Acoust. Soc. Am., vol.* 113, issue 5, pp. 2742-2753, May 2003.

[48] F. K. Gruber, E. A. Marengo, A. J. Devaney, “Time-reversal imaging with multiple signal classification considering multiple scattering between the targets,” *J. Acoust. Soc. Am., vol.* 115, issue 6, pp. 3042-3047, June 2004.

[49] A. J. Devaney, E. A. Marengo, and F. K. Gruber, “Time-reversal-based imaging and inverse scattering of multiply scattering point targets,” *J. Acoust. Soc. Am., vol.* 118, issue 5, pp. 3129-3138, November 2005.

[50] A. J. Devaney, "Time reversal imaging of obscured targets from multistatic data," *IEEE Transactions on Antennas and Propagation*, vol.53, no.5, pp. 1600-1610, May 2005.

[51] A. Ekşim, "New wideband microstrip feeding slot antenna design and implementation," M.Sc. dissertation, Sabancı University, İstanbul,, 2004.